2015

# Surface Structure/Property Relationship for (001) Surface of Magnetite

Fangyang Liu
*Louisiana State University and Agricultural and Mechanical College*

# SURFACE STRUCTURE/PROPERTY RELATIONSHIP FOR (001) SURFACE OF MAGNETITE

A Dissertation

Submitted to the Graduate Faculty of the
Louisiana State University and
Agricultural and Mechanical College
in partial fulfillment of the
requirements for the degree of
Doctor of Philosophy

in

The Department of Physics and Astronomy

by
Fangyang Liu
B.S., University of Science and Technology of China, 2005
May 2016

## ACKNOWLEDGEMENTS

I would like to first thank my advisor, Prof. Ward Plummer, for providing me the opportunity to start my research work in physics department of Louisiana State University. I extremely appreciate his guidance and educate during my PhD study. I benefited a lot from his altitude to science, ways of thinking as physicist and ability to present a work. I would also thank Dr. Jiandi Zhang and Dr. Rongying Jin for the detailed instruction in experiments, trouble shooting and patient explanation of physics problems. I also want to acknowledge my committee, Dr. Phillip Sprunger and Dr. Jianwei Wang, for their guide on my project and dissertation. I would like to acknowledge Dr. Richard Kurtz and Dr. Von Braun Nascimento for their support and many useful advices during my thesis work.

I also want to express my thanks to Dr. Xiaobo He and Dr. Jing Teng, who introduced me to the field of ultra-high vacuum experiments. I send my thanks to collaborators in Center of Advanced Microstructure & Devices: Dr. Orhan Kizikaya and Dr. Eizi Morikawa, who help me for the synchrotron experiments. I feel grateful to Chen Chen, Lina Chen and Gaomin Wang, who came to LSU at the same time with me and worked in the same group for these years. I need to send my thanks to all my colleagues who were or are in LSU: Dr. Jisun Kim, Dr. Guorong Li, Dr. Hangwen Guo, Dr. Zhaoliang Liao, Dr. Yi Li, Dr. Junsoo Shin, Dr. Dalgis Mesa, Mohammad Saghayezhian, David Howe, Dr. Biao Hu, Dr. Yiming Xiong, Dr. Amar Karki, Jianneng Li, Zhenyu Diao, Jiayun Pan, Dr. Zhenyu Zhang, Dr. Ziyu Zhang, Dr. Fei Wang and Frank Womack. I also want to thank LSU electronic shop, machine shop and department main office for their help.

My final acknowledgements go to my family, including my wife and parents. They are the most important people in my life, and I greatly thank them for the love and support to me.

# TABLE OF CONTENTS

## ABSTRACT

Magnetite ($Fe_3O_4$), a well-known magnetic material, is still attracting intense study because of its great application in catalyst and technology development. These useful properties are related to the coexistence and coupling of several degrees of freedom, including charge, lattice, orbital and spin. The interaction between $Fe_3O_4$ and hydrogen is one of the most important issues, which guides the development of catalytic efficiency and material practicality. In this work, natural single crystal $Fe_3O_4$ (001) surfaces are studied with a variety of techniques. It is discovered that the $Fe_3O_4$ (001) surface structure and properties are dependent on the surface preparation methods. Conventional processed surfaces in an oxygen-rich environment are found to be oxygen deficient, with a significant amount of ordered oxygen vacancies on the surface and even penetrate deep into the bulk. The more stoichiometric surface is then obtained by ozone treatment, which successfully removes most surface vacancies. Atomic hydrogen is used to probe the $Fe_3O_4$ (001) surface. On an ozone processed (OP) surface, H bonds to surface oxygen, which form hydroxyl as expected. However, on conventional processed (CP) surfaces, H is found to bond preferentially to the surface Fe atoms. This abnormal H-Fe bonding is a result of oxygen vacancies on the CP surface. One explanation is, when H is adsorbed by a CP surface, it leads to the formation and desorption of water, thus creating more oxygen vacancies and stabilizing H-Fe bonds. Our study shows that previous experimental work on CP $Fe_3O_4$ surfaces all deal with oxygen deficient surfaces, which solves the long disagreement between experimental results and theoretical predictions. The different H bonding on CP and OP surfaces can serve as a novel direction of catalysis development and hydrogen storage applications.

# CHAPTER 1 GENERAL INTRODUCTION

## 1.1 Background of $Fe_3O_4$

$Fe_3O_4$ (magnetite) was discovered around 1500 BC because of its magnetic properties. As the oldest magnet, it has been studied for decades, but it is still attracting attention owing to its relevance to technological development. It is used as the core material of hardware, such as electromagnetic coils, microwave resonant circuits, computer memory cores and high density magnetic recording media.[1-6] It is also an important catalyst in ammonia synthesis, Fischer-Tropsch synthesis, and also in high temperature water gas phase shift reactions.[7-15] In the field of geology, $Fe_3O_4$ can affect the local magnetic field as a frequently occurred magnetic material in the earth's crust. [16,17] Due to its multi-valence features, it has been used as a redox active material, where $Fe^{2+}$ can reduce toxic species such as chlorinated organics and chromate.[18-20]

$Fe_3O_4$ is among the family of correlated electron system, where electron charge, spin, orbital, and lattice degrees of freedom are intimately related. In conventional metals, electrons are usually considered non-interacting and can travel freely in the material, which is typically referred to as the free electron model. However, in correlated electron systems, electrons are localized and interact with each other strongly. Because of this fundamental difference compared to ideal free electron systems, correlated electron materials would present many fascinating properties, such as metal insulator transitions, half metallicity, charge density waves, spin density waves, and high temperature superconductivity. In the past several years, extensive research has been done on correlated electron materials, both theoretically and experimentally. In spite of this effort, it has been very difficult to understand the phenomena occurring in these systems. For example, high temperature superconductivity has been experimentally demonstrated for more than thirty years, and yet no realistic theoretical explanation has been given. The main reason for

this is the complex coupling between the charge, spin and lattice. The competition and interaction of those degrees of freedom is affected by many factors, such as doping and temperature, which lead to complex phase diagrams. The crystal structure of $Fe_3O_4$ is shown in Figure 1.1.

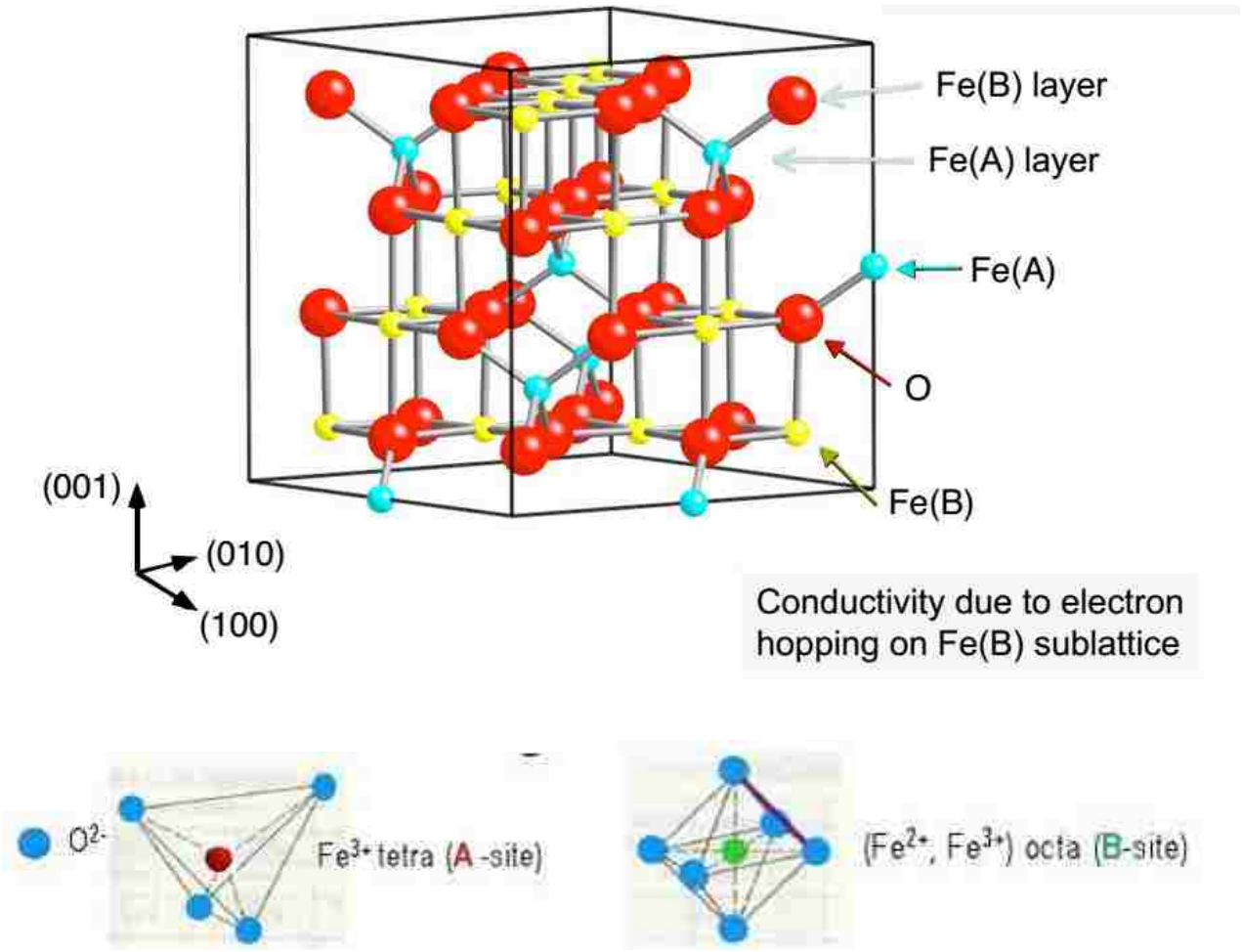


Figure 1.1 (Upper) Side view of the inverse spinel $Fe_3O_4$ structure, where all the A site Fe and half of B site Fe occupy octahedral sites, while the other half of B site Fe occupy tetrahedral sites. Oxygen atoms, Fe(A), and Fe(B) are marked by red, blue and yellow balls. (Bottom) Tetrahedron structure of A site and octahedron of B site Fe is in the center, O atoms are in the corner.

It has inverse spinel structure, space group Fd3m, and lattice constant 9.396 Å.[21] The oxygen anions (red balls) form a fcc sublattice with iron cations sitting in interstitial sites. Two different Fe sites exist in the lattice, labeled as A sites and B sites. A sites are tetrahedrally coordinated and occupied by $Fe^{3+}$ cations, while B sites are octahedrally coordinated and occupied by equal numbers of $Fe^{2+}$ and $Fe^{3+}$ cations.

The electron configuration of Fe is $3d^6 4s^2$. In $Fe_3O_4$, the electron orbital degeneracies are broken by the crystal fields of the octahedron and tetrahedron. As shown in Figure 1.2, in an octahedral crystal field, the electron orbitals are split into two sets of energy levels with an energy difference of ~2.5 eV, where $d_{xy}$, $d_{xz}$ and $d_{yz}$ are lower energy levels, $d_{x2-y2}$ and $d_{3z2-r2}$ are higher energy levels. These levels are decided by the electron charge distribution and ligands orientation. Orbitals $d_{x2-y2}$, $d_{3z2-r2}$ lie in the z direction and *xy* plane and are referred to as $e_g$ orbitals, while $d_{xy}$, $d_{xz}$ and $d_{yz}$ orbitals lie in *xy*, *xz*, *yz* planes and are referred as $t_{2g}$ orbital. Therefore $t_{2g}$ orbitals overlap less with ligands so they have less repulsion and therefore lower energy levels.

On the other hand, $e_g$ orbitals do overlap with ligands, which is not energy favorable. $Fe_3O_4$ is highly spin complex, meaning each level will be filled with one electron first and then filled with electrons of opposite spin, obeying Hund's rule. Figure 1.2(b) shows the electron configuration for $Fe^{3+}$, where all the five energy levels are occupied with one electron of same spin direction. The extra electron of $Fe^{2+}$ will locate at the lower energy level and contribute to the conductivity of $Fe_3O_4$ through hopping to different sites. That's the reason $Fe_3O_4$ is not a semiconductor but a bad metal.

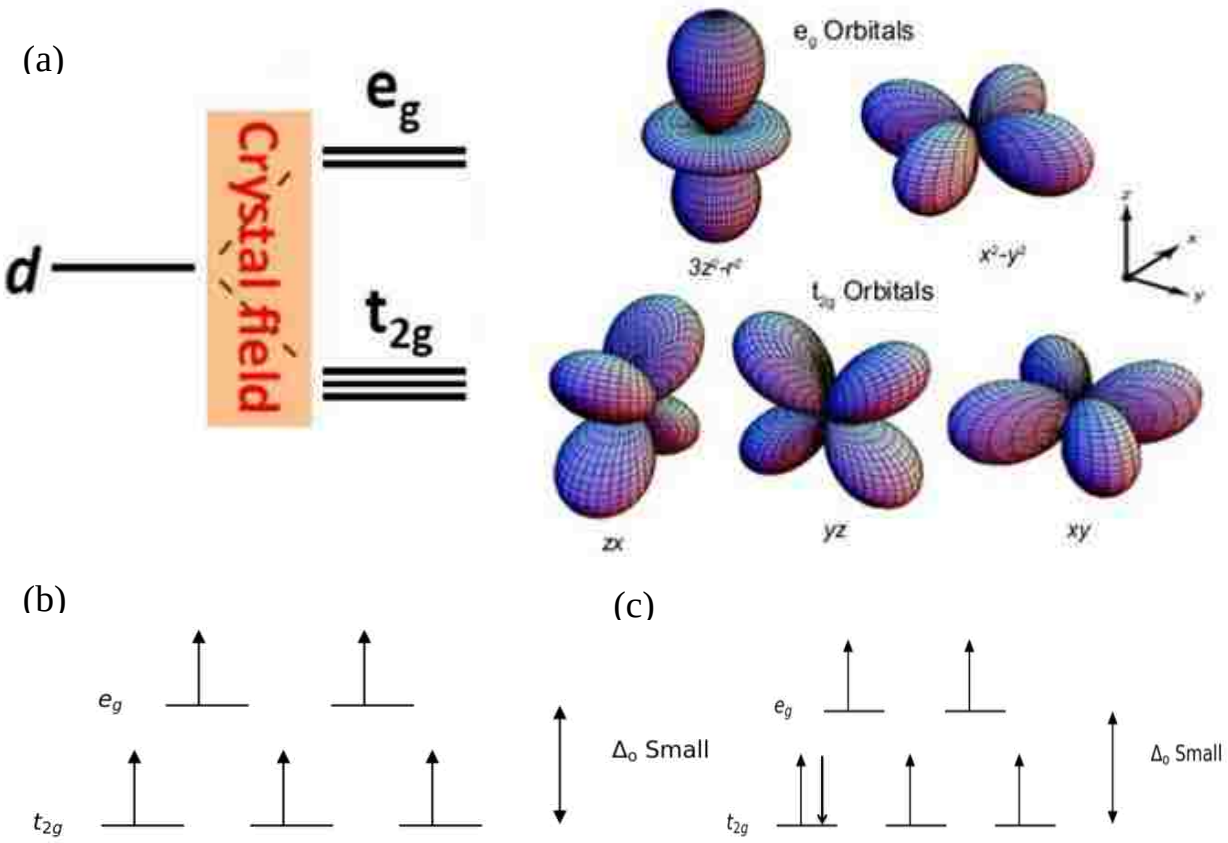


Figure 1.2 (a) Crystal filed splitting lifts band degeneracy into subshells $e_g$ and $t_{2g.}$ In octahedral crystal field, this fivefold degeneracy is lifted to two $e_g$ orbitals and three $t_{2g}$ orbitals (b)(c) Electron configuration of $Fe^{3+}$ and $Fe^{2+}$.

The resistivity of $Fe_3O_4$ is ~$10^{-2}\ \Omega \cdot cm$ at room temperature, which categorizes it as a poor metal when compared to pure iron($10^{-7}\ \Omega \cdot cm$), but is $10^{12}$ better than the conductivity of insulator $Fe_2O_3$.[22] However, in 1939 Verwey observed a decrease of manganite's conductivity by two orders of magnitude at ~120K.[23] This phase transition is named "Verwey transition". As presented in Figure 1.3, during the Verwey transition, not only does resistance jump two orders of magnitude, but many other property parameters also have first order transitions, such as the specific heat, magnetization, and structure.[24]

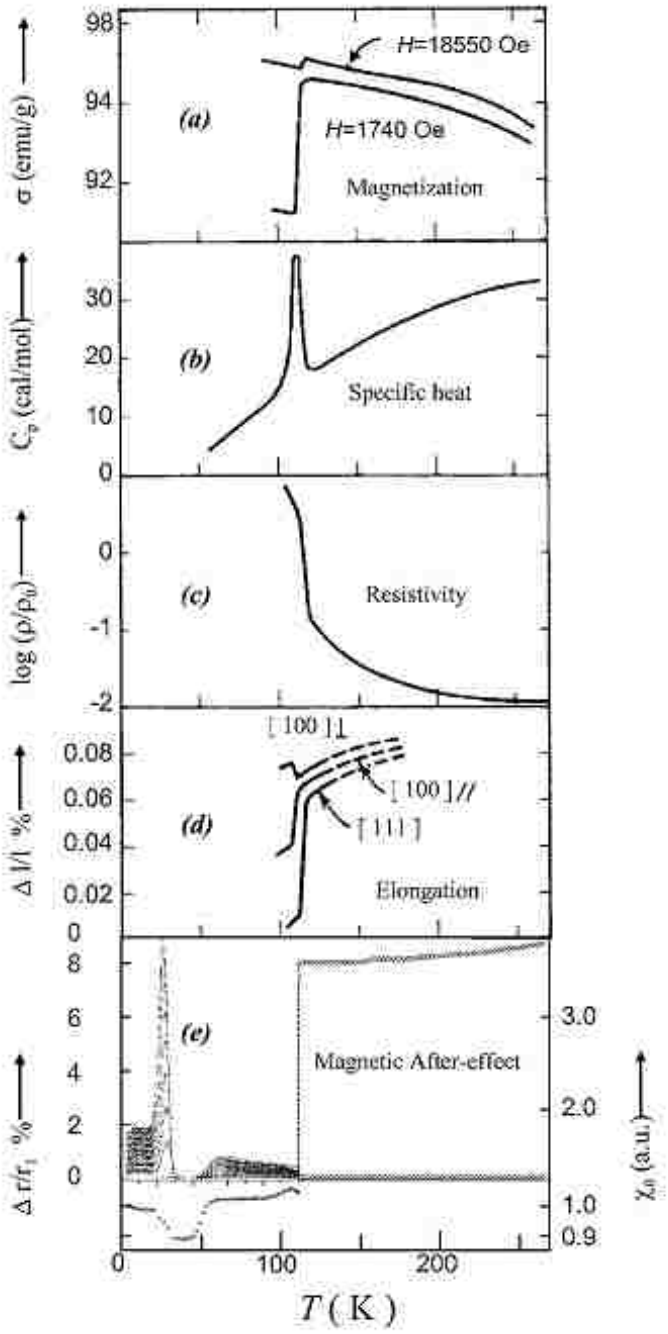


Figure 1.3 Basic manifestations of the Verwey transition in $Fe_3O_4$ near $T_V$ (~125 K), arranged in the historical order of their detection[25]: (a) spontaneous jump of the magnetization[26];(b) specific heat anomaly[27]; (c) spontaneous drop of specific resistivity[28]; (d) thermal expansion along selected directions[29]; (e) MAE spectrum, characterizing the low-temperature phase of perfect magnetite; the transition is indicated by the sudden decay of the relaxation at $T_V$ in combination with a spontaneous jump of the initial susceptibility,$\chi_0$[30-32]. Figure adapted from [24]

Verwey proposed the idea of charge ordering to explain this phase transition.[23] His idea was that at low temperatures, due to strong interaction between electrons and ions, electrons become localized at different sites, which leads to an ordered superlattice. In the case of $Fe_3O_4$, the iterant electrons from $Fe^{2+}$ cations are localized at the $Fe^{2+}$ sites at temperatures below 120K, thus dramatically reducing the conductivity. Although this charge ordering theory has been successful in explaining phase transitions of many strongly correlated materials, it has been proven by X-ray and neutron diffraction that no long range charge ordering exists in $Fe_3O_4$.[33,34] Anderson has suggested that short range ordering may exist during Verwey transitions, which is referred to as a "Fermi glass" with a finite density of states at the Fermi level, but these states are localized.[33] However, the real mechanisms at work in manganite are still unresolved. Magnetite is still attracting intensive research therefore not only because of its application potential, but also its mysterious properties.

There are two possibilities for the surface termination in the (001) direction; A termination or B termination, which are both displayed in Figure 1.4(c). Both terminations are polar surfaces where charge cannot self-compensate, and thus the surface tends to reconstruct. Researchers have observed $\left(\sqrt{2}\times\sqrt{2}\right)R45°$ reconstruction through LEED experiments.[35,36] That is, the unit cell is twice as large as the (1×1) unit cell, and rotated by 45 degree. STM images also reveal the $\left(\sqrt{2}\times\sqrt{2}\right)R45°$ symmetry, seen by the wave-like structures with a periodicity of 6Å, instead of a straight array in the unreconstructed model which has been claimed to be induced by the lateral displacement of Fe atoms.[37] The STM dI/dV spectrum indicates that the surface is non-metallic. Since STM measures the charge density on the surface, this wave-like structure may also be due to a surface charge density wave (CDW).

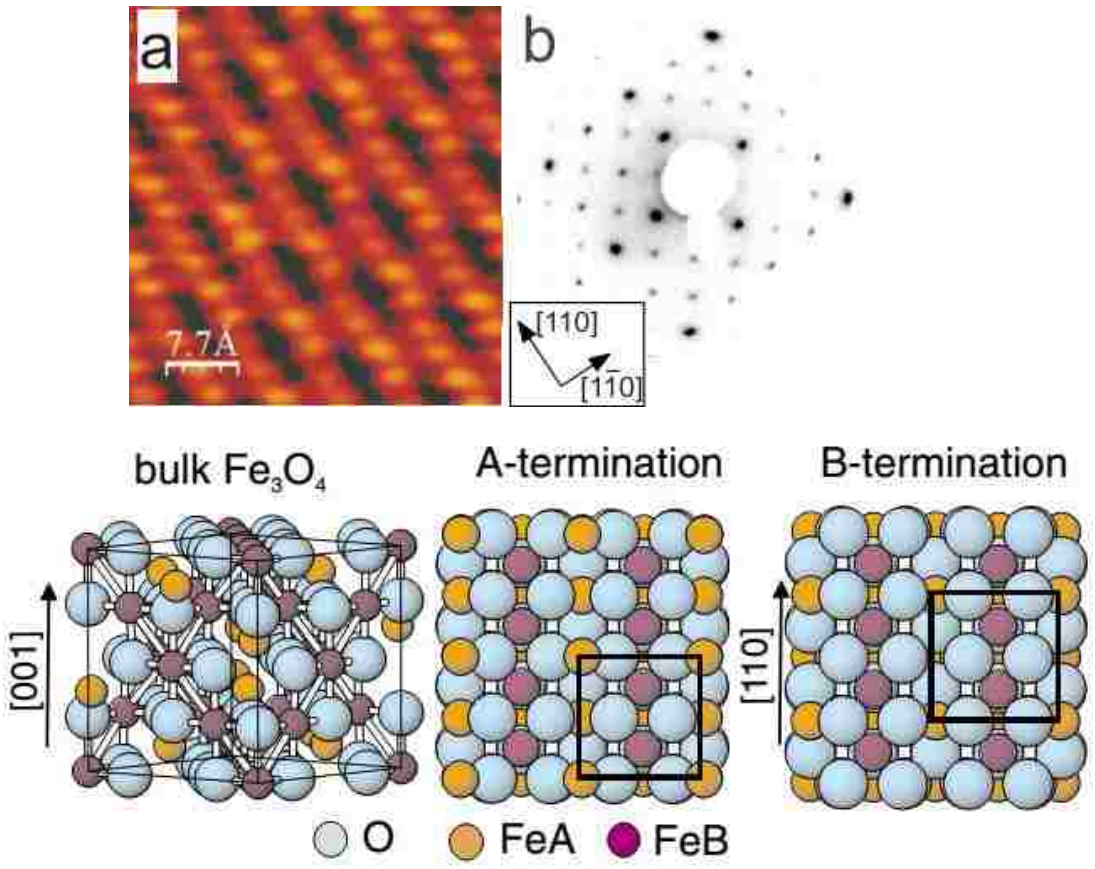


Figure 1.4 (a) STM image ($V_{sample}$= +1.7 V, $I_{tunnel}$=0.14 nA) of clean $Fe_3O_4$ (001) surface, (b) $\left(\sqrt{2} \times \sqrt{2}\right)\boldsymbol{R45°}$ LEED pattern ($E_{beam}$=90 eV) on clean $Fe_3O_4$ surface; (c)The inverse spinel structure of magnetite together with a top view of the two bulk truncations of $Fe_3O_4$ (001) with A and B layer, respectively. Oxygen atoms, Fe(B), and Fe(A) are marked by white (light blue), gray (orange), and black (purple) circles. Figure adapted from [38]

Several models have been proposed to explain the surface reconstruction. Figure 1.5(a) is a surface terminated with a half monolayer of Fe(A); Figure 1.5(b) is a surface terminated with one layer of Fe(B) and tetrahedral O with an oxygen vacancy in each unit cell. The ratio of $Fe^{3+}$ and $Fe^{2+}$ is 3:1 if the surface is non-polar. Figure 1.5(c) is a surface structure derived from x-ray crystal truncation rod (CTR) experiments which can determine atomic structure on the surfaces. In this model, half the ions in the Fe(A) layer are above the neighboring Fe(B)/tetrahedral O plane, drawing their bonded O up with them and leaving the other half lower down in the interstitial sites. Figure 1.5(d) shows the surface termination predicted by molecular dynamics

simulations.[39] It is a modification structure based on Figure 1.5(a), the Fe(A) atom in the top (third) layer swing down (up) along (110) and take empty cation sites in the second Fe(B) and O(A) layer.

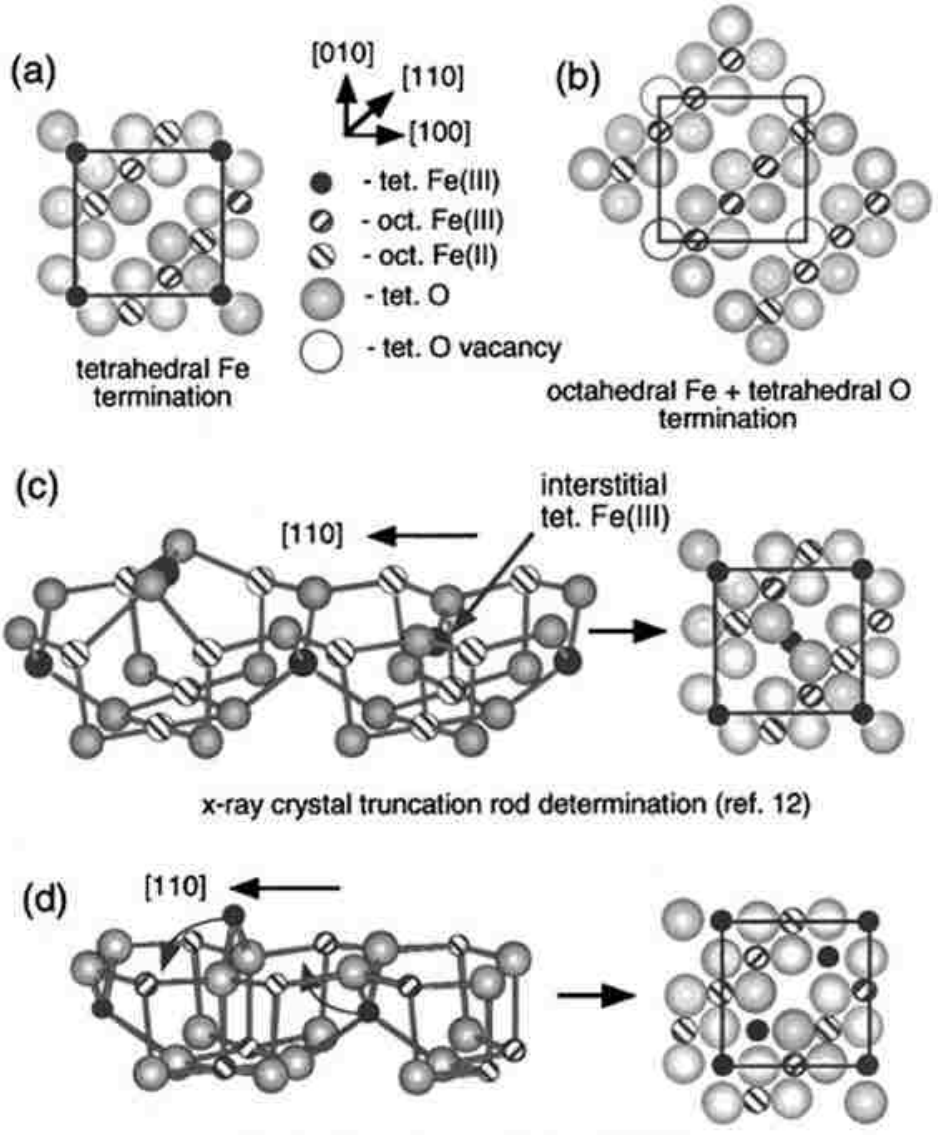


Figure 1.5 Candidate surface structures for $\left(\sqrt{\mathbf{2}} \times \sqrt{\mathbf{2}}\right)\boldsymbol{R45°}$ $Fe_3O_4$ (001) based on a 1/2 ML tetrahedral Fe( III ) terminal layer (a), an octahedral Fe and tetrahedral O terminal layer (b), a preliminary structure derived from CTR experiments[37] (c), and ageometry predicted by molecular dynamics simulations described in [39](d). Figure adapted from [40]

In 2005, Pentcheva predicted another possible surface termination using DFT calculation with *ab initio* atomistic thermodynamics.[41] Her results suggested that a polar modified B termination has the lowest energy possible. As shown in Figure 1.6, this surface termination also

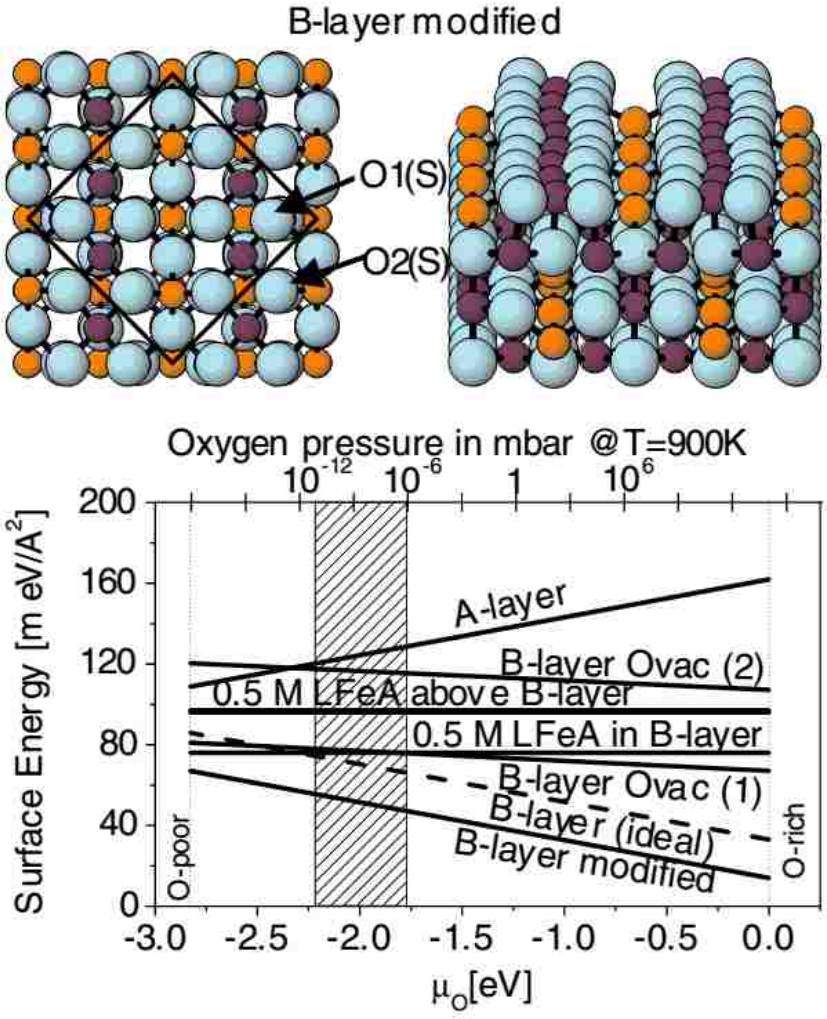


Figure 1.6 Calculated surface free energy $\gamma(T,p)$ as a function of the chemical potential of oxygen (bottom x axis)for all studied terminations. In the top x axis $\mu_O$ is converted into a pressure scale at T=900 K. The vertical lines mark the oxygen-poor and oxygen-rich limits of the oxygen chemical potential. The dashed region marks the range of pressures that were used during sample preparation in the experiment. The B termination with bulk atomic positions and modified positions with a 2p periodicity are marked as ideal and modified, respectively. The B layer with oxygen vacancies above an octahedral iron and next to a tetrahedral iron are denoted by (1) and (2), respectively. Top and side views of the modified B layer are given at the top. Surface oxygens with and without a FeA neighbor are denoted by O2(S) and O1(S), respectively. For the color code see Figure 1.4. Figure adopted from [41]

gives a wave-like structure, which is due to Jahn-Teller distortion.[38] The energy diagram indicates the modified B layer has the lowest energy, where the energy of O vacancies in the model is slightly higher.

At the present time, although most people agree with Pentcheva's model, it has a poor R factor(~0.30) in LEED IV experiments, implying that this model's structure is still lacking.[42] As such, the true surface structure of $Fe_3O_4$ (001) as not yet been fully determined.

## 1.2 Hydrogen Adsorption

As the lightest atom, hydrogen has a very simple structure and is therefore expected to be the simplest adsorbate for absorption investigations. However, it has been seen that studying hydrogen adsorption is complex both experimentally and theoretically due to its high mobility and small size.[43,44]For example, XPS and Auger experiments are not possible due to hydrogen's lack of a core level.

The motivation to study hydrogen adsorption on solid surfaces arises for several reasons. Firstly, hydrogen is involved in many chemical reactions as a reactant or product, and transition metals are usually used as heterogeneous catalysts in these reactions. For example, water gas shift reaction is a widely used method to produce pure hydrogen gas in industry, which was first proposed by Felice Fontana in 1780.[13] Iron oxide and MgO are the catalysts used for this reaction. In Fischer-Tropsch processes, as shown in Figure 1.7, where a mixture of hydrogen and carbon monoxide gas is used to produce liquid hydrocarbons, a variety of transition metals are used as catalysts. For all these industry process, the interaction of hydrogen and the metals or metal oxides play an important role in the reaction. Understanding the mechanisms of hydrogen-metal interactions can increase the reaction rate and catalytic efficiency.

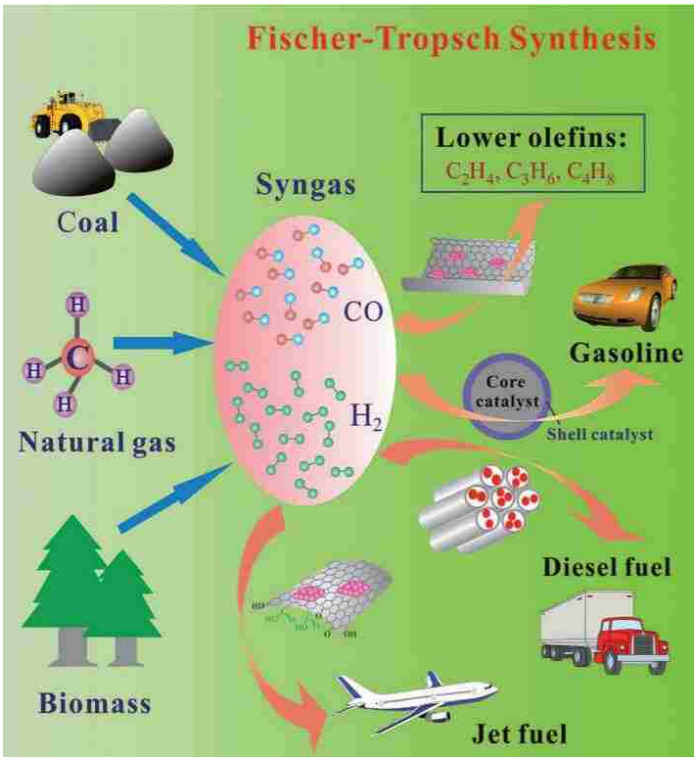


Figure 1.7 The process and production of Fischer-Tropsch synthesis. Hydrogen and CO are the reactants, while magnetite is one of the catalysts. It is an important synthesis method to produce gasoline, diesel fuel and jet fuel.

Secondly, hydrogen is known to cause embrittlement, which is a process that causes metals such as steel to become brittle and possibly fracture and is caused by the penetration and diffusion of hydrogen into the materials. This happens mostly during metal formation and finishing operations. During the embrittlement, hydrogen in the environment is adsorbed on the surface and can then diffuse into the bulk. At high temperatures, hydrogen atoms have more energy to diffuse deeper into the metal. Hydrogen atoms inside the metal can gradually reform hydrogen molecules, creating pressure in the material, reducing the toughness and tensile strength of the metal. If the pressure is high enough, the metal will crack. Figure 1.8 shows a crack caused by hydrogen embrittlement. For example, the East Span of the Oakland Bay Bridge failed testing before opening because of flaws attributed to embrittlement. However, the

elementary steps of this process is not yet fully understood, perhaps even less than heterogeneous catalysis is.

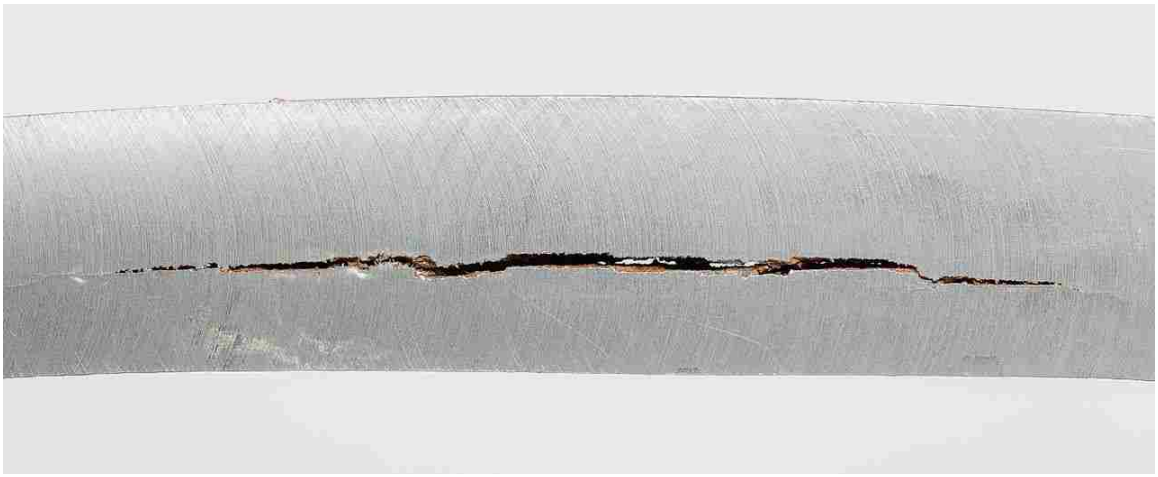

Figure 1.8 Hydrogen induced cracks (HIC)

Third, hydrogen economy is becoming a hot topic.[48-51] Hydrogen is an ideal energy source to replace petroleum in the future. Besides lowering the cost of production, hydrogen storage is another key challenge in the hydrogen economy. Hydrogen can be stored in three formations; (i) cryogenic liquid, (ii) pressurized gas, or (iii) solid fuel when chemically or physically combined with materials, such as metal hydrides, complex hydrides, and carbon materials. The traditional storage facilities are complicated and expensive because of hydrogen's low boiling point (-252.97℃) and low density in gas phase. Therefore, cryogenic storage and pressurized storage require high energy and maintenance costs. Safety issues also make these two methods impractical. Hydrogen storage by chemical adsorption, on the other hand, has the advantage of increased safety because external energy is required to release hydrogen for use. Another advantage of metal hydrides is their storage capacity, which is, perhaps unexpectedly, much higher than that of the other two methods. As shown in Figure 1.9, metal hydrides store nearly twice the amount of hydrogen when compared to liquid hydrogen storage at -423°F. A

drawback to this method is the extra weight created by the hydrogen carrier materials, but the added efficiencies elsewhere make this storage method promising for future energy applications.

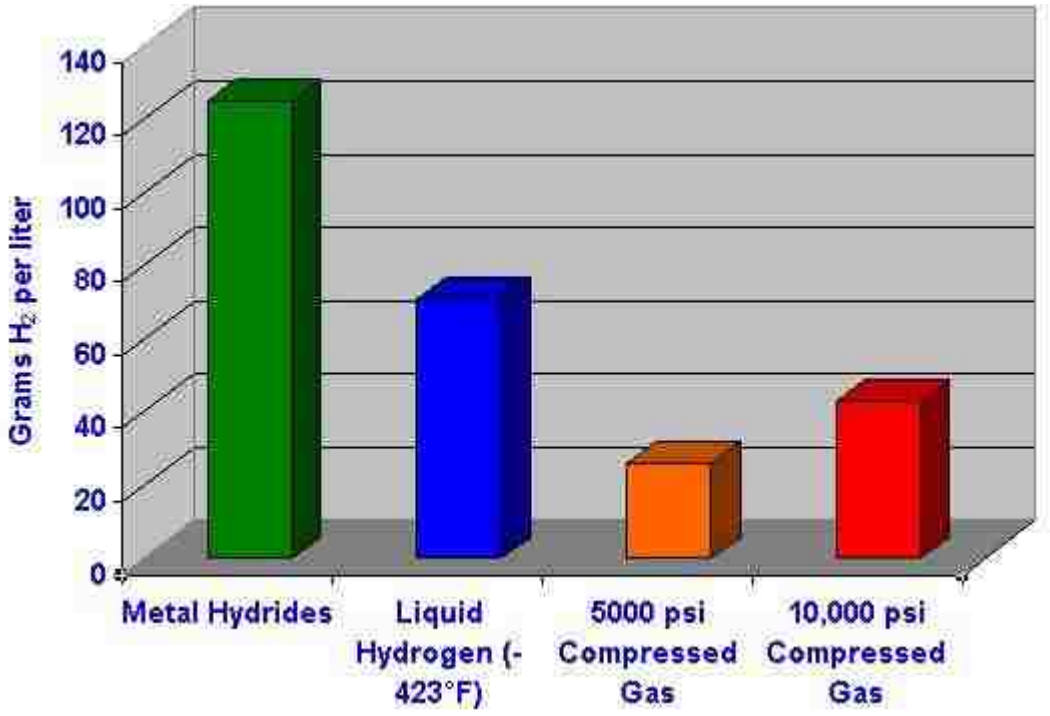


Figure 1.9 Hydrogen storage efficiency comparison between metal hydrides, liquid hydrogen and compressed hydrogen gas. ( http://www.hydrogengas.biz/metal_hydride_hydrogen.html)

To make improvement for all these applications, it is essential to understand the interaction of hydrogen and the solids, especially at their surfaces. The surface is where most of the reactions will happen, and are therefore particularly important. During these surface reactions, hydrogen gas is first dissociated into hydrogen atoms which then interact with other materials. Hot filaments are generally used to experimentally produce atomic H. Hydrogen adsorption on transition metals have been studied extensively with a variety of experimental techniques.[44] However, there are few studies on hydrogen adsorption with metal oxide surfaces, due to its relative complexity. Only the most well characterized single crystals, such as $TiO_2$ or ZnO, have been systematically studied. When metal is exposed to ambient air, most of them are

immediately oxidized, which makes absorption research difficult in metals. Therefore, it is a more realistic to study the interactions between hydrogen and metal oxides.

### 1.3 Previous Results

Parkinson and Kurahashi investigated hydrogen absorption on the manganite surface experimentally in 2010[38,52] while Mulakaluri performed DFT calculation on it in 2012.[53] Both Parkinson and Kurahashi observed LEED pattern changes from $\left(\sqrt{2} \times \sqrt{2}\right)R45°$ reconstruction to (1×1) symmetry after atomic H adsorption. Figure 1.10 shows atomic resolved STM images of the $Fe_3O_4$ surface reproduced from Parkinson, both before and after hydrogen adsorption. Bright paired protrusions are observed on top of iron atoms after hydrogen exposure. He claims that the hydrogen bonds to surface oxygen and therefore reduces surface iron, which produces the higher contrast seen when compared to a clean surface. On the H saturated Fe3O4 surface, nearly half of the surface iron becomes brighter (Figure 1.10(e)). He suggests the Fe(b) row indicated by the dashed line becomes straight, as opposed to the curved line from the clean surface, which therefore explains the LEED (1×1) pattern. However, this conclusion is questionable. First, the 8 atoms under the dash line in Figure 1.10(e) are not completely straight. The higher contrast makes every atom larger in the image, making the curve features harder to see. Secondly, only the 8 atoms indicated by the dash line may be "straight", while all the other bright protrusions are not connected, which could still produce fractional spots in LEED. As said in this paper, Figure 1.10(e) is the saturated surface, so no more bright protrusions could be created by hydrogen exposure. Thirdly, the semiconductor to metal transition upon hydrogen adsorption observed by UPS in this paper has yet to be repeated. Therefore, this explanation of the LEED (1×1) symmetry on hydrogen covered Fe3O4 surfaces is dubious.

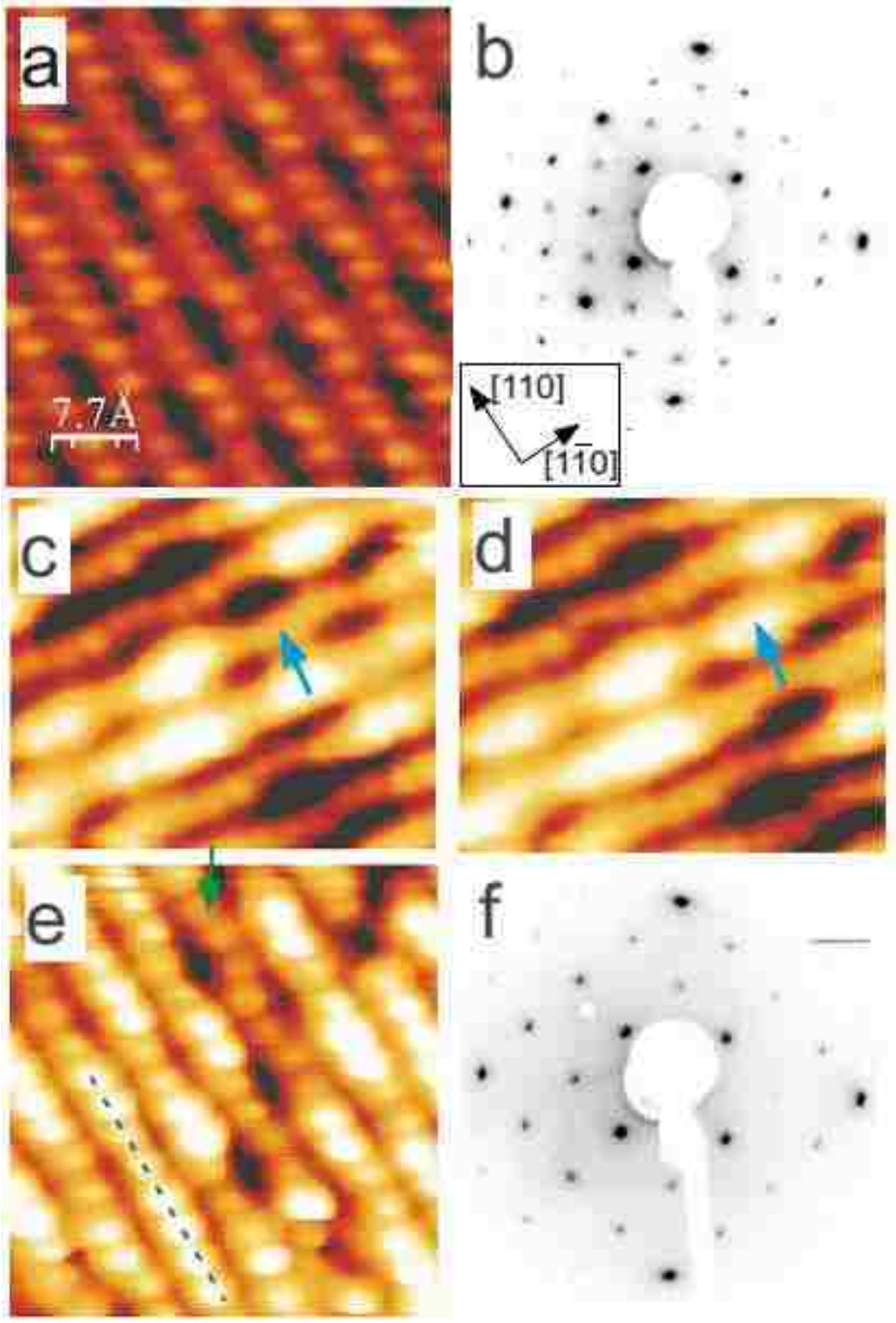


Figure 1.10 (a) STM image ($V_{sample}$= +1.7 V, $I_{tunnel}$=0.14 nA) of clean $Fe_3O_4$ (001) surface, (b) $\left(\sqrt{\mathbf{2}} \times \sqrt{\mathbf{2}}\right)\boldsymbol{R45}°$ LEED pattern ($E_{beam}$=90 eV) on clean Fe3O4 surface; (c) and (d) consecutive STM images at low atomic H coverage. (e) STM image of hydrogen saturated surface. (f) LEED pattern of H saturated surface showing (1×1) symmetry. Figure adapted from [54]

Pentcheva has calculated the phase diagram of hydrogen coverage on $Fe_3O_4$ surfaces as a function of hydrogen and oxygen chemical potential, shown in Figure 1.11. In Parkinson's paper, the hydrogen pressure is $10^{-6}$ Torr during exposure, which corresponds to a saturation coverage of 4 H atoms per unit cell in this environment. Pentcheva also suggested the O-H bonding will strongly tilt parallel to the surface and assist the hydrogen hopping between oxygen sites. The work function is predicted to monotonically decrease with increasing hydrogen coverage.[41]

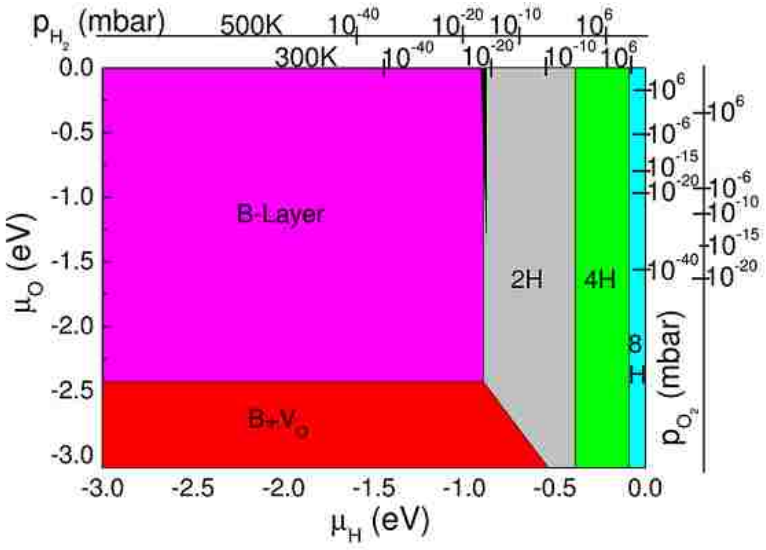


Figure 1.11 Projection of the surface phase diagram of hydrogen adsorbed on $Fe_3O_4$ (001) showing the most stable configurations for given ($\mu_O$,$\mu_H$): B-layer with oxygen vacancies, B+$V_O$(red), distorted B-layer (magenta), single hydrogen, (1H, black), two (2H, gray), four (4H, green), and eight (8H, cyan) hydrogen atoms $Fe_3O_4$ (001). Figure adapt from [41]

Though these three papers suggest that hydrogen bonds to surface oxygen, there is no direct evidence, such as OH vibrational modes. The bright protrusions in STM images can also be explained by H atoms bonded to surface Fe and as such the exact adsorption site has not yet determined. Several predictions from DFT calculation need to be confirmed by experiment as well, such as work function change upon hydrogen exposure. Desorption processes have also not been studied, which can be important for future uses. In this thesis, hydrogen adsorption on the

$Fe_3O_4$ surface is studied with a variety of surface sensitive techniques in an attempt to clarify the nature of the H bond.

### 1.4 Achievements of this Thesis

In this thesis, we have discovered that conventional processed $Fe_3O_4$ (001) is not a stoichiometric surface as people expected. As shown in Figure 1.12, there are significant amount of oxygen vacancies in the surface region. The evidences are presented in Section 3.4 using XPS and HREELS results. Thus previous experimental studies with conventional process method are actually dealing with oxygen deficient surface, not stoichiometric surface they thought. These oxygen vacancies on the CP surface can be removed by ozone treatment. The ozone processed (OP) surface is verified to be close to stoichiometric $Fe_3O_4$ (001) with B termination and $(\sqrt{2} \times \sqrt{2})R45°$ symmetry, described in Chapter 4.

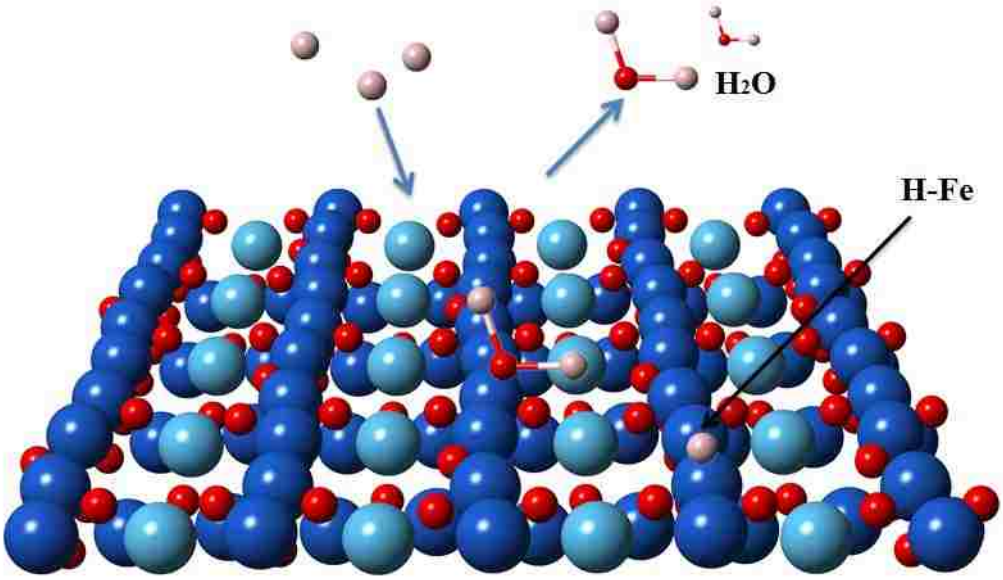


Figure 1.12 schematic view of H adsorption on conventional processed (CP) surface. CP surface is oxygen deficient, H atoms will form water with surface O and desorb, leaving more oxygen vacancies. Those oxygen vacancies can stabilize H-Fe bonding.

These two surfaces present completely different properties. Thus the understanding and explanations of previous reported experimental results need to be reconsidered. For example, the long time contradiction of H adsorption on $Fe_3O_4$ (001) surface between experiments and theories are solved after knowing CP surface is oxygen deficient. It is found that H preferentially bonds to surface Fe instead of O on CP surface, while H bonds to O on OP as expected. The reason of this abnormal H-Fe bonding is determined to be surface oxygen vacancies and a two-step adsorption process is proposed in Chapter 5.

# CHAPTER 2 EXPERIMENTAL TECHNIQUES

## 2.1 Integrated Imaging Functionality Facility ($I^2F^2$) for Measuring the Functionality of Surfaces

Because surface science studies the surface properties of materials, experiments are usually done in a vacuum environment to eliminate effects from contaminations. Based on Langmuir's adsorption model, when a surface is exposed to adsorbate gases of $1\times10^{-6}$ Torr pressure, it takes only one second to cover the surface with a monolayer of adsorbates. [55] This completely changes the surface in question. To obtain a pure surface phase without adsorbates during the entire measurement process, ultra-high vacuum (UHV) is required. UHV is defined as the vacuum region below $10^{-9}$ Torr, or below $10^{-10}$ Torr for strictly surface studies.[56]

A large UHV surface preparation and investigation system was designed and built to enable *in-situ* surface measurements. The base pressure of this system is ~$1.0\times10^{-10}$ Torr, which ensures an unchanged surface during multiple measurements. The system consists of two main chambers, a preparation chamber and an investigation chamber.

As shown in Figure 2.1, the preparation chamber is equipped with an ion source, X-ray source, Ultraviolet (UV) source, Specs 100 hemispherical energy analyzer, Low Energy Electron Diffraction (LEED), two crucible evaporators and a Residue Gas Analyzer (RGA). Clean sample surfaces are achieved by cleavage or sputter-annealing treatment. Only samples with layered structure can be cleaved, while most others require sputter-annealing. In the preparation chamber, the ion source, which is mainly used for Low Energy Ion Scattering (LEIS) measurements, can also be used as a sputter gun to ensure sample cleanliness. The vertical 3 axis manipulator is equipped with a dual stage sample holder, one for cooling (LHe), and another for heating (1000K in $O_2$ environment). The annealing process takes place at the heating stage.

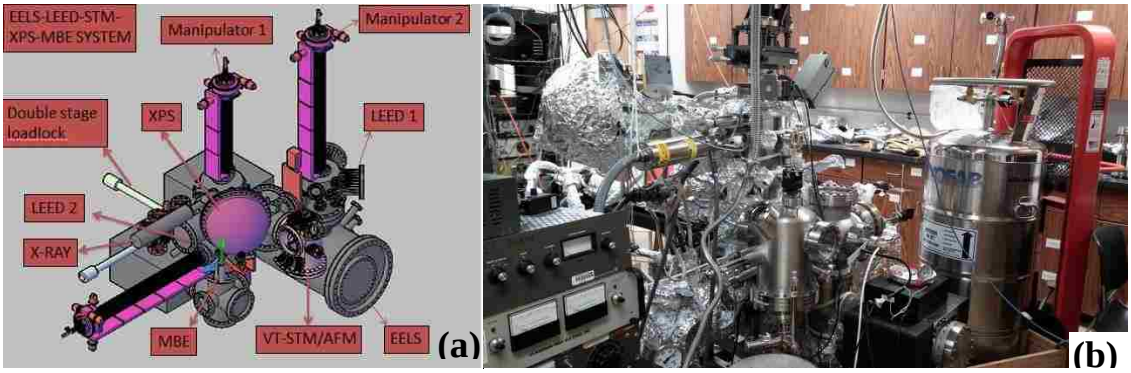


Figure 2.1 (a) 3D drawing of the Integrated Imaging Functionality Facility; (b) Photo of preparation chamber and STM chamber

Beside bulk single crystal surface preparation, Molecular Beam Epitaxy (MBE) thin film growth is also available in this preparation chamber. The MBE system consists of two evaporators, Reflection High Energy Electron Diffraction (RHEED), and a kelvin probe. Substrates are mounted on the heating stage of the vertical manipulator. The ability to reach high temperatures in an oxygen-rich environment is crucial for oxide materials because oxygen vacancies are an important control parameter for this research.

Surface quality checks and some preliminary measurements can also be done in the preparation chamber. Surface symmetry can be measured with LEED, while the surface elementary composition and chemical state can be checked with X-ray photoelectron spectroscopy (XPS), UPS and LEIS. A well controlled clean surface without any undesirable contaminations is crucial for detailed investigations. After a known and reproducible surface condition is reached, samples can be transferred to the investigation chamber.

Our investigation chamber has three powerful surface analysis techniques installed, namely scanning tunneling microscopy (STM), LEED and High Resolution Electron Energy Loss Spectroscopy (HREELS). Since this chamber is mainly used for measurement, the vacuum condition maintained is even better here (~$10^{-11}$ Torr). The whole chamber is Mu-metal shielded. Mu-metal is a Nickel-Iron alloy which has high permeability which shields from static and low

frequency magnetic fields from surroundings, which is important when using highly sensitive electronic equipment such as HREELS and LEED. The vertical manipulator is a 6 axes single stage manipulator, which can be temperature controlled by a Lakeshore controller from Liquid He temperatures to 500K.

**2.2 Low Energy Ion Scattering Spectroscopy (LEIS)**

Low Energy Ion Scattering Spectroscopy ;(LEIS), known as Ion Scattering Spectroscopy (ISS), is a strictly surface sensitive technique (Figure 2.2). It can provide elemental composition information for the topmost layer, while further quantitative analysis can give lattice structure information. LEIS setup usually consists of an ion source and a detector. The ion source produces a fine tunable ion beam, with an energy range from hundreds of electron volts to thousands. Noble gas ions like $He^+$, $Ne^+$, $Ar^+$ are normally used for the ion beam source because these ions are chemical inert. However, reactive gas ions such as $H^+$ and $O^{2-}$ can also be used when studying the interaction between samples and ion sources.

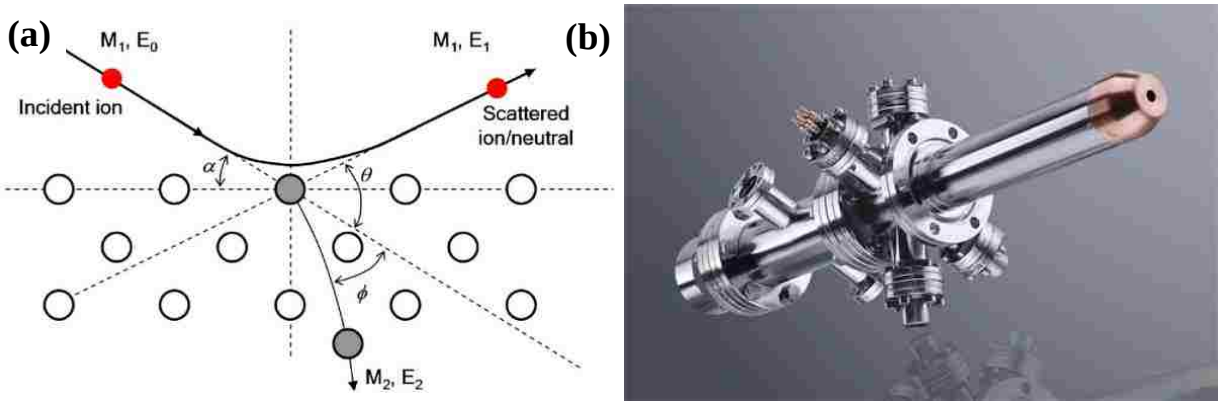


Figure 2.2 (a) Two body elastic collision model. (b) The photo of Specs IQE-12/38 ion source[57-59]

An analyzer, usually hemispherical, is used to detect the energy of scattered ions. By applying a voltage between the outer and inner shells, only ions with selected energy can pass through the detector and reach the channel electron multiplier (CEM). This gives high energy

resolution, but is limited in that only ions could be detected while neutral particles are ignored. Neutral particles can include neutralized incident ions, scattered surface atoms, and gas molecules.

Ion scattering is a complicated process, which includes scattering, sputtering, charge transfer, and photon emission. However, the most critical feature of LEIS is scattering, which can be easily explained using a two-body collision model (Figure 2.2). In this simplified model, only elastic collisions are considered, and the scattered ion only collides once with surface atoms. Therefore, the final kinetic energy of the scattered ion $E_f$ is[60]

$$E_f = \left(\frac{\cos\theta \pm \sqrt{\left(\frac{m_2}{m_1}\right)^2 - \sin^2\theta}}{1+\frac{m_2}{m_1}}\right)^2 \cdot E_0, \text{ eq(1)}$$

Here $m_1$ is the mass of the incident ion, $m_2$ is the mass of the surface atom, $E_0$ is the initial kinetic energy of the incident ion, and $\theta$ is the scattering angle. For a given LEIS system, the scattering angle is usually fixed, and the mass and energy of incident ions are known, so the mass of the surface atoms can be calculated when the final kinetic energy of scattered ions are measured. However, there is an important limitation when choosing incident ion gases. To get a solution from this equation, $\frac{m_2}{m_1}$ must be larger than $\sin\theta$. In other words, to ensure the observation of scattered ions, the mass of incident ion must be smaller than surface atoms, which is another reason He and Ne are typically used in these experiments.

LEIS is a destructive technique. The incident ion beam will sputter the surface atoms away from the surface, so it is critical to know the sputtering rate before performing measurements. The sputtering rate z/t is

$$\frac{z}{t} = M/(rN_A e) \times Sj_p, \text{ eq(2)}$$

Here M is the molar weight of surface atom [kg/mol], r is the density of the material [kg/$m^3$], $N_A$ is Avogadro's number, e is the electron charge, S is the sputtering yield of incident ions [atom/ion], and $j_p$ is the incident ion current density [A/$m^2$]. The sputtering yield depends on the incident ion and target material. For example, if $Ar^+$ is used to sputter an Ag surface, then M=108 g/mol, r=10.49 g/$cm^3$, incident ion energy=0.5 keV, sputter yield S=3, and ion current $j_p$ = 1mA/$cm^2$, yielding a sputtering rate=1924Å/min=192.4 nm/min =11.06 Monolayer/s. This is obviously too fast for LEIS measurements. To lower the sputtering rate, smaller ion currents can be used, while another method is to choose lighter atoms for the gas source. The ion current typically used here is 0.2μA with a beam diameter of 7 mm, which gives an ion current $j_p$ = $5\times10^{-4}$ mA/$cm^2$ and a sputtering rate of 500eV $Ar^+$ on Ag, resulting in a 0.006 Monolayer/s sputtering rate, which is more appropriate. However, one scan of a LEIS measurement usually takes 5 minutes, so the sputtering rate is still too fast compared to the time of measurement. Using the much lighter ion gas $He^+$ produces a sputtering yield on Ag at 500 eV of ~0.282, thus reducing the sputtering rate to $5.6\times10^{-4}$ Monolayer/s, meaning it takes nearly half an hour to sputter one monolayer. In this condition, the surface composition can be considered unchanged during data acquisition.

The mass resolution is the ability of an LEIS system to create peak separations between different atomic masses. For example, the atomic mass of Cu is 63.5 and Zn is 65.4, which are hard to distinguish in LEIS spectra. Most LEIS setups can only observe peak location shifts as a function of the Cu and Zn ratio on the surface. If better mass resolution is required, several methods can be utilized. The mass resolution is a function of scattering angle $\theta$, energy resolute power $\frac{E}{\Delta E}$ and the mass ratio A= $\frac{m_2}{m_1}$,

$$\frac{M}{\Delta M} = \frac{E}{\Delta E} \cdot \frac{2A}{A+1} \cdot \frac{A+\sin^2\theta-\cos\theta(A^2-\sin^2\theta)^2}{A-\sin^2\theta+\cos\theta(A^2-\sin^2\theta)^2}, \quad \text{eq(3)}$$

Scattering angle is usually fixed by the instrument used, and energy resolution of ion beam is limited by the ion source, so the most practical and effective way to improve mass resolution is by choosing the best source gas. According to this formula, the best resolution is reached when the mass ratio A is 1. So $Ar^+$ has much better mass resolution than $He^+$ and $Ne^+$ when resolving Cu and Zn. This can be seen in Figure 2.3. However, as discussed previously, heavier incident ion have higher sputtering rates, thus damaging the surface faster. Therefore, a tradeoff between mass resolution and surface destruction must be made according to the key features to be investigated.

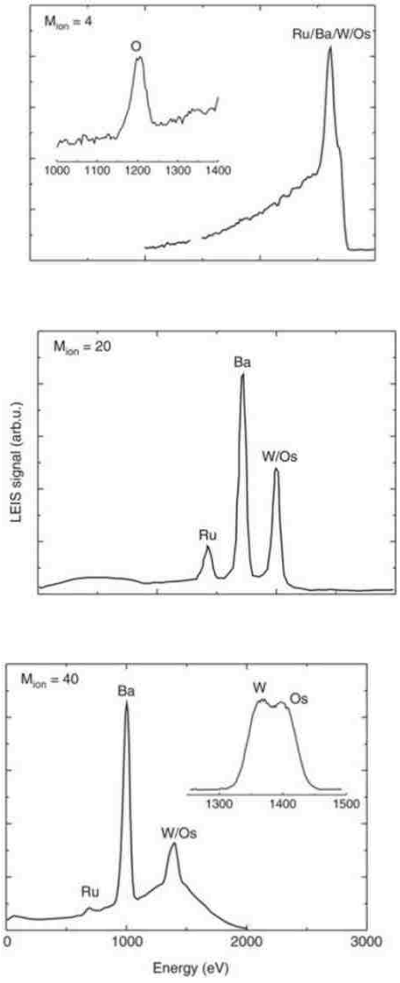


Figure 2.3 Example of the use of different ions to resolve LEIS peaks. Spectra obtained on an Os/Ru layer using 3keV $He^+$, $Ne^+$ and $Ar^+$ beam. Figure adapted from [61]

The shadowing effect is a feature in ion scattering experiments. As shown in Figure 2.4(a), when a parallel ion beam hits an atom, the incident ions will be scattered away and the resultant scattered path is a paraboloid shape cone. In the region of the paraboloid cone behind the scattering atom, no ion atoms exist, while the flux near the edge of this cone is enhanced. The radius of this paraboloid is

$$r = 2\sqrt{\frac{m_1 m_2 e^2 L}{E_0}}, \text{ eq(4)}$$

where L is the distance from the scattering atom.

The shadowing effect can be utilized to do quantitative measurements. As shown in Figure 2.4(b), at large incident angles, the neighboring atom may sit in the shadowing cone, and as a result no ion will be scattered from that atom. At a specific angle when the neighboring atom is located exactly at the edge of this shadowing cone, the amount of scattered atoms will increase dramatically. Since the paraboloid shape and incident angle are known, the distance between neighboring atoms can be calculated. Similarly, the atom distance in the sub-layers can also be determined. This also has important applications in surface adsorption studies. The scattered peak intensities are measured as a function of the sample's in-plane azimuthal angle. The peak locations provide information on the adsorption geometry on the surface, which can be used to determine the exactly adsorption sites.

**2.3 X-ray Photoemission Spectroscopy (XPS)**

XPS is a surface sensitive technique which provides information about core level electrons. XPS is based on the photoelectron effect, which was first discovered by Heinrich Rudolf Hertz in 1887, and later explained by Albert Einstein in 1905.[62] Two years later, P.D. Innes built a hemispherical detector to record the electron kinetic energies produced by this effect, producing what is considered the first XPS spectrum.[63] The first high-resolution XPS

spectrum was recorded in 1954 by Kai Siegbahn on NaCl crystals, who was awarded the Noble prize in 1981.[64] The technique has since been refined further.

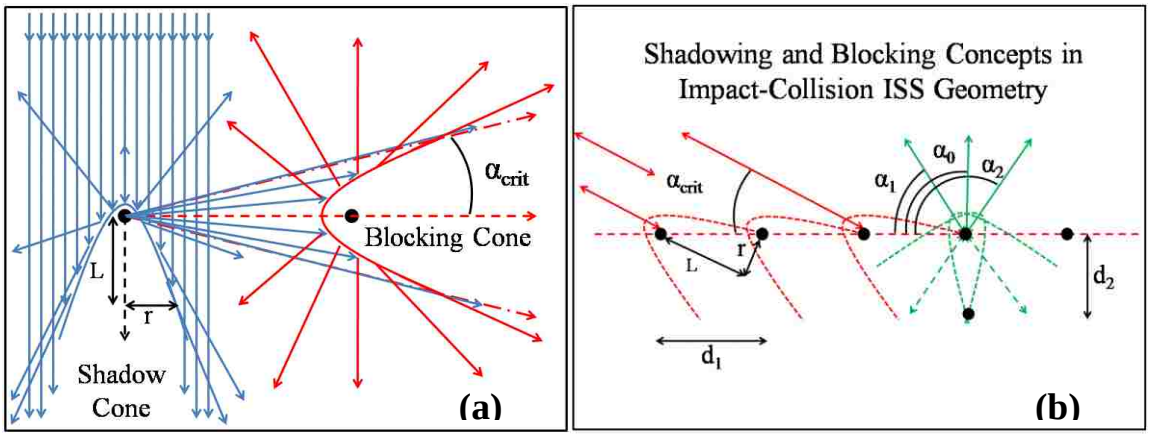


Figure 2.4 (a) Shadowing and blocking effects in two dimensions. No ions will be detected at angles below primary angle when ions are approaching from the upper left. (b) ISS geometry and its relevance to structural characterization of surfaces. The direction and length of the surface-subsurface bond may be determined from an intensity vs. plot. Red: determining the shape of the shadow cone; Green: determining surface-subsurface spacing and direction with a known shadow cone shape.

When X-rays are incident on a sample surface, electrons in the sample can be excited by the X-ray and emitted. The relation between electron binding energy and emitted electron kinetic energy is:

$$E_{binding} = E_{photon} - (E_{kinetic} + \phi), \text{ eq(5)}$$

where $E_{\text{binding}}$ is the binding energy (BE) of the electron, $E_{\text{photon}}$ is the energy of the X-ray photons, $E_{\text{kinetic}}$ is the kinetic energy of the electron as measured by the analyzer and $\phi$ is the work function affected by both the spectrometer and sample. The work function is the energy difference between Fermi level $E_F$ and the energy of vacuum level $E_V$, $\phi = E_V - E_F$. This formula is based on simple energy conservation laws. As shown in Figure 2.5, the Fermi level of the sample and spectrometer are aligned by grounding them. By calibrating with a standard sample, for example the Au 4f peak, the work function of spectrometer can be determined. The

value of the binding energy can then be easily calculated with the kinetic energy measured by the spectrometer. It is obvious that only electrons with binding energy lower than photon energy can be excited. An X-ray source with particular energies (Al $K_\alpha$ 1486.7 eV or Mg $K_\alpha$ 1253.6 eV X-rays) or a synchrotron light source are usually employed to produce X-ray. The emitted electron kinetic energy and intensity are measured by a hemispherical analyzer. Electrons with the same binding energy create a peak in the spectrum.

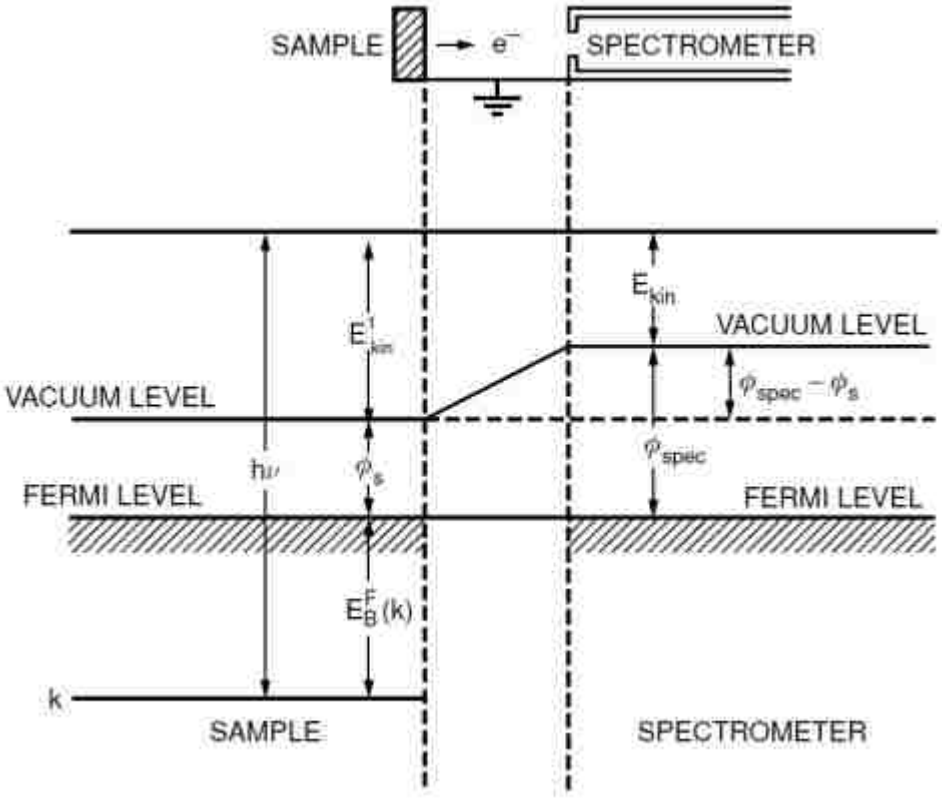


Figure 2.5 Schematic view of photoemission. Figure adapted from [65]

XPS is a surface sensitive technique. Electrons need to escape from the surface, travel through the vacuum, and reach the analyzer. However, after photo-excitation, photoelectrons may undergo elastic scattering, inelastic scattering by the sample or any particles in the path, or can recombine and excite other electrons. All of these could result in a failure of the electron to reach the analyzer and be collected. The average travel distance for a photoelectron can be

estimated by the mean free path, as shown in Figure 2.6. The exact measuring depth relates to the material and the electron energy.

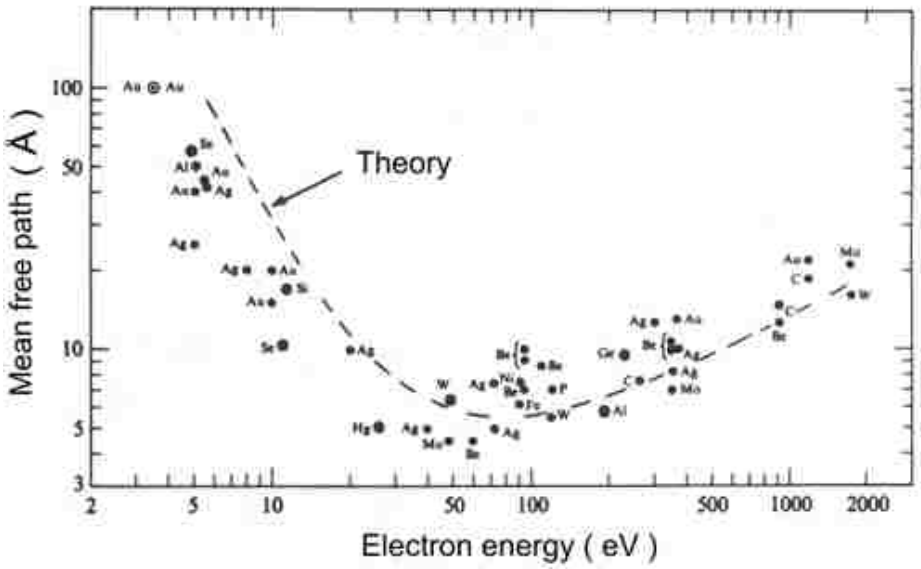


Figure 2.6 Theory predicted mean free path dependence on electron energy (dash line) and experimental data on different materials.

The Beer-Lambert law gives the possibility of an electron traveling distance d without any inelastic scattering:

$$P(d)=\exp(-d/\mathtt{l}(E)), \text{ eq(6)}$$

where $\mathtt{l}$ is the mean free path. In normal emission conditions, it is estimated that electrons from the top 0 to 10 nm can escape from the sample. Therefore, the signal of XPS comes from top a few layers. This is different from LEIS, which only measures the topmost layer. It is important to keep this in mind when analyzing data from XPS and LEIS.

With a rotatable manipulator, it is possible to perform Angle Resolved XPS (ARXPS), which provides information from different layers. With different emission angles, the electron signal will come from different regions. The intensity contribution from a layer of thickness x is given by

$$I_x = I_{tot}[1 - exp - (x/\lambda \cos\theta)], \text{ eq(7)}$$

where $I_{tot}$ is the total photoelectron intensity. According to this formula, at very high (~80°) emission angles, more than 80% of the signal observed is produced from the top layer. XPS can then be much more surface sensitive. The angle resolved measurements also provide information from inside layers by comparing spectrums of different emission angle, which is important for layered materials.

Energy resolution of XPS becomes critical to resolve close peaks. For example, the Fe 2p peaks for $Fe^{2+}$ and $Fe^{3+}$ are located at 709 eV and 711 eV, respectively.[66] Resolving these two different chemical states requires good energy resolution. The intrinsic FWHM of Al $K_\alpha$ X-ray is 0.43 eV, which is not enough to resolve these features. A monochromator is usually used to improve the source energy resolution. A well-tuned monochromator can obtain an Al $K_\alpha$ X-ray of 0.16 eV energy resolution.

Work function measurement is a major application of XPS. The work function is defined as the minimum energy needed to remove an electron from a solid to the vacuum immediately outside the solid surface. It can be expressed by the formula:

$$W = E_V - E_F, \text{ eq(8)}$$

$E_V$ is the energy of electron at rest in the vacuum near the surface, and $E_F$ represents the energy of this electron at the Fermi level.

The work function is not a bulk property, but is related to the material's surface. There are various factors that can affect the value of the work function. For example, on a metal's surface, its close-packed surface tends to have larger work function than open lattice surfaces. Surface reconstruction and contamination can also change the work function.

To measure the work function by photoemission, the region near the Fermi edge and the secondary electron cut off need to be measured by biasing the sample, as shown in Figure 2.7. The work function is then given by

$$\phi = h\nu - (E_{cutoff} - E_{Fermi}), \text{ eq(9)}$$

where $E_{cutoff}$ gives the photoelectron zero kinetic energy, while $E_{Fermi}$ is the kinetic energy of electrons at the Fermi level.

The electrons at the cut off edge have zero kinetic energy, so a bias voltage has to be applied to the sample in order to detect them. For example, when a sample is biased -6 V, the whole spectra (both $E_{cutoff}$and $E_{Fermi}$) will shift their kinetic energy upward by 6 eV, but the value of $E_{cutoff} - E_{Fermi}$ will remain the same. The bias voltage can be chosen depending on the work function of the detector. The secondary electrons are those electrons with multiple energy loss or excitation events. The intensity of secondary electrons are huge; using normal parameters for XPS measurement, secondary electron counts can exceed 2 million per second. This ultra-high count rate can burn the channeltron, so low pass energies (~2 eV) are suggested when doing secondary electron measurements.

It is important to notice that the energy resolution of work function measurements only related to the energy resolution of analyzer and not to the X-ray source. This is because the work function calculation is an edge effect, where only the electrons with highest kinetic energy (Fermi edge) and lowest kinetic energy (secondary electron cutoff) are both involved. Therefore, no matter how broad the X-ray spectra is, only the edge of it is taken into consideration when calculate the work function.

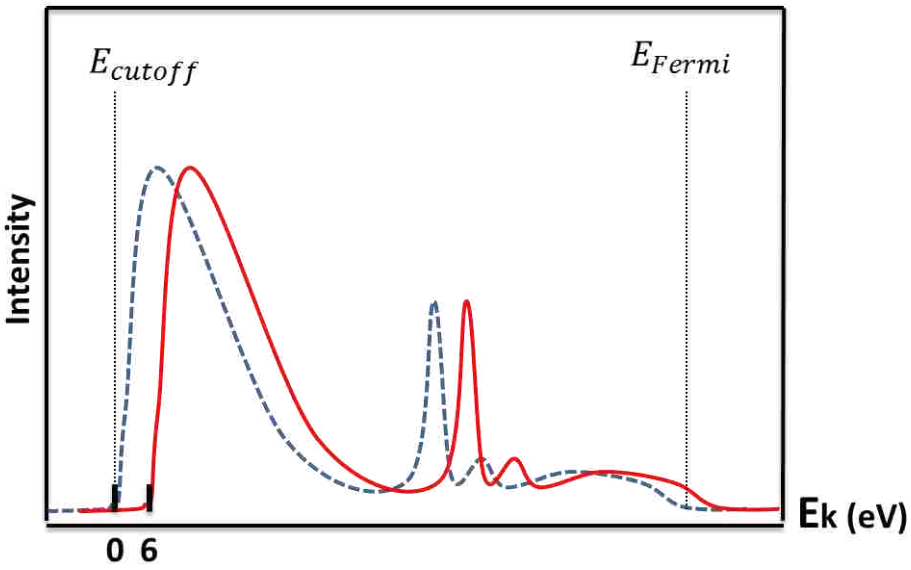


Figure 2.7 XPS spectrum including Fermi edge and secondary electron cut-off edge. Blue spectrum is with zero bias and red spectrum is biased -6 V on sample. The whole spectra shift to higher kinetic energy side after sample bias.

**2.4 High Resolution Electron Energy Loss Spectroscopy (HREELS)**

HREELS is a surface analysis tool used to measure surface vibrational modes and electronic excitations with momentum transfer (Figure 2.8). The measured energy loss range is from 1 meV to several eV. Therefore, it has the ability to investigate surface phonon dispersions, surface plasmas, and adsorption progress.

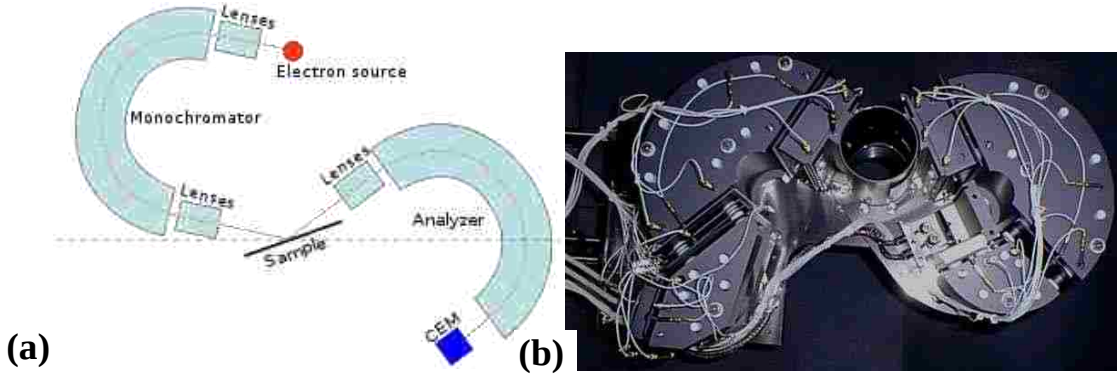


Figure 2.8 (a) Principle of HREELS setup; (b) photo of HREELS set up by LK technology

Since HREELS employs electrons as the source, it requires an UHV environment and zero magnetic field to operate. The low energy of incident electrons ensures this technique is surface sensitive. The instrument geometry is shown in Figure 2.8(a). Electrons are generated by a filament (usually $LaB_6$). The first lens concentrates the electron beam and focuses it to the entrance of the monochromator. The kinetic energy of the electron beam is usually tunable from a couple of eV to ~50 eV. After exiting the monochromator, electrons are focused by another lens and hit the sample. After scattering from the sample surface, the electron beam enters the analyzer. As in the incident beam, there is a lens that focuses the scattered electron beam at the entrance of analyzer, after which the electrons reach the channeltron. This is the classical HREELS setup for high resolution, which can reach 0.5 meV.

Although the resolution of the classic setup is superb, there are several limitations. First, the data acquisition period is long. It takes up to ten minutes for one scan, depending on the settings used such as steps and the scanning scale. Most of the time one scan is not enough because the features of interest may be low intensity and noisy. Therefore, a full HREELS spectrum may take hours. This is an important issue for surfaces whose properties change fast, for example some surfaces are highly reactive and get “dirty” in an hour after cleavage even in UHV environment. In this case, data acquisition time is more important than energy resolution. Also, in the classical setup, tuning is difficult, as it is difficult to find the best conditions for measurement.

To solve these problems, a newly designed multichannel electron energy analyzer is utilized. It uses a wide cylindrical analyzer with multichannel plates for simultaneous data collection over 800 channels. This not only gives 100-150 faster detection efficiency over conventional HREELS, but also provides users a real time view of electron energy distributions

while tuning. However, the resolution is reduced to 1 meV using this setup, making it ideal for measurements where high resolution is not the priority, and has the added benefit of real time reaction measurements.

As mentioned previously, HREELS measures the electron energy loss during interaction with a sample surface because of a momentum transfer. The interactions on the surface are expressed by:

$$E_s(k_s) = E_i(k_i) - h\omega(q_\parallel), \text{ eq (10)}$$

$$k_{s\parallel} = k_{i\parallel} - q_\parallel + G_{h,k}, \text{ eq (11)}$$

Equation 10 portrays energy conservation at the surface, where $E_i(k_i)$ is the incident electron beam with momentum $k_i$, $E_s(k_s)$ is the scattered electron beam with momentum $k_s$, $h\omega(q_\parallel)$ is the energy of the surface excitation and $q_\parallel$ is the momentum transfer parallel to the surface. Equation 11 deal with momentum conservation, where $G_{h,k}$ is a two dimensional reciprocal lattice vector parallel to the surface. This mechanism is shown in Figure 2.9.

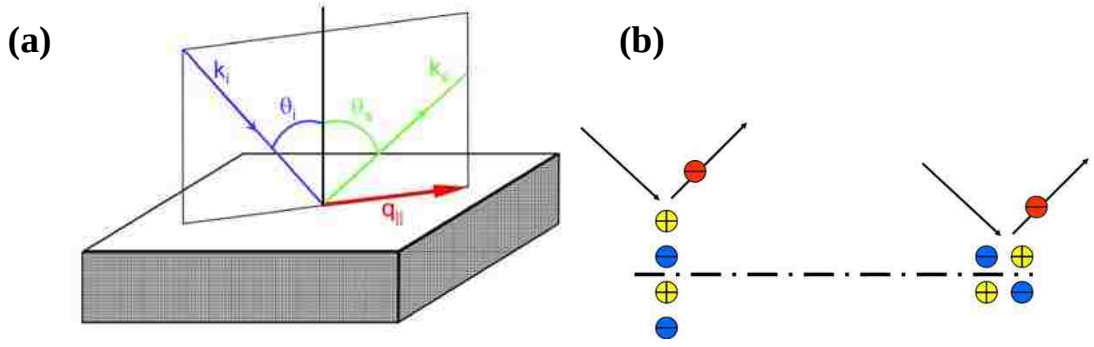


Figure 2.9 (a) HREELS scattering geometry; (b) Figurative Interpretation of dipole scattering

There are two different scattering types, namely dynamic dipole scattering and impact scattering. Dynamic dipole scattering is a long range effect due to the electric field on the surface. Since symmetry is broken on surfaces, there is an electric dipole moment set up on the surface. The incident electron beam is affected by the Coulomb field when far away from the sample

surface, which causes a small angle deflection of the electron beam. Because of this, dynamic dipole scattering dominates the specular direction. When the dipole moment is perpendicular to the surface, it will create an image dipole in the sample. These dipoles add together and effectively double the field seen by incident electron beam. However, if the dipole is parallel to the surface, the dipole moments will cancel out and therefore cannot be seen by the incident electron beam. This is similar to the IR selection rule. The dynamic dipole scattering is only in the specular direction, while impact scattering deals with scatterings at any direction. Impact scattering is a short range interaction.

On some metal oxide material surfaces, the intensity of dipole scattering is very large in the specular direction. Some electrons may undergo multiple scatterings with surface phonons and will introduce overtone peaks as a result. The intensity of the overtone peaks is related to the single scattering peak. Sometimes the dipole scattering is so strong that its overtones are also large, such as in iron oxide, ZnO and $SrTiO_3$ HREELS spectra.

The intense dipole peaks make it difficult to distinguish other phonon peaks, such as the vibrational modes of adsorbates. For example, the first overtone of 50 meV and 80 meV phonon peaks of $Fe_3O_4$ will make the small features around 100 meV and 160 meV energy range invisible. To solve this problem, P. A. Cox has proposed a method using Fourier Transform to deconvolute the overtones.[67]

A HREELS spectrum can be expressed as:

$$s(\omega) = i(\omega) * [\delta(0) + p(\omega) + \frac{1}{2!}p(\omega) * p(\omega) + \frac{1}{3!}p(\omega) * p(\omega) * p(\omega) + \cdots], \text{ eq(12)}$$

where $i(\omega)$ is the instrumental broadening function. The elastic peak can be well fitted by a Gaussian profile, so we usually use a Gaussian with the FWHM of the elastic peak as the

instrument broadening function. $\delta(0)$ is the delta function which represents the elastic peak, and $p(\omega)$ represents the surface loss function.

After Fourier transforming:

$$S(\tau) = I(\tau)\left[1 + P(\tau) + \frac{1}{2!}P(\tau)^2 + \frac{1}{3!}P(\tau)^3 + \cdots\right] = I(\tau)exp[P(\tau)], \text{ eq (13)}$$

Thus,

$$P(\tau) = \ln[\frac{S(\tau)}{I(\tau)}], \text{ eq(14)}$$

Back transformation of $P(\tau)$ will give the spectra without elastic peaks and overtones.

This method was successfully applied to several materials. In Figure 2.10, the HREELS spectrum of a water adsorpt $SrTiO_3$(001) surface was measured. Because of the huge dynamic dipole scattering modes, water vibrational modes at 198 meV and 450 meV are not clear, especially the 198 meV peak, which is totally submerged in the 1$^{st}$ overtone. After FTD, the elastic peak and overtones are almost removed and two clear peaks at 198 meV and 450 meV appear.

The success of the FTD method on $SrTiO_3$ demonstrates that this method has the ability to remove phonon combinations without losing other information. This is extremely important in adsorption studies.

In this thesis, we will see the importance of this FTD method during the HREELS data processing. It successfully unveiled a lot of key features of different sample surface. The detail of FTD source code is in the Appendix section. The code is written with matlab and a GUI is created for easy use.

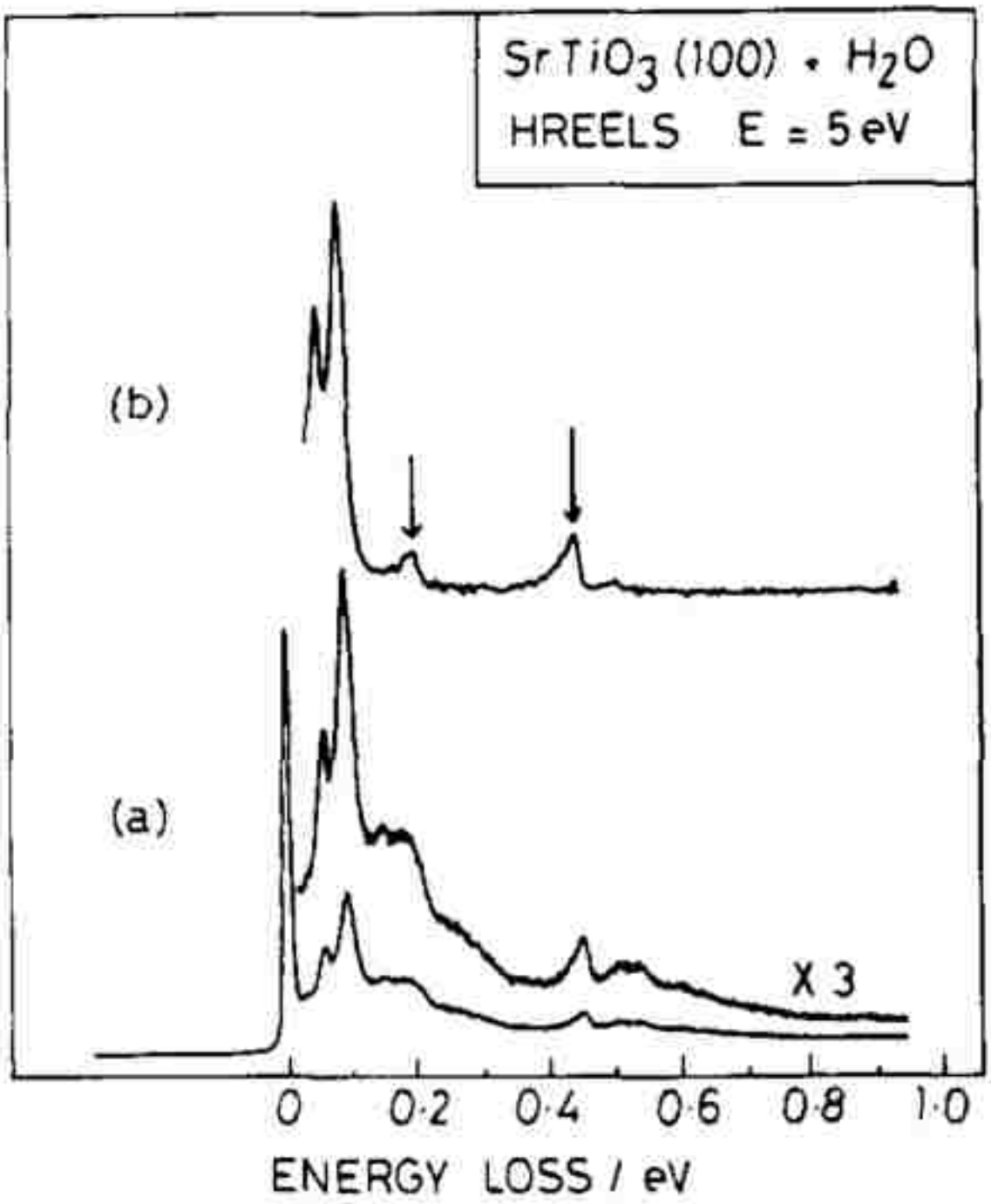


Figure 2.10 (a) Electron energy loss spectrum of SrTiO3(100) dosed with water.[68] (b) Deconvoluted and smoothed loss function with adsorbate induced losses indicated by arrows. Figure adapted from [67]

## 2.5 X-ray Absorption Near Edge Spectroscopy (XANES)

X-ray absorption near edge structure (XANES), also called near edge X-ray absorption fine structure (NEXAFS), is a form of X-ray absorption spectroscopy (Figure 2.11). The studied region probes above the electron core level binding energy. It was first used by A. Bianconi at the Stanford Synchrotron Radiation Laboratory (SSRL) in 1980.

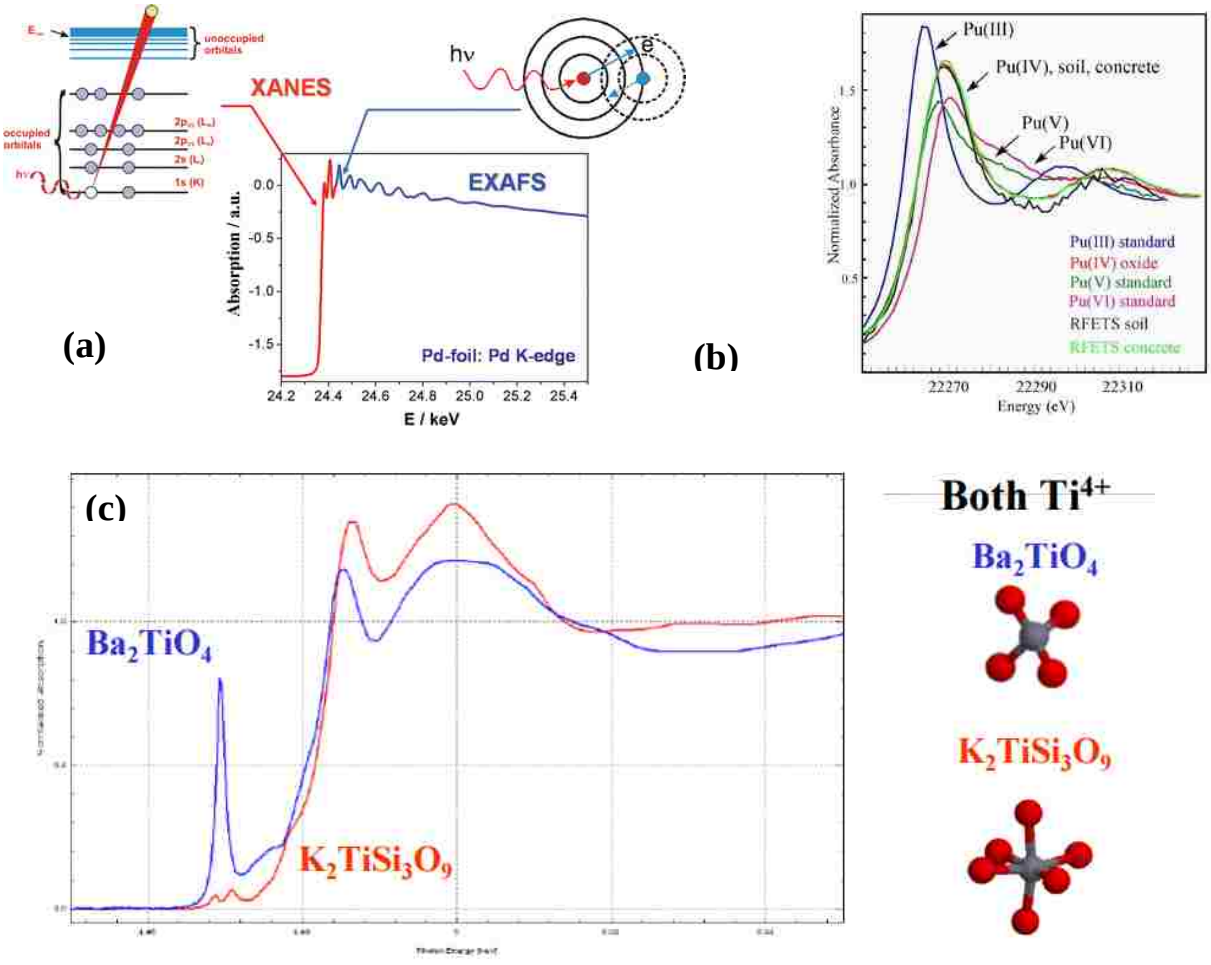


Figure 2.11 (a) Principle of XANES (b) XANES of Plutonium in soil, concrete and standards of different oxidation states (c) Ti K edge spectrum shows dramatic dependence on local coordination environment. Figure adapted from [69]

XANES measures the electron excitation from core levels to unoccupied states. As shown in Figure 2.11(a), the 1s electron is excited to the empty states above the Fermi energy by absorbing the energy from incident X-ray, which creates an absorption peak in the spectrum. If the excited electron is excited from the first shell, the peak is called K edge, whereas if it is from the second shell, it is called L edge.

XANES consists of pre-peak and edge parts. Pre-peak, as shown in the blue spectrum in Figure 2.11(c), is caused by the electron's transition from a core level to the bound states, such as empty 3d states. Although the 1s to 3d transition is forbidden by selection rules, it may still be observed due to 3d and 4p orbital mixing. Pre-peak measurements can provide local geometry information around the absorbing atoms. For example, in Figure 2.11(c), Ti atoms are 4+ valence in both material, but the structures are noticeably different. One is tetrahedral while the other is octahedral, which leads to different XANES spectrum, especially in pre-peak measurements. Edge measurements come from the threshold energies for electron transitions from core levels to continuum empty states. This effect is sensitive to the oxidation state of the surface. Main edges will shift to higher energy with increased oxidation states. As shown in Figure 2.11(b), for different Pu compounds with Pu oxidation states ranging from 3 to 6, the XANES edge shift continues to higher energy. In summation, XANES is an technique sensitive to both oxidation state and local geometry

Because the incident energy of X-rays depend on the binding energy of the studied electron band, the X-ray energy needs to be tunable. Synchrotron light is an ideal X-ray source for XANES, not only is it tunable, but is also highly polarized and bright, has a wide energy spectrum, and emits in very short pulses. Figure 2.12 shows the schematic view of it.

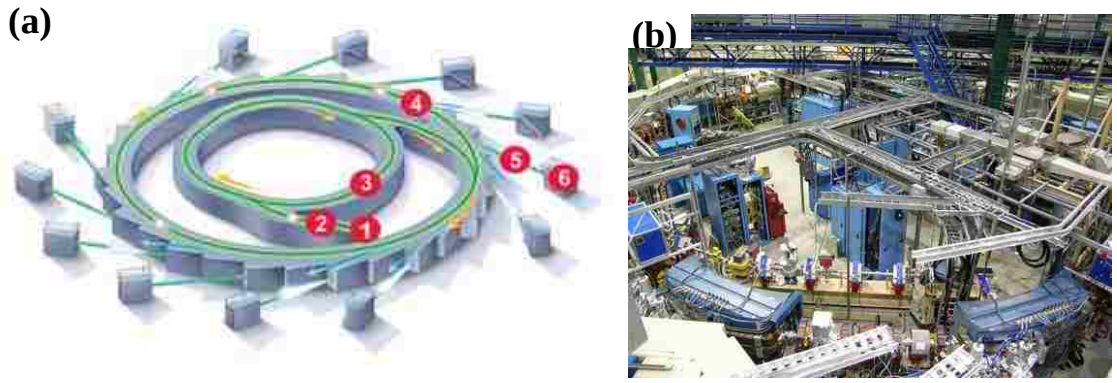


Figure 2.12 (a) A schematic view of a synchrotron ring, (1) electron gun, (2) Linear acceleration, (3) booster ring, (4) storage ring, (5) beamline, (6) end station (b) The synchrotron ring of Center for advanced microstructure and devices (CAMD);

The synchrotron light is produced by the electromagnetic radiation emitted when electrons are accelerated by the magnetic field. The emitted synchrotron light is forward along the tangent direction of the electron's orbit. The light is extremely intense and forms a narrow cone in the emitted direction. The energy is tunable from infrared light to hard x-rays. The light is highly polarized, which can be linear, circular or elliptical.

Usually a synchrotron source consists of an electron gun, linear accelerator, booster ring, storage ring, beam lines, and end stations. The electrons generated by the electron gun are first accelerated by the linear accelerator to 99.9997% of the light speed. In the linear accelerator, the electrons are accelerated by a microwave field. The electron beam is then forwarded to the booster ring, which further accelerates the electron beam. The booster can induce speeds that are 99.9999985% of the light speed after delivering energies ranging from hundreds of MeV to several GeV. There are two main components in the boost ring, one being the dipole magnets used to direct the electron beam and the other being the quadruple magnets which focus the electron beam. When electrons have enough energy, they are transferred to the storage ring. Once in the storage ring, electrons can remain circulating from 4 to 12 hours and will produce

photons when they change direction. The entire synchrotron ring needs to be in a UHV environment to avoid electrons colliding with atoms or molecules in the ring.

All XANES measurements take place at the Varied-Line-Space Plane Grating Monochromator Beamline (VLSPGM) beam line at Center for Advanced Microstructures & Devices (CAMD) at LSU. Plane Grating has the advantage of a wide energy range and high resolution. This PGM is an SX-700 type monochromator, whose working energy range is 200-1200 eV. This VLSPGM is designed for a resolving power of 20000-8000 at photon energies from 200 eV to 1200 eV, which meets the requirements of XANES experiments.[70]

**2.6 Low Energy Electron Diffraction (LEED)**

Low Energy Electron Diffraction (LEED) can be used to determine surface structures. It uses an incident low energy electron beam (20 eV to 500 eV) to image back diffracted electrons on a fluorescent screen. The diffraction pattern on the screen provides information on surface structure symmetries. Quantitatively, the intensity of each spot on the screen can be recorded as a function of incident beam energy generating the LEED I-V curve. By comparing the measured values with theoretically calculated curves, the precise atomic positions on the surface can be identified. Pendry R-factors are used to quantify the difference between experiment and theoretical models. Usually an $R<0.3$ is considered to be an acceptable value.

The observance of electron diffraction was first reported by Clinton Davisson and Lester Germer at Bell Labs in 1927.[71] However, the technique of LEED was not widely used until the 1970s for several reasons. Similar to other surface techniques, LEED also requires a UHV environment. LEED is also sensitive to surface preparation, needing a well ordered region to observe sharp, low background LEED patterns. As shown in Figure 2.13(a), the experimental setup for LEED is relatively simple. There is an electron gun that produces the low energy

electron beam, four grids to filter electrons undergoing inelastic scattering on the sample, a fluorescent screen to image the diffracted electrons, and several lenses to focus the electron beam.

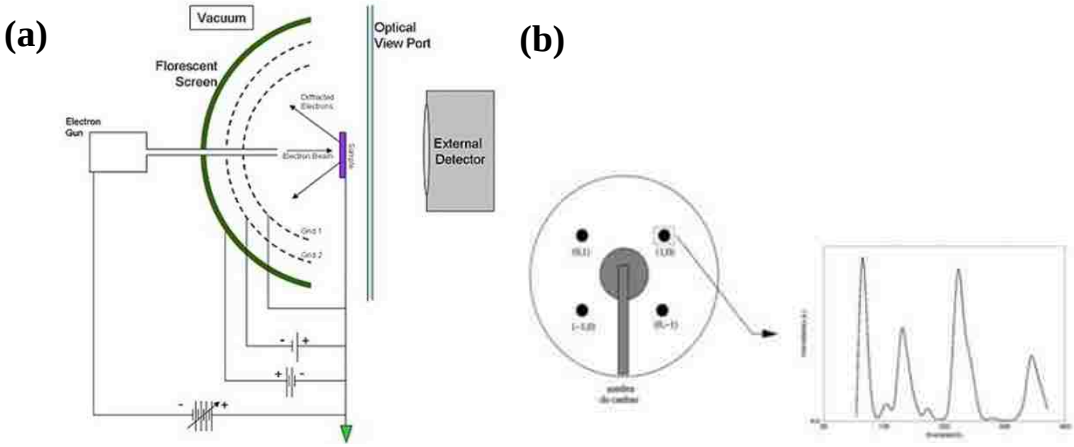


Figure 2.13 (a) Schematic view of LEED setup (b) LEED-IV curve of (1,0) diffraction spot

# CHAPTER 3 H ADSORPTION ON CONVENTIONAL PROCESSED (CP) $Fe_3O_4$ (001) SURFACE

## 3.1 Surface Preparation and LEED

To achieve a clean ordered $Fe_3O_4$ surface, several cycles of sputtering and annealing processes are required.[38,72] $Ar^+$ and $Ne^+$ are commonly used for ion sputtering. Sputtered surfaces are clean but also rough, so in order to rectify this, further annealing of the sample to ~900K yields a smooth surface. It is important to note that oxygen vacancies play a crucial role in metal oxide materials.[73] The properties of oxygen defective surfaces and stoichiometric surfaces are often very different. Therefore, an oxygen-rich environment during annealing is required to avoid oxygen vacancies on the surface or in the bulk. This method successfully produces some stoichiometric metal oxide surfaces, such as $SrTiO_3$. In the case of $Fe_3O_4$, previous STM and LEED experiments reported that perfect $Fe_3O_4$ B layer surfaces are obtained after cycles of sputtering and annealing in oxygen.[40]

Following this conventional surface preparation method, a sharp $\left(\sqrt{2}\times\sqrt{2}\right)R45°$ reconstruction pattern was observed by LEED. As seen in Figure 3.1, fractional spots are clearly observed, but have lower intensity compared to the integral spots. A line profile taken from this LEED pattern quantitatively displays the spot intensity. It can be seen that the background intensity of the LEED pattern is low compared to the peak intensity, which means the conventional treatment successfully created a well ordered surface. A detail Intensity-Beam Voltage analysis presented later will give more information about the surface structure of CP clean surface.

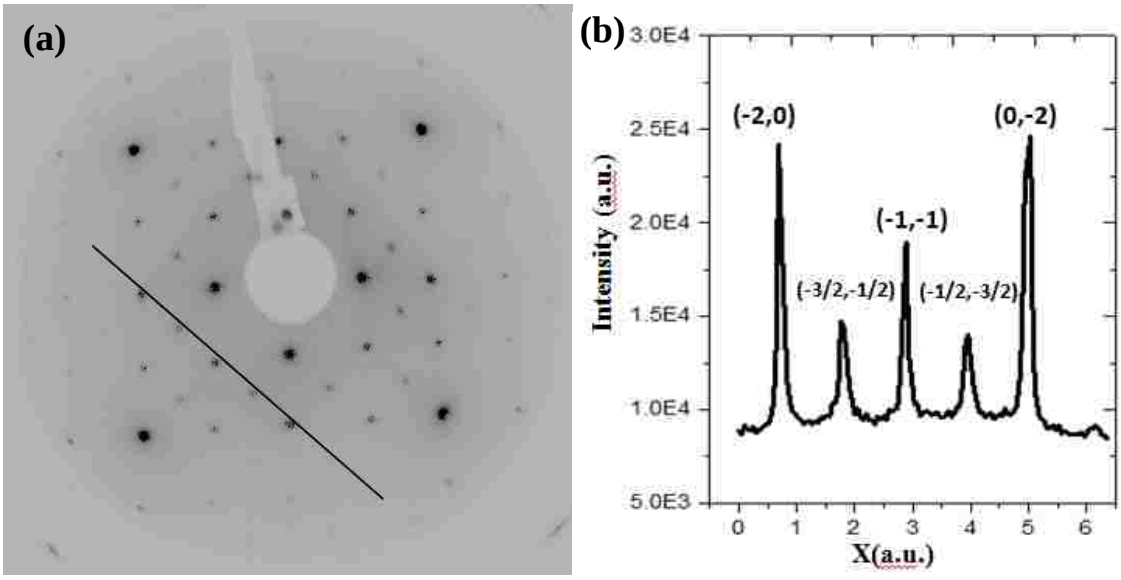


Figure 3.1 (a) $\left(\sqrt{\mathbf{2}} \times \sqrt{\mathbf{2}}\right)R45°$ LEED pattern of conventional treated $Fe_3O_4$ (001) surface. Beam energy is 90 eV, sample surface was cooled down to room temperature after annealing. (b) line profile of this LEED pattern.

To investigate the interaction between a $Fe_3O_4$ (001) surface and H, atomic hydrogen is produced and exposed to the sample surface. Research purity (99.9999%) hydrogen gas is leaked into the UHV chamber through a high precision leak valve. The gas pressure in the chamber is maintained at $1\times10^{-6}$ Torr during reactions. A tungsten filament is used to dissociate hydrogen molecular gas into atomic hydrogen. The hydrogen dissociation temperature is about 3000K, as reported by Langmuir.[74] The tungsten filament is visibly white hot during dosing.

The LEED pattern of the hydrogen saturated surface at room temperature is shown in Figure 3.2. As previously reported, fractional spots disappeared after hydrogen saturation.[38] Background was also increased, indicating the hydrogen covered surface is not as well ordered as a clean surface. Surfaces with different hydrogen exposure times are also investigated with LEED. After 240L of atomic hydrogen exposure, fractional spots are nearly invisible. However, line profiles still show a small peak at the location of fractional spots, meaning surface

reconstruction is not fully removed. Through continued dosing of atomic hydrogen to ~1000L, fractional spots are seen to completely disappear.

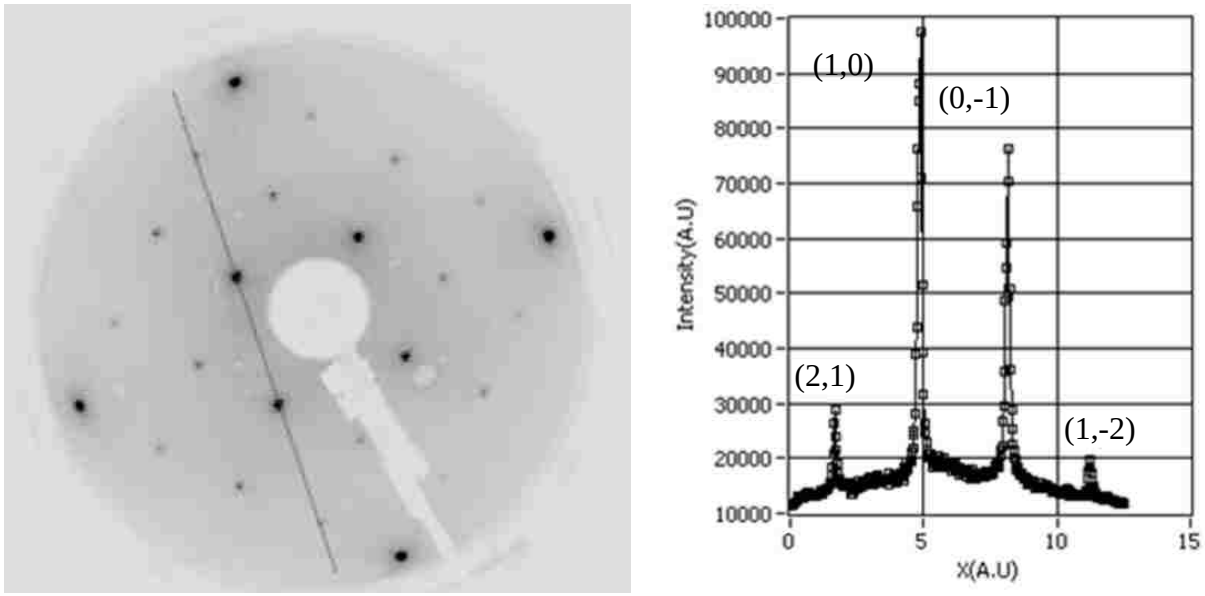


Figure 3.2 LEED pattern of H saturated surface and line profile. Electron beam energy is 90 eV, measured at room temperature.

Previous STM studies report that the "zigzag" iron atom stripe turns into a straight line after hydrogen saturation, which would explain the changes in LEED observations.[54] If the surface Fe atoms change site, LEED IV curves should show apparent differences. However, as shown in Figure 3.3, the peak locations and relative instensity of the (1,0) diffraction spot does not have any signaficant change. Similarly, LEED IV curves at other interal spots like (1,1) and (2,0) are also observed to remain the same after hydrogen exposure. This could be due to LEED IV being more sensitive to displacements along the c direction (perpendicular to the surface), while surface Fe atom may have lateral displacements. The adsorped hydrogen atoms are too small to affect the diffraction electron beam, so they have little contribution to the LEED pattern.

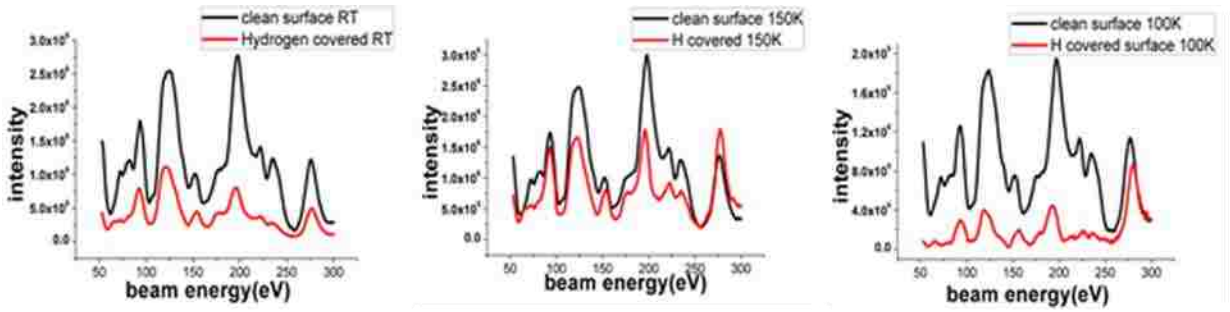


Figure 3.3 LEED I-V curves of clean and hydrogen saturated $Fe_3O_4$ (001) surface. The three experiments are performed at room temperature, 150K, and 100K respectively.

Temperature is a major factor in an adsorption experiment. Some species only adsorb on the surface at very low temperature, and desorb quickly after small amounts of heat are added. Chemical adsorptions usually have higher desorption temperatures because it requires high energies to break the chemical bonding between surface atoms and adsorbates. Although hydrogen exposure at room temperature on an $Fe_3O_4$ surface is already known to absorb, it is beneficial to investigate how temperature affects the adsorption. According to our experiments, hydrogen adsorption at 150K and 100K yield similar LEED patterns when compared to room temperature. LEED IV curves are also similar before and after hydrogen adsorption, but the intensity is lower after hydrogen adsorption, which is not surprising because the LEED pattern background is increased. A complete comparison of LEED IV curves at (1,0) and (0.5, 0.5) spots between different conditions are not shown here. Most of the calculated R factors are below 0.3, indicating little surface structure change. The R factor of the hydrogen covered surface at 100K is relatively high because the surface was degraded after multiple cycles of experiments. This can be seen in the LEED pattern, which has much higher background, and leads to the relatively low IV peak in figure.

According to the LEED experiments, hydrogen adsorption on $Fe_3O_4$ (001) at different conditions result in similar phenomenon. Hydrogen adsorption could gradually remove surface

reconstruction at room or lower temperature, but the IV curves do not show large differences after hydrogen adsorption.

Despite several studies of hydrogen adsorption on $Fe_3O_4$ surfaces, there is no data on hydrogen desorption in this report. Desorption process could provide useful information, such as bonding type and bonding strength.

The hydrogen saturated $Fe_3O_4$ sample are heated to various temperatures for 10 minutes, then returned to room temperature for the LEED experiments. The temperature variations are available in 50K steps though here only 300K, 500K and 700K values are used. As displayed in Figure 3.4, the sample still shows (1×1) symmetry after being heated to 550K, and the $(\sqrt{2} \times \sqrt{2})R45°$ reconstruction fractional spots start to appear after heating to 700K. Hydrogen desorption temperatures are usually relatively low, but the surface recovery temperature here is close to the annealing temperature, which points to annealing effects recovering the surface structure. Although LEED cannot tell us when hydrogen desorbed, the surface after hydrogen desorption is different from after the adsorption. Hydrogen desorption will not recover surface reconstruction automatically, and annealing is needed to recover the $(\sqrt{2} \times \sqrt{2})R45°$ reconstruction.

### 3.2 High Resolution Electron Energy Loss Spectroscopy (HREELS)

Previous STM study has observed bright protrusions on the Fe atom arrays after hydrogen adsorption.[38] Since STM images the charge density states on surfaces, these bright protrusions indicate hydrogen has changed the charge density states of Fe. It is natural to assume hydrogen bonds to surface oxygen and forms hydroxyl. This is also the conclusion of Parkinson's STM paper, where he finds that hydrogen and surface oxygen form hydroxyl and therefore reduce surface $Fe^{3+}$ to $Fe^{2+}$.[54] This is a reasonable explanation, yet it lacks sufficient

evidence such O-H vibrational modes, and the mechanism of surface reconstruction being removed is not sufficient.

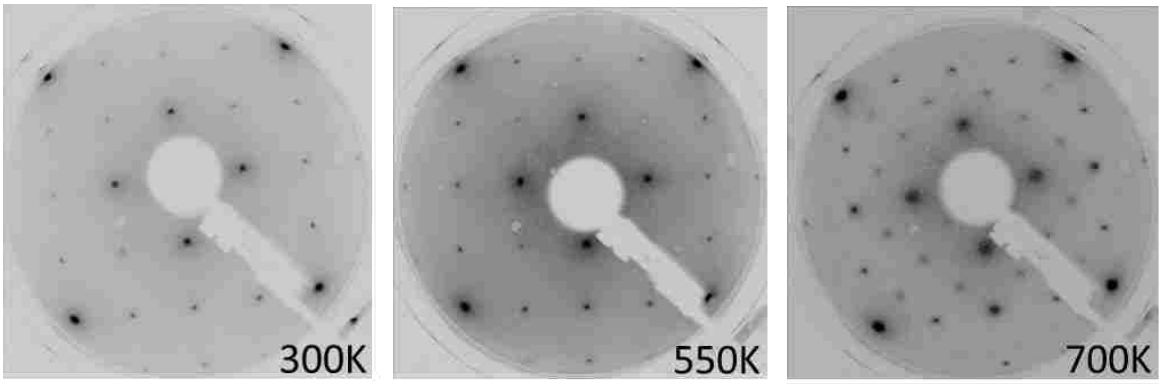


Figure 3.4 LEED pattern during desorption process, images are taken after sample was heated up to (a) 300K, (b)550K, (c)700K and cool down to room temperature.

To find direct evidence of hydrogen bonding on the surface, HREELS is utilized to study the (CP) $Fe_3O_4$ (001) surface upon hydrogen adsorption. If hydroxyl (-OH) is formed, a signature vibrational mode of ~450 meV is expected. However, the OH vibrational mode is not observed in our HREELS measurement, as shown in Figure 3.5(b). Hydrogen adsorption performed at room temperature, 150K, and 100K (under verway transition) are all attempted in order to find the OH vibrational mode, but we did not find its signature. Specular and off specular measurements are also used, and still no OH vibrational mode around 450 meV was observed. To exclude individual sample factors, both natural and synthetic single crystals were used, and all the samples produced a sharp $\left(\sqrt{2}\times\sqrt{2}\right)R45°$ LEED pattern and the reported 50meV, 80meV vibrational modes from HREELS. In addition to using different samples, two HREELS systems are used to measure the hydrogen covered $Fe_3O_4$ surface. Both systems have been tested to work properly on other samples, and even with this level of care, no OH vibrational modes were observed. Since all the available methods failed to finding the OH modes, we conclude that

no measurable amount of hydroxyl (OH) exist on the $Fe_3O_4$ surface after hydrogen adsorption, contrary to expected results.

Although HREELS experiments failed to find the OH vibrational mode, it shows changes of the iron oxygen bonding vibrational mode. As shown in the Figure 3.5(a), on a clean $Fe_3O_4$ (001) surface, two peaks on 50 meV and 80 meV are observed, which agree with previously reported HREELS experiments.[75] After 300L hydrogen exposure, the 80 meV peak shifts to lower energy and both peaks become broader. The change in peak shape may be caused by the surface becoming rougher and less ordered after hydrogen adsorption, a conclusion which is also indicated in LEED experiments. The energy change is then due to the bonding strength change after hydrogen adsorption. Continuing exposure of the sample to hydrogen makes the 80 meV peak shift slightly more before saturating. Shifting to lower energy usually implies that the bonding strength becomes weaker which reduces the vibration frequency.

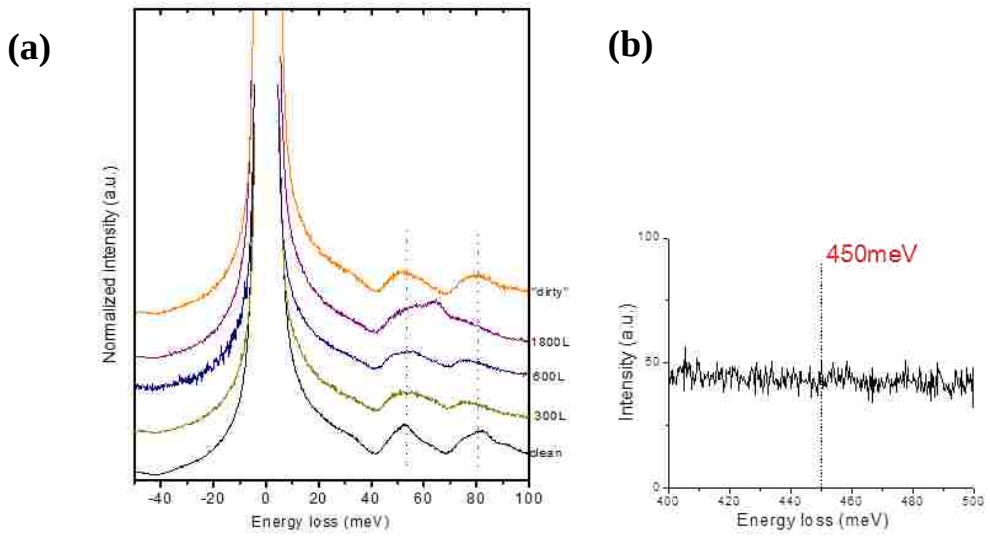


Figure 3.5 (a) HREELS of different hydrogen exposure on $Fe_3O_4$ surface, from bottom to top are clean(black), 300L(yellow), 600L(blue), 1800L(purple), "dirty"(orange) respectively. "dirty" surface was produced by leaving clean sample in low vacuum loadlock overnight. (b) HREELS of energy loss range around 450meV on hydrogen saturated surface. Primary electron energy is 7 eV, spectra measured at specular direction.

To make sure this change comes from hydrogen adsorption but not residue gases, a control experiment was also performed. A clean $Fe_3O_4$ sample is left in the "low" vacuum load lock (~$1\times10^{-6}$ Torr) overnight, with the hot tungsten filament in front of the sample surface. Then, the sample is transferred back to the HREELS analysis chamber and measured. The two peaks are lower and less sharp, but the peak location remains at the same energy as the clean surface. So the peak shift observed for the 80 meV peak is confirmed to be caused by hydrogen adsorption. At this point, HREELS has demonstrated that the $Fe_3O_4$ surface has been changed upon hydrogen adsorption, and that no OH is formed on the surface.

If hydrogen is on the surface, but not bonded to surface oxygen, then it may bond to surface Fe. Previous hydrogen adsorption on iron single crystal experiments have reported hydrogen will bond on the Fe bridge site and produce a vibrational mode around 110 meV.[76] Unfortunately, on the $Fe_3O_4$ surface, the range around 110 meV overlaps with the first overtone of the 50 meV peak. In this case, Fourier transform deconvolution method can be used to remove the overtones. As shown in Figure 3.6, after FTD, a small peak at 110 meV appears. This indicates that hydrogen bonds to surface Fe instead of oxygen.

In summary, HREELS experiments demonstrate that O-H bonding is not the preferential bonding on the hydrogen covered surface, which is an unexpected result. The influence of hydrogen adsorption is found through the shifting of the 80 meV vibrational mode peak. Therefore, atomic hydrogen does interact with the $Fe_3O_4$ surface, which is also the result of our previous LEED studies. According to Parkinson's STM study, hydrogen remains on the surface, so hydrogen may bond to surface Fe instead. This prediction is confirmed when the H-Fe vibration peak is found at ~110 meV after FTD. The 110 meV peak is, however, not strong and clear here, and further study of H-Fe bonding is required.

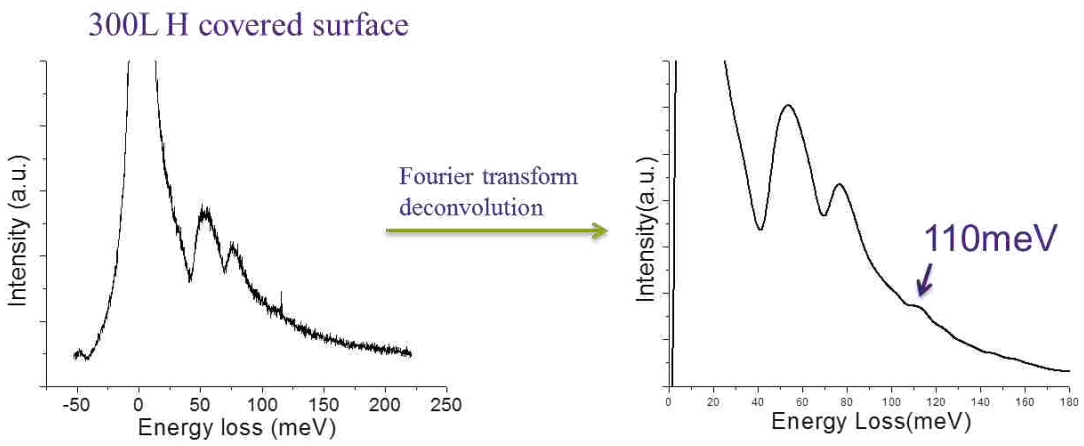


Figure 3.6 HREELS spectra before and after Fourier transform deconvolution. A small peak is revealed after FTD, as indicated with an arrow.

### 3.3 Low Energy Ion Scattering Spectroscopy (LEIS)

HREELS experiments show signs of H-Fe bonding upon hydrogen adsorption. If this is what happens on the surface, other surface techniques should also give the same results. LEIS is a surface measurement technique, which sees only the topmost layer. Although hydrogen cannot be directly observed through LEIS, the shadowing effect could make hydrogen atoms "visible" and provide the adsorption site.

As shown in the Figure 3.7, the black curve is the spectra for a clean (CP) $Fe_3O_4$ surface, while the red is for hydrogen saturation. According to the two body collision equation eq(1), the peak at ~1280 eV is due to Fe, and the peak on the lower energy side ~960 eV is from oxygen. Since there are many other interactions on the surface during scattering processes other than simple elastic scattering, the peak locations are usually shifted with respect to theory. After hydrogen adsorption, the Fe peak is significantly reduced, while the oxygen peak is only lowered slightly. This observation illustrates that surface Fe atoms are affected more than oxygen atoms by the shadowing effect. Therefore, adsorbed hydrogen atoms are closer to Fe atoms, implying hydrogen wants to bond to Fe. This result agrees with HREELS experiments.

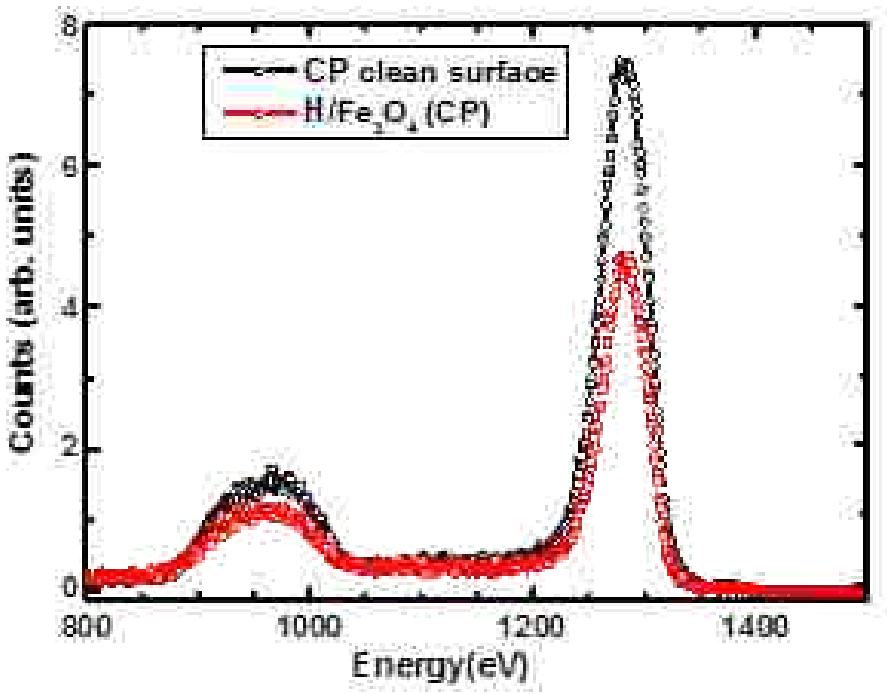


Figure 3.7 LEIS of clean (black) and hydrogen saturated (red) $Fe_3O_4$ (001) surface. Incident He+ beam energy is 1500eV, angle between ion source and analyzer is 100 degrees. O peak located at ~960eV and Fe peak at ~1280eV.

The exact scattered ion yield can be quantitatively analyzed. The two spectra are first normalized, and then the background is subtracted to determine the net peak area. As shown in the Figure 3.8, the highlighted regions are defined as the peak region. The peak area is calculated by CasaXPS software. On the clean surface, the oxygen peak area is 499 while the Fe peak area is 1213. The oxygen to Fe peak ratio agrees with previous studies on clean $Fe_3O_4$ surface.[37] After hydrogen adsorption, the oxygen peak area reduces to 366 and Fe peak area becomes 730. This is a 25% area loss for oxygen and 40% for Fe.

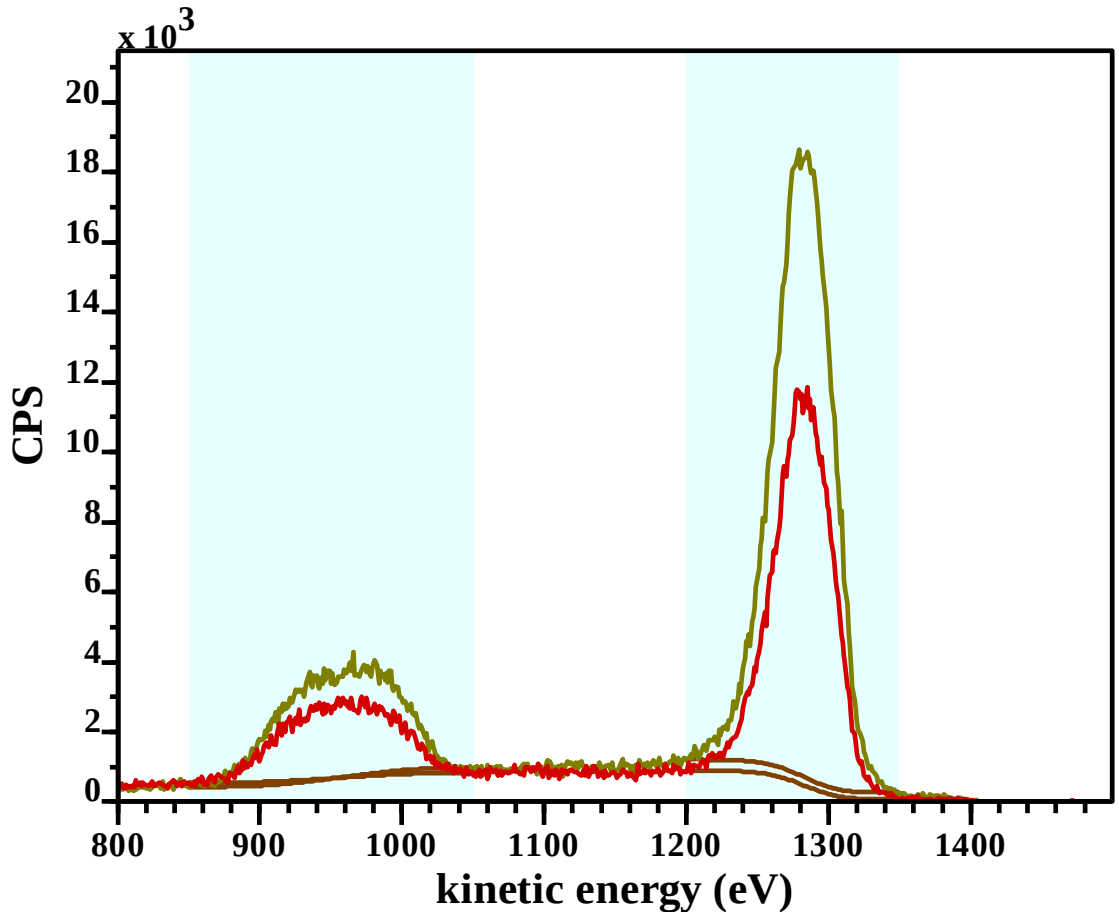


Figure 3.8 Quantitative analysis using CasaXPS to measure the peak areas before(brown) and after(red) hydrogen adsorption.

The sample holder in our system cannot rotate, which means the incident ion beam is only scattered by a specific sample azimuthal angle. When the sample is mounted to the plate, the orientation of the plane is unknown, meaning that each LEIS measurement could have different azimuthal angles. This makes the LEIS results have an error due to the orientation. That is why, when the experiment is repeated, the peak area changes have slightly different values. For example, the oxygen could reduce only 23% instead of 25%. But qualitatively, the Fe peak area always reduces more than the oxygen peak.

Similar to LEED measurements, the hydrogen covered $Fe_3O_4$ sample is measured as a function of temperature as well. As shown in Figure 3.9, after heating to 500K, the Fe peak

intensity is recovered for a clean surface. This means that the shadowing effect produced by hydrogen is totally removed when H is removed. Therefore, we can conclude hydrogen is desorbed at this temperature. This is as expected according to the previously reported hydrogen desorption temperature. The most interesting phenomenon is, at this temperature, the oxygen peak has not recovered, which is consistent with the fact that the LEED pattern does not fully recover at this temperature.

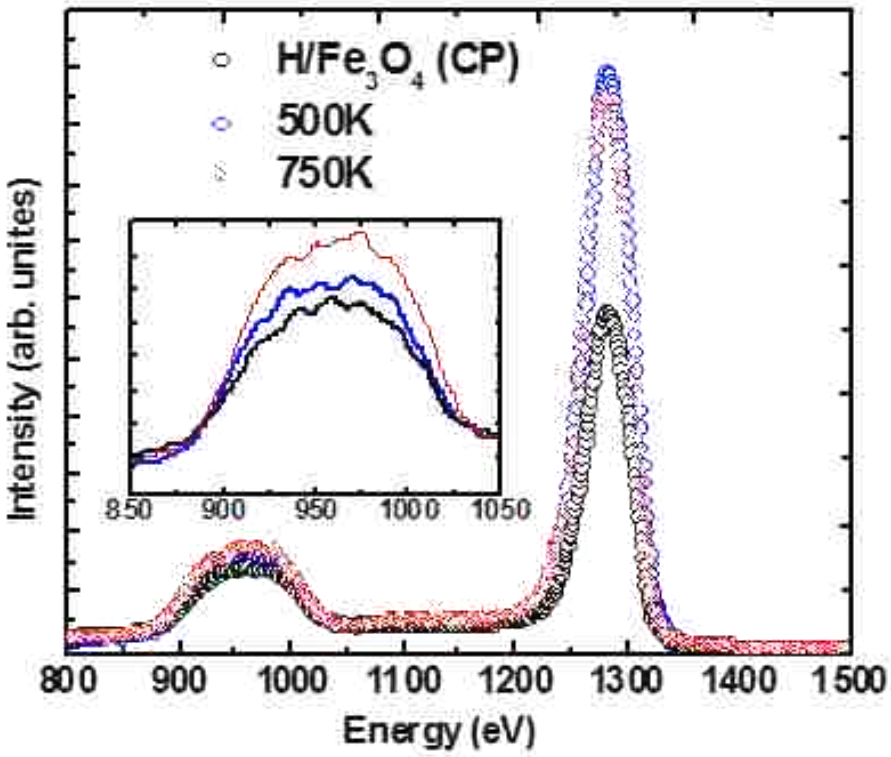


Figure 3.9 Desorption process measurements with LEIS. H covered surface spetra(black) is compared with surfaces heated to 550K(blue) and 750K(red).

If we raise the temperature to 750K, the oxygen peak totally recovers to the intensity of the clean surface. This temperature is same with the temperature when the LEED pattern was seen to recover. From this we can say that there are at least two steps in the desorption process. First, at ~500K, adsorbed hydrogen on Fe sites desorbs, removing shadowing of Fe atoms. Since the LEIS oxygen peak intensity does not change with warming to 500K, one can speculate the

surface oxygen concentration hasn't changed during the desorption process. Thus, hydrogen desorbs in the form of $H_2$, not water. Our sample was kept at 500K for long time, yet the oxygen peak never recovered. When the sample is heated up to 750K, both the LEED pattern and oxygen peak intensity are recovered. These processes are then completely reversible. The reason oxygen peak needs higher temperature to recover may cause by the stronger bonding strength of O-H bonding. Although hydroxyl is not observed by HREELS, there may still small amount of OH species on the surface, which leads to the shadowing effect of O peak in LEIS. Thus when temperature is high enough to break O-H bonding, the shadowing effect is released and the O peak recovered.

In conclusion, our LEIS experiments confirmed HREELS's result that hydrogen preferentially bonds to surface Fe and not oxygen. More importantly, by investigating the desorption process, LEIS revealed two steps are included. Hydrogen of H-Fe bonding first desorbs at 550K, then at 750K, O-H bonding also broken and oxygen peak recovered to its original intensity. All results of LEED, HREELS and LEIS have been consistent with the adsorption structure of hydrogen on the $Fe_3O_4$ surface described.

### 3.4 XPS and UPS

We have discovered evidence of hydrogen preferentially bonding to surface Fe instead of oxygen structurally. With XPS and UPS, the electronic properties can be studied. Figure 3.10 is a wide range scan on clean $Fe_3O_4$ (001) at room temperature. Fe and oxygen peaks are marked in the figure. No carbon peak is observed, which means that the surface is clean. It is worth noticing that the Fe 2p peak is split into 2p ½ and 2p 3/2 peaks because of spin orbital coupling, with an area ratio of 1:2 in principle.

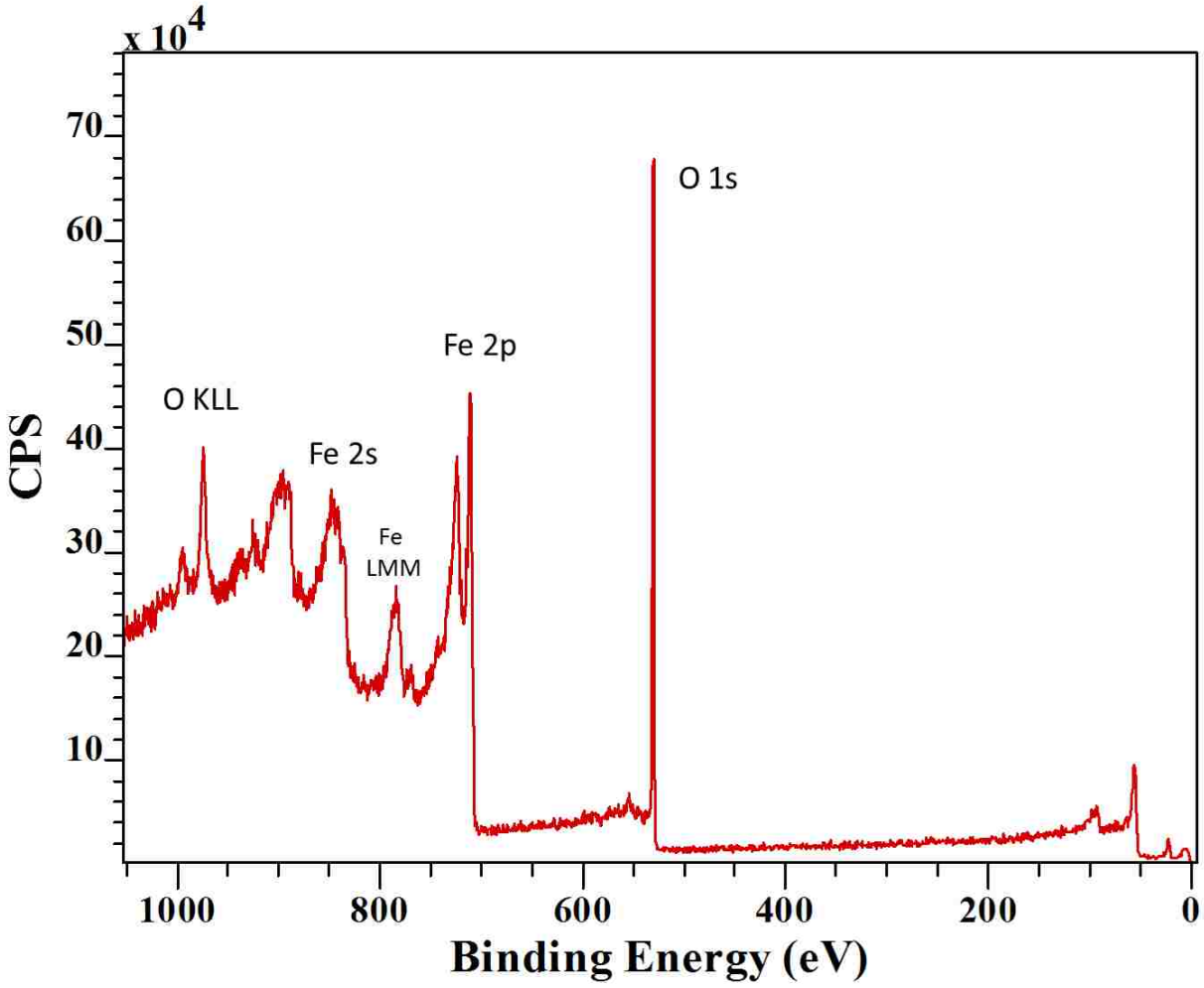


Figure 3.10 A full scan of XPS on clean $Fe_3O_4$ (001). The main peaks are labeled.

XPS is used to measure work functions. The secondary electron cut off edge is very sharp and has high intensity. To determine the cut off energy point for the spectra, two linear fits can be used as shown in the Figure 3.11. First the slope is fit where the intensity is straight up, then subsequently fit for where the intensity is nearly zero. The cut off energy is the cross point of these two lines. After getting the two energies, the work function can then be calculated with *eq(9)*.

**(a)**

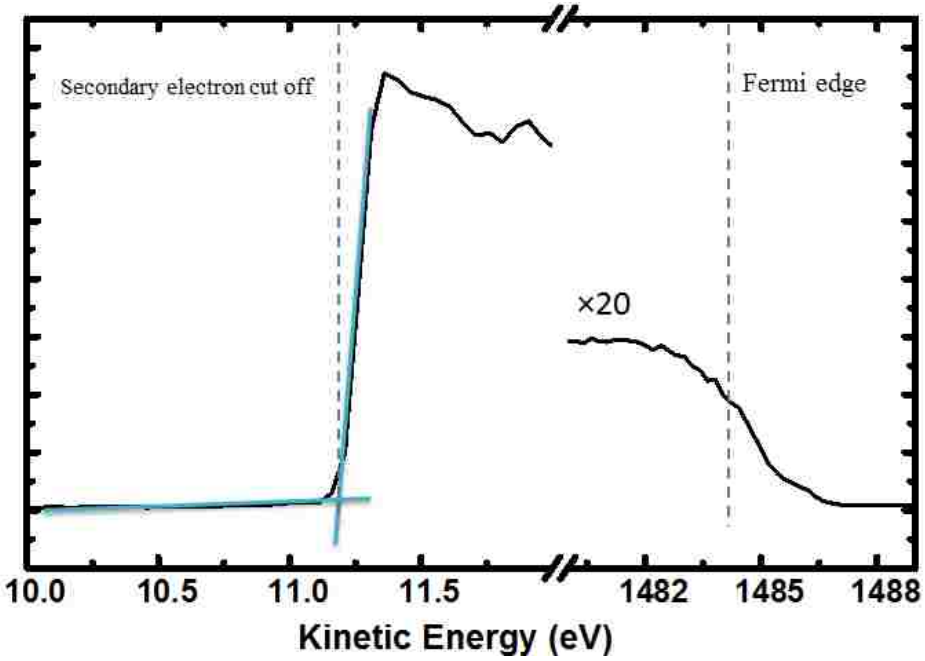


**(b)**

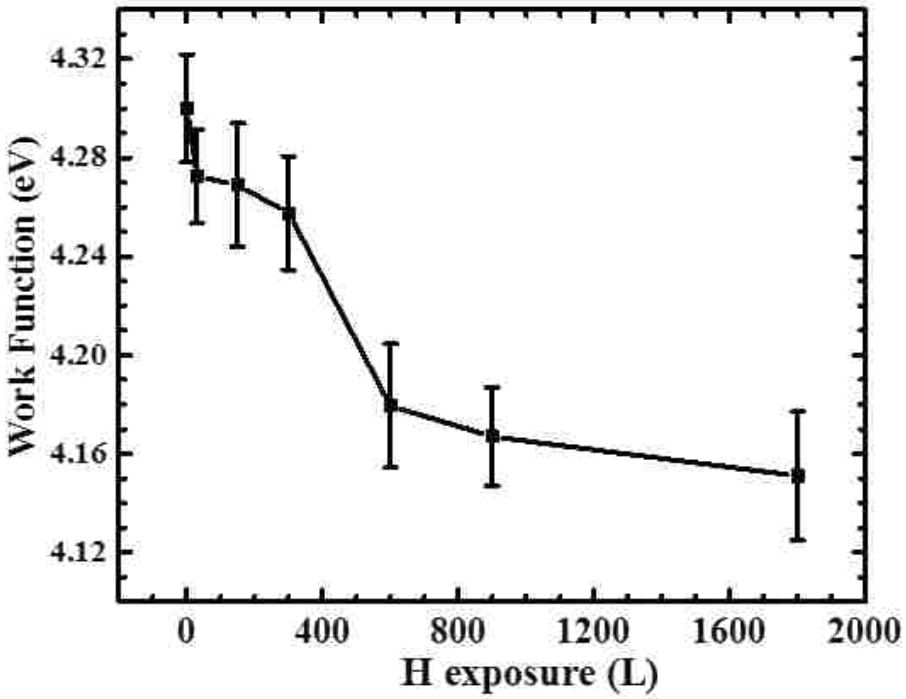


Figure 3.11 (a) secondary electron cutoff measured by XPS. Sample is biased 6 volts, curve is fit with two lines and the cut off energy is circled; (b) Work function change upon hydrogen exposure, clean surface work function (4.3 eV) is referenced as 0.

The work function on a clean CP $Fe_3O_4$ surface is 4.3 eV. Using the clean surface work function as a zero point, the work function's change after hydrogen exposure is plotted in Figure 3.11(b). Hydrogen adsorption makes the surface work function decrease, reaching saturation around 1000L H exposure. Taking a close look at the shape of the curve, it is found that the drop in work function has two regions. After dosing only 50L hydrogen on the surface, the work function has a dramatic drop to -0.10 eV. The work function drops to -0.20 eV after 600L of total hydrogen exposure. After that, the work function decrease becomes slower and more stable. This indicates that there are two different bonding sites with two different sticking coefficients.

The Fe 2p peaks can provide information on the Fe valence states on the surface. Figure 3.12(a) is the Fe 2p peak measured on $Fe_3O_4$, $\alpha$-$Fe_2O_3$ and $\gamma$-$Fe_2O_3$ surfaces. The $Fe^{3+}$ and $Fe^{2+}$ $2p^{3/2}$ are indicated with dashed lines. The binding energy of $Fe^{3+}$ is 711.1 eV while the $Fe^{2+}$ is 709.7 eV.[77] The shake-up satellite peaks in iron oxide are usually located 6-8 eV higher than the binding energy of the main peaks. The satellite peak of $Fe_3O_4$ is much weaker than the satellite peak in $Fe_2O_3$ at 719 eV.

Figure 3.12(b) is the Fe 2p spectrum measured in our system. The peak shape agrees with previous results for the $Fe_3O_4$ (001) surface given in Figure 3.12(a). The $Fe^{3+}$ and $Fe^{2+}$ 2p and satellite peaks are labeled. After hydrogen adsorption, the lower binding energy shoulder of the Fe 2p ½ peak is clearly increased, which indicates that the amount of surface $Fe^{2+}$ has increased after hydrogen adsorption. This is as expected since hydrogen brings an extra electron to the system. Whether or not hydrogen bonds to oxygen and forms OH or bonds to surface Fe and directly forms H-Fe bonding, $Fe^{3+}$ will be reduced to $Fe^{2+}$ in both cases. So this observation cannot be used to determine where hydrogen bonds, but only confirms that hydrogen reduces the surface.

**(a)**

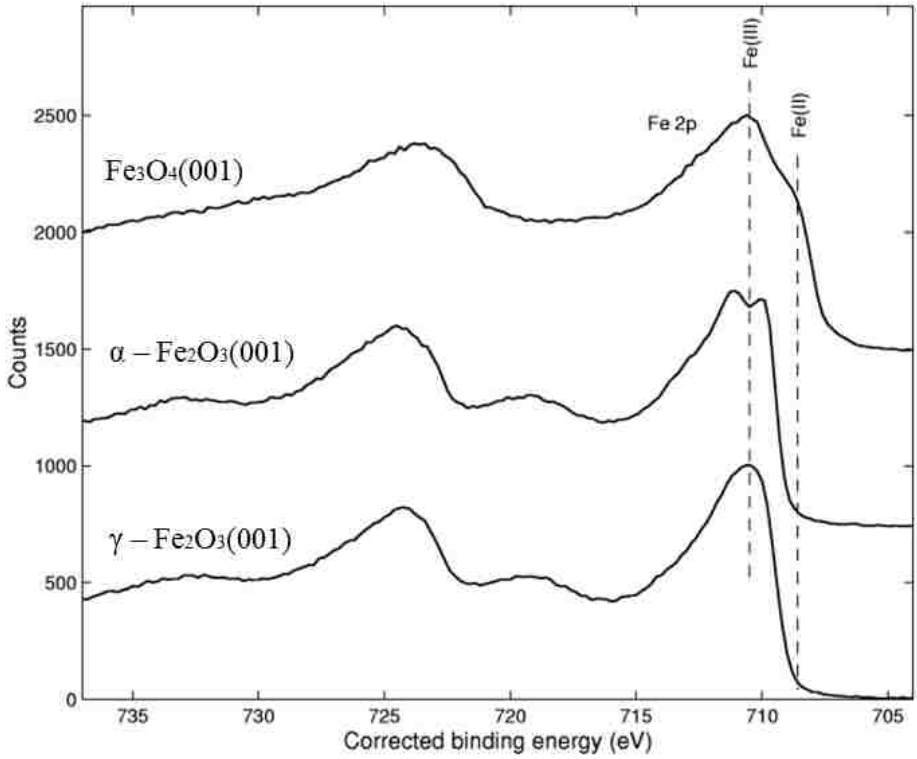


**(b)**

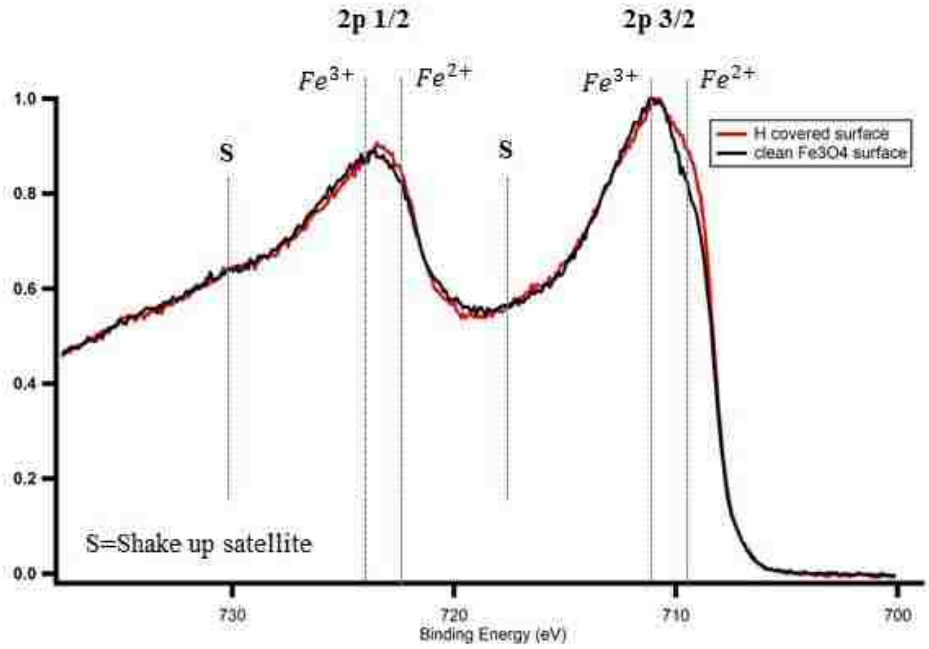


Figure 3.12 XPS spectra on $Fe_3O_4$ surface upon hydrogen adsorption. (a) Fe 2p ½ and Fe 2p $^{3/2}$ peaks. Figure adapted from[77] (b) O 1s peak before(black) and after hydrogen adsorption(red)

Quantitative analyses of Fe 2p peaks are not practical since the peak is complex. As previously reported for the iron oxide surface, shake-up effect, multiplet splitting, and phonon broadening are included in the Fe 2p peak, which makes it too complicated for peak fitting.[35,66] During shake-up processes, outgoing photoelectrons can excite a valence electron to higher energy empty states, thus reducing the kinetic energy of photoelectron and creating a higher binding energy peak with respect to the main peak. For example, the shake-up satellite peak of $Fe^{2+}$ $2p^{3/2}$ is located at 714.5 eV, which is in the region of the broad Fe $2p^{3/2}$ peak. Multiplet splitting happens when there are unpaired electrons in the valence band. When a core electron is excited and leaves an unpaired electron in the core level, this unpaired electron will couple with the outer shell unpaired electrons. This effect will create several final states and will be observed as multi-peak splitting. The $Fe^{3+}$ and $Fe^{2+}$ have 5 and 4 unpaired 3d electrons, respectively. Therefore, $Fe_3O_4$ has strong multiplet splitting effects. Phonon broadening describes the excitation of low energy vibrational modes in the initial and final states. Considering those effects for $Fe_3O_4$, the 2p peak is more complicated because of the existence of two iron oxidation states. Because of this reason, Fe 2p peak fitting is not attempted in this thesis work.

Figure 3.13 shows the oxygen 1s spectrum of InGaZnO thin film, where the O 1s peak is located at 530eV binding energy, as is reported for ionic oxygen.[77,78] O 1s can be used to study the oxygen environment on the surface. As shown in the spectrum, oxygen in water creates the 1s peak at 533 eV, while the 1s peak for OH is located at 532 eV.[79,80] If these OH or $H_2O$ species have large amount appear on the surface, the O 1s peak should become broadened and asymmetric.

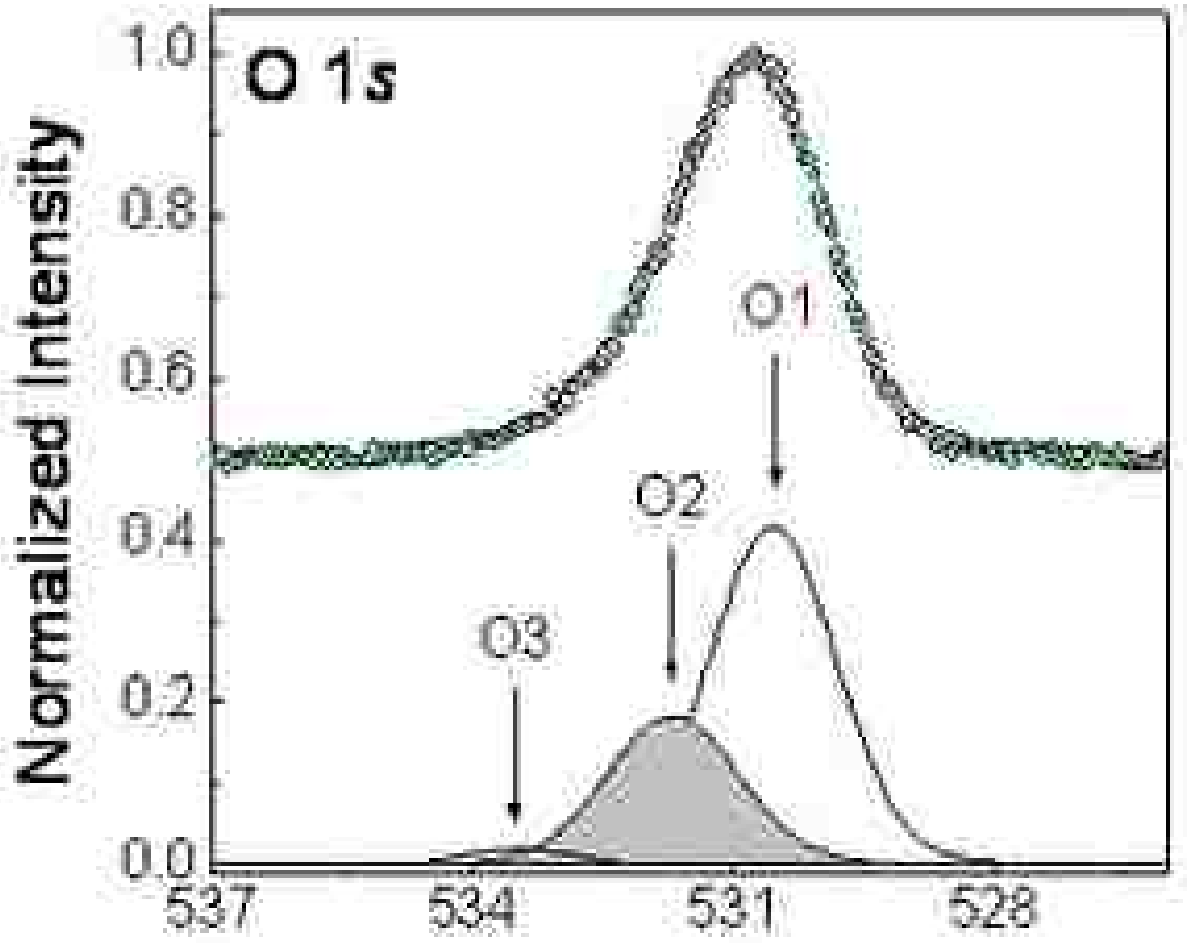


Figure 3.13 XPS O 1s spectrum of InGaZnO film. O1 is ionic oxygen ions, O2 is oxygen deficient $O^{2-}$ ions or OH species, O3 is oxygen in $H_2O$ or $O_2$ molecules. Figure adapted from [81].

When we return to the question of where hydrogen binds on the $Fe_3O_4$ surface, one would expect a shoulder at 532 eV to appear if hydrogen bonds to surface oxygen. The O 1s spectra before and after hydrogen adsorption on the $Fe_3O_4$ surface is displayed in Figure 3.14. No OH features at 532 eV was observed after hydrogen adsorption. The curves before (black) and after (red) hydrogen adsorption nearly overlap at the ~532 eV binding energy region. However, the peak intensity is clearly lowered after hydrogen adsorption.

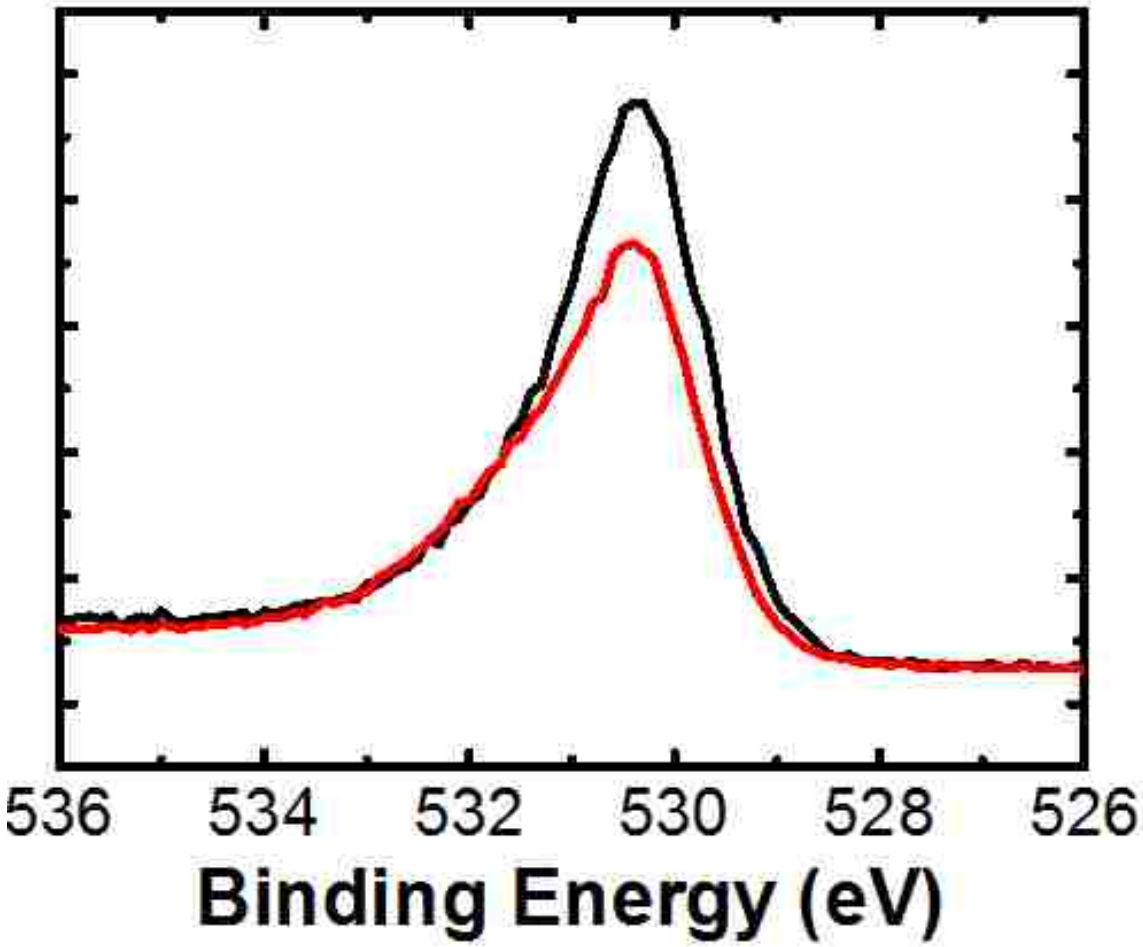


Figure 3.14 XPS O 1s spectra measured at 81° emission angle on CP $Fe_3O_4$ surface before (black) and after (red) hydrogen adsorption.

Although XPS is a surface sensitive technique, it is not as surface sensitive as HREELS and LEIS, as multiple layers can contribute to the signal yield due to the mean free path. Depending on the experimental condition, the photoelectrons can escape from as deep as up to 10 nm under the surface. Thus, when better surface sensitivity is required, high angle detection is typically used. As we discussed in chapter 2, only 2 layers of magnetite will contribute to the electron yield when the emission angle is more than 80 degree.

As shown in Figure 3.15(a), the red O 1s spectrum is taken at an 81° emission angle. The intensity is much lower than the spectra taken at normal angle at only ~2.5% of the original. Since the oxygen peak has a high intensity, only a few scans are required to get a good spectrum even at high emission angle. For those low intensity peaks, such as Fe 2p, up to 50 scans can be needed to obtain a usable spectrum, and this can take several hours. If the peak is already noisy at normal angles, as is the case for Fe 3d, it may not be able to do high angle emission experimentation. According to *equation (7)*, at a 81° emission angle, about 96% signal comes from top two layers (~2.1Å per layer) of $Fe_3O_4$, among which the topmost layer contributes about 80% and second layer contributes 16%. This technique is then much more surface sensitive than normal emission XPS (~15 layers).

Comparing the O 1s peak shape at the 81° emission angle with normal emission, it is seen that the peak for the 81° emission angle is much more asymmetric. As displayed in Figure 3.15(a), after normalizing and subtracting the background, the normal emission angle spectrum is asymmetric, but the 81° emission angle spectrum is even more asymmetric. The reason for this asymmetry in the O 1s peak of $Fe_3O_4$ is still debated. Chambers claim this could due to the shake-up effect.[37] In Chamber's ARXPS measurements on $Fe_3O_4$ thin films, the normal angle emission spectra have the same magnitude of asymmetry as high angle emission spectra. However, in our experiments, high angle emission 1s peaks were more asymmetric, which indicates that there are other factors besides the shake-up effect.

One possible alternative explanation is due to the oxygen vacancy on the surface. Goodenough states that the oxygen deficient region oxygen atoms will have higher O 1s binding energy and therefore induce the asymmetry.[82] However, shake-up and oxygen vacancy cause the same spectra structure, so it is hard to distinguish them. As shown in Figure 3.15(b), the O 1s

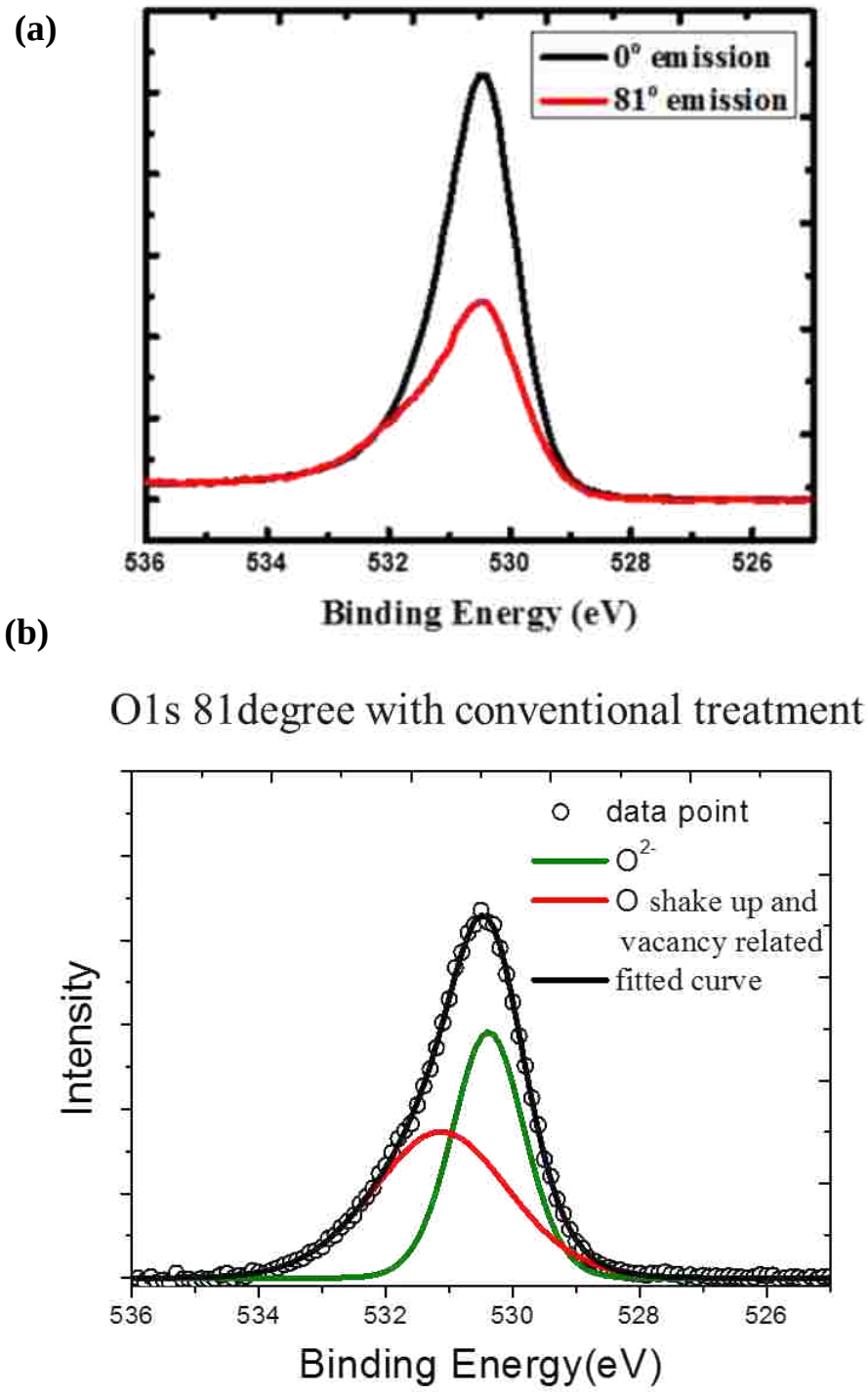


Figure 3.15 (a) Comparison of normal emission O 1s spectra (Black) with 81 degree emission spectra (red), spectra are normalized. (b) 81 degree emission angle of O 1s spectra fitted with ionic oxygen and shake-up, vacancy related oxygen components.

peak is fitted with two peaks, one ionic peak at ~530.0eV and another at ~532.0eV either due to the shake-up or oxygen deficient region effects. The peak area of the ionic peak is 74%, which means that 26% of the photoelectrons come from either the shake-up effect or oxygen deficient regions. The O 1s spectrum at normal emission is also fitted using the same parameters. The ionic peak ratio is 81%, while shake-up and oxygen deficient peak ratio is 19%. These results indicate there are large amount of oxygen vacancies on the clean $Fe_3O_4$ surface after annealing in oxygen.

Recall that we both followed the conventional surface preparation recipe to anneal the sample in an oxygen-rich environment and got a sharp LEED pattern as previous reported. The HREELS experiments also gave the same 50meV and 80meV vibrational mode peaks as previous results, confirming we has the same surface as other studies. However, our XPS experiments raise the question of whether the $Fe_3O_4$ surface after conventional preparation is a stoichiometric surface or not, in that there may be large amount of oxygen vacancies on the surface.

UPS focuses on the valence band near the Fermi energy. This region reflects more about the details in the bonding. Similar to XPS spectra, the two iron valence states have different energy level. As shown in Figure 3.16, the previous reported UPS data on iron oxide surfaces, both FeO and $Fe_3O_4$ UPS spectra show a peak at ~1 eV, while $Fe_2O_3$ does not have one. So this peak at ~1 eV could be a signal of $Fe^{2+}$. On the other hand, both $Fe_3O_4$ and $Fe_2O_3$ have a spectra weight at ~3 eV, while FeO does not. This feature at ~3 eV is then assigned as a signal of $Fe^{3+}$.[83]

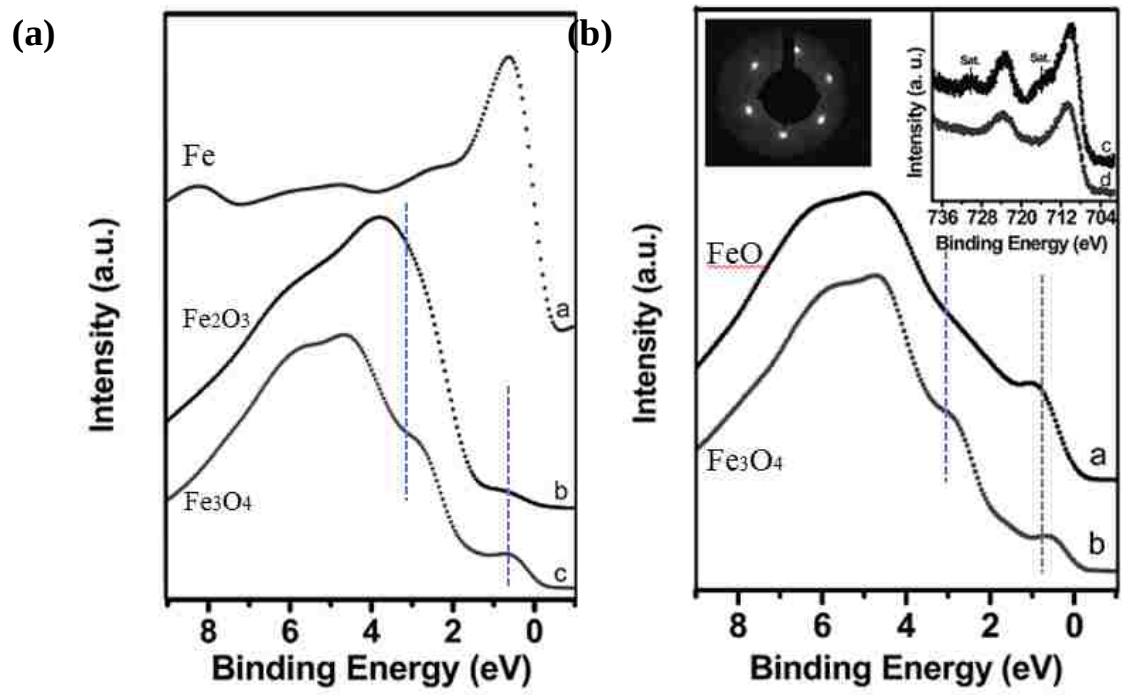


Figure 3.16 (a)UPS on Fe(110), Fe2O3(000a), and $Fe_3O_4$ (111) surface. (b) UPS on FeO and $Fe_3O_4$ films. Top left inset is LEED pattern of FeO(111), top right is XPS Fe 2p peak of these two films. Figure adapted from [83]

Our UPS results for the CP $Fe_3O_4$ surface is shown in Figure 3.17. As indicated by the black arrow, the $Fe^{2+}$ 3d peak is located at ~1 eV while the $Fe^{3+}$ is located at ~2.8 eV. The large peak at ~4 eV is another Fe 3d electron peak which appears in most iron oxide materials.[22,83,84] After hydrogen adsorption, the spectrum changes. The spectra weight of $Fe^{2+}$ increases from nearly zero to a slightly larger value, indicating that the amount of $Fe^{2+}$ has increased. However, the increase is much smaller than that seen in Parkinson's report.[38] In his paper, the Fermi level dramatically increased after hydrogen adsorption, which they interpret as a semiconductor to half metal transition. This striking change is not observed in our experiments, even after using two separate UPS systems.

**(a)**

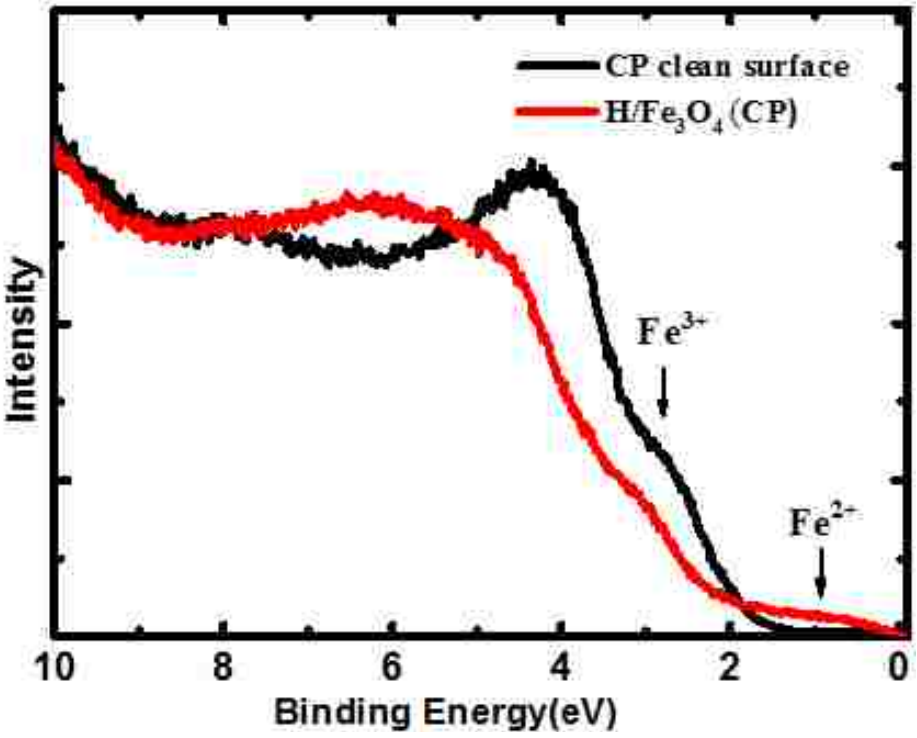


**(b)**

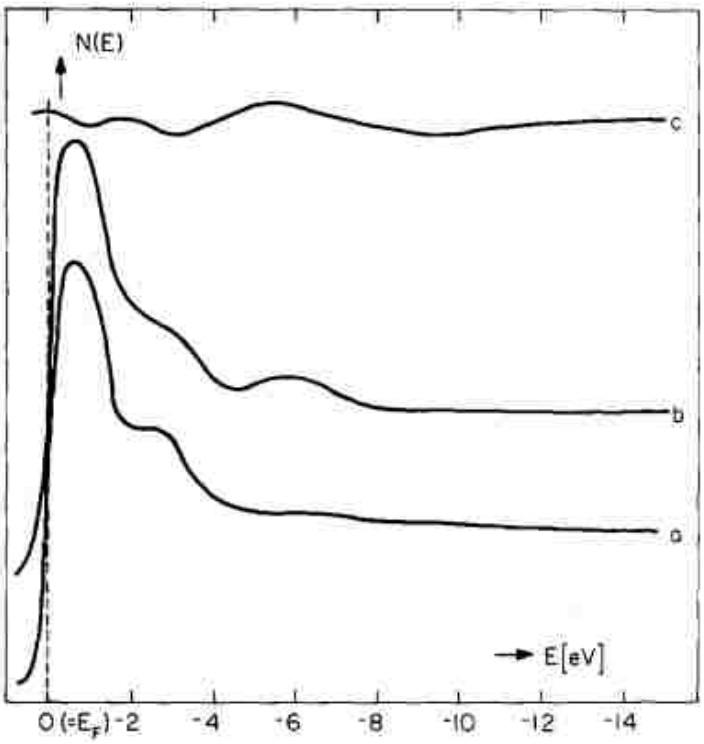


Figure 3.17 (a) UPS on $Fe_3O_4$ (001) surface before(black) and after hydrogen adsorption(red), spectra was taken at normal emission angle. (b) UPS from Fe(100), from bottom to top are: clean surface, hydrogen saturated, and difference spectrum. Figure adapted from [85]

The $Fe^{3+}$ shoulder dropped while the $Fe^{2+}$ increased after hydrogen adsorption, which is expected. The iron valence reduction in UPS is similar to the XPS experiment results upon hydrogen adsorption. One change however is the appearance of a large, wide peak at ~6 eV. This has not been seen on pure iron oxide materials. However, this peak has been reported for hydrogen adsorption on Fe metal surfaces. In Figure 3.17(b) curve b, a similar wide peak appears ~6 eV after hydrogen adsorption. The study attributed this to H-Fe bonding.[85] The similar peak shape and location indicates that they have the same bonding on the surface, which is to say that there is also H-Fe bonding on hydrogen covered $Fe_3O_4$ surfaces. The UPS experiments confirm the existence of H-Fe bonding upon hydrogen adsorption as previously found in our LEIS, HREELS and XPS experiments.

Desorption experiments were performed using XPS. Figure 3.18 shows three Fe 2p spectrum for after hydrogen adsorption, heated to 500K, and heated to 700K. The $Fe^{2+}$ peak was enhanced after hydrogen adsorption. After being heated to 500K, the $Fe^{2+}$ shoulder clearly drops, indicating that the amount of $Fe^{2+}$ is reduced. This is due to the desorption of hydrogen. Further oxidation is observed after heating the sample to 700K. As previous LEIS experiments indicated, there may be small amount of hydroxyl after hydrogen adsorption. Heating the sample to 700K will break the O-H bonding, which is why $Fe^{2+}$ continues to be oxidized to $Fe^{3+}$ at 700K.

In conclusion, XPS and UPS probed the electronic property changes after hydrogen adsorption. The O 1s peak from XPS and the wide peak at ~6 eV both confirm that hydrogen preferentially bonds to surface Fe and not O. It is shown by both techniques that hydrogen adsorption is a reduction reaction while desorption is an oxidization process, as expected. The two-step desorption process is consistent with previous experiments.

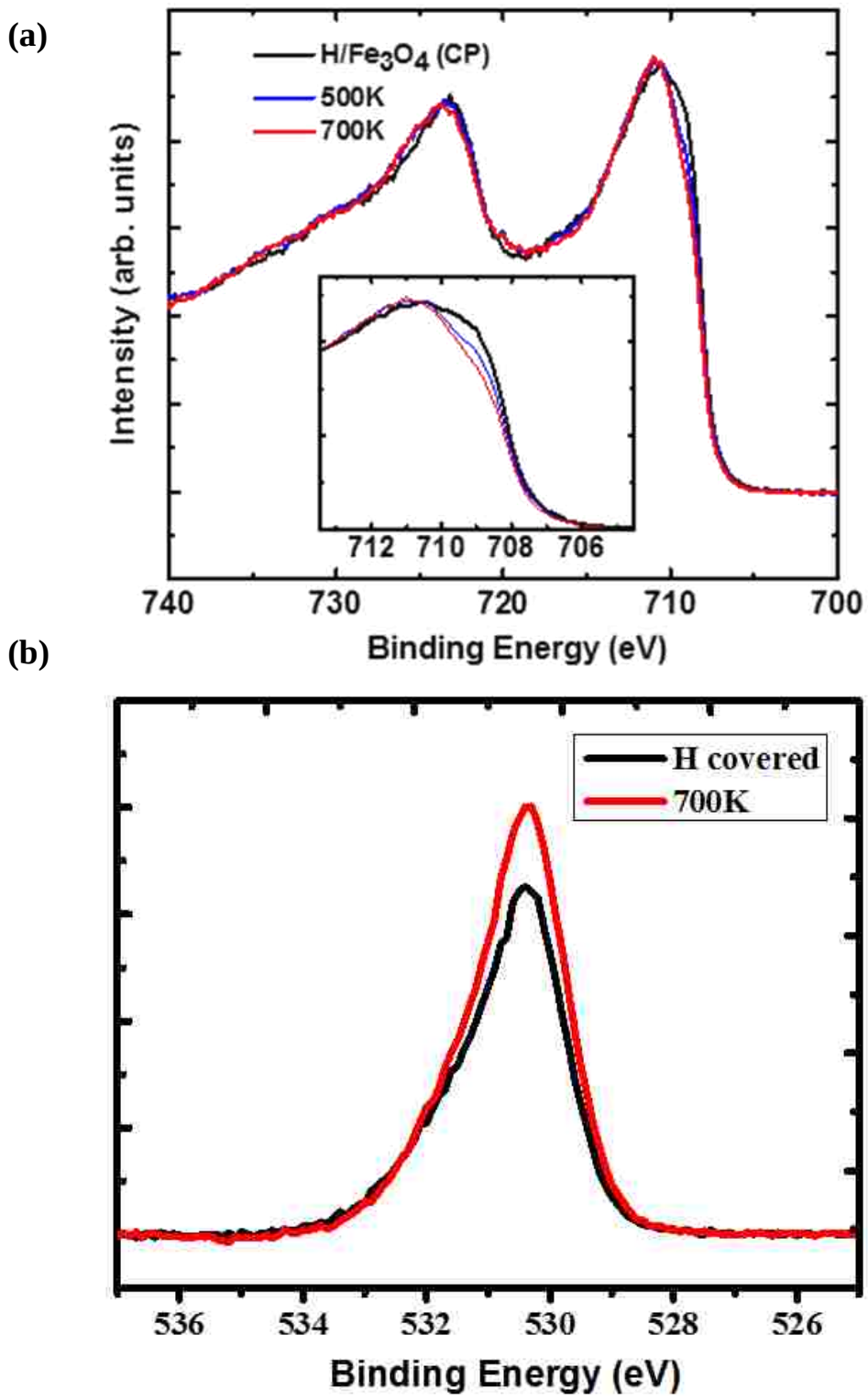


Figure 3.18 (a)Fe 2p peak during desorption process. Inset zoom in the Fe 2p ½ shoulder, shows the changes upon desorption temperature. (b) O 1s spectrum when desorption.

### 3.5 X-Ray Adsorption Near Edge Spectroscopy (XANES)

XANES is a core level absorption spectroscopy. It can provide insight into oxidation states, coordination, and bonding environments because it investigates the unoccupied electron states.

Iron L edge results from different samples are shown in Figure 3.19. The iron L edge is split into two main peaks because of spin-orbital coupling. $L_3$ is located in the ~710 eV region, induced by $2p^{3/2} \rightarrow 3d$ transitions. The $L_2$ peak is ~722 eV, induced by $2p^{1/2} \rightarrow 3d$ transitions. L peaks of iron oxides, such as $Fe_3O_4$ and $Fe_2O_3$, will further split into two subpeaks. This is due to the crystal field of these two oxides (octahedral or tetrahedral) splitting the 3d orbitals levels into $e_g$ and $t_{2g}$ orbitals. The $Fe^{3+}$ irons in $Fe_2O_3$ sit in octahedral sites, while the $Fe_3O_4$ case is more complicated. Half of $Fe^{3+}$ occupy octahedral sites and the other half in tetrahedral sites, while all the $Fe^{2+}$ occupy tetrahedral sites. Therefore, the $L_3$ edge of $Fe_2O_3$ is clearly split into two peaks while $Fe_3O_4$ only shows a small shoulder on the low photon energy side. Reference Figure 3.19 also compares the $L_3$ edges of FeO and $Fe_3O_4$. The Fe $L_3$ edge of FeO is located at ~707 eV, about 2 eV lower than main peak of $Fe_3O_4$. Since FeO has cubic structure, no double peak splitting was observed. Figure 3.19(c) shows how the L edge changes when an $Fe_3O_4$ sample is oxidized by exposing it to $O_3$ at room temperature. After ozone oxidation, the $L_3$ edge shoulder is suppressed. Therefore, with XANES, the crystal structure as well as the oxidation state of iron oxide can be analyzed.

Since the Varied Line Space Plane Grating Monochromator Beamline of CAMD has an energy range of 200-1200 eV, only the L edge could be measured at this beamline. Total electron yield is measured with this setup. The resolving power of this beamline is 5000. In this setup, the entrance slit size and exit slit size could be tuned to optimize the resolution and electron yield. A

slit size of 100um is the typical working parameter for high intensity and good energy resolution. However, as shown in Figure 3.20(a), the L3 peak is a broad peak without any detailed features as previous reported. In order to achieve better resolution, slit size is reduced at the expense of peak intensity. At 50 um, the best resolution is achieved for the $Fe_3O_4$ sample. A low energy shoulder and pre-peak bump is observed. However, when comparing to the previously reported L3 edge, our resolution is not as good here.

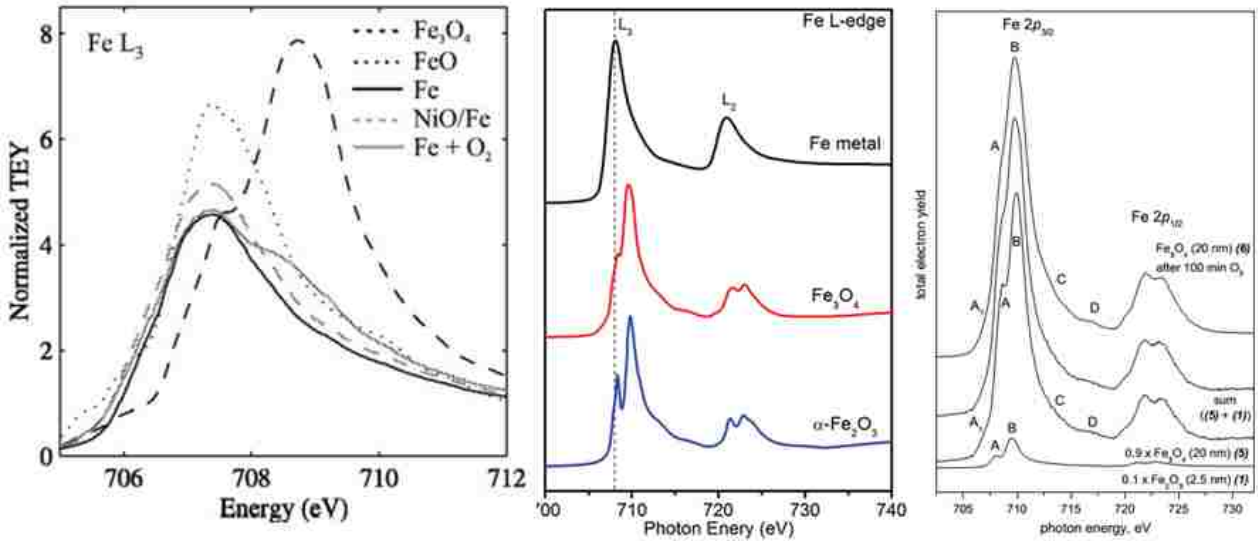


Figure 3.19 XANES Fe L edge of different iron based materials. Figures adapted from [86-88]

After hydrogen adsorption, the Fe $L_3$ edge shifts to the left side. Since the shoulder feature is hard to observe, it cannot provide much useful information in this case. The peak shape remains nearly the same after hydrogen adsorption, indicating that the sample structure does not change. Considering that lower edge energy usually means a lower oxidation state, for example the $Fe^{2+}$ L edge in FeO is 2 eV lower than $Fe^{3+}$ L edge in $Fe_2O_3$, shifting to lower energy may indicate a surface reduction upon hydrogen adsorption.

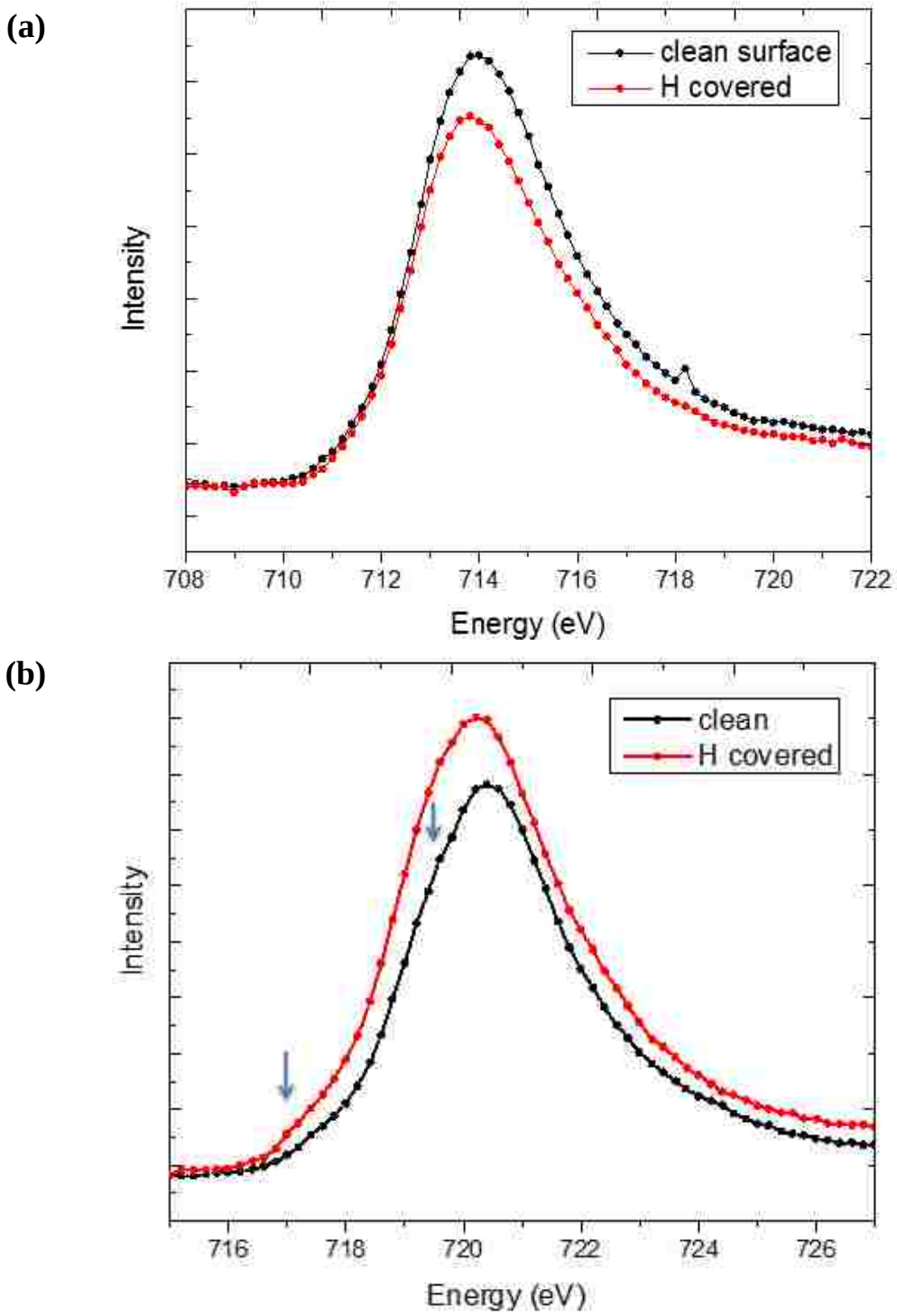


Figure 3.20 Fe L edge of $Fe_3O_4$ surface with(red) and without H covered(black). (a) Slit size is 100um. (b) slit size is 50um. More features are observed at smaller slit size, indicated by blue arrow in (b).

The oxygen K edge is also measured by XANES. As shown in Figure 3.21, no significant change was observed after hydrogen adsorption. The first peak is assigned to the excitation of O 1s electrons to the Fe 3d energy level, while the higher energy peaks are assigned to O 1s electrons performing Fe 4s and 4p transitions. The electron configuration for $Fe^{3+}$ is $3d^5$ and $Fe^{2+}$ is $3d^6$, showing that their differences are in the 3d band. So if there are differences, they should occur in the first peak. However, no change in the first peak is observed, which may be due to the low beam current when this set data was collected. As you can see from the data, the spectrum is noisy and has poor resolution. But the nearly perfect overlap of first peak could also suggest that the $Fe^{3+}$ to $Fe^{2+}$ change upon hydrogen adsorption does not have a large effect on the O k edge.

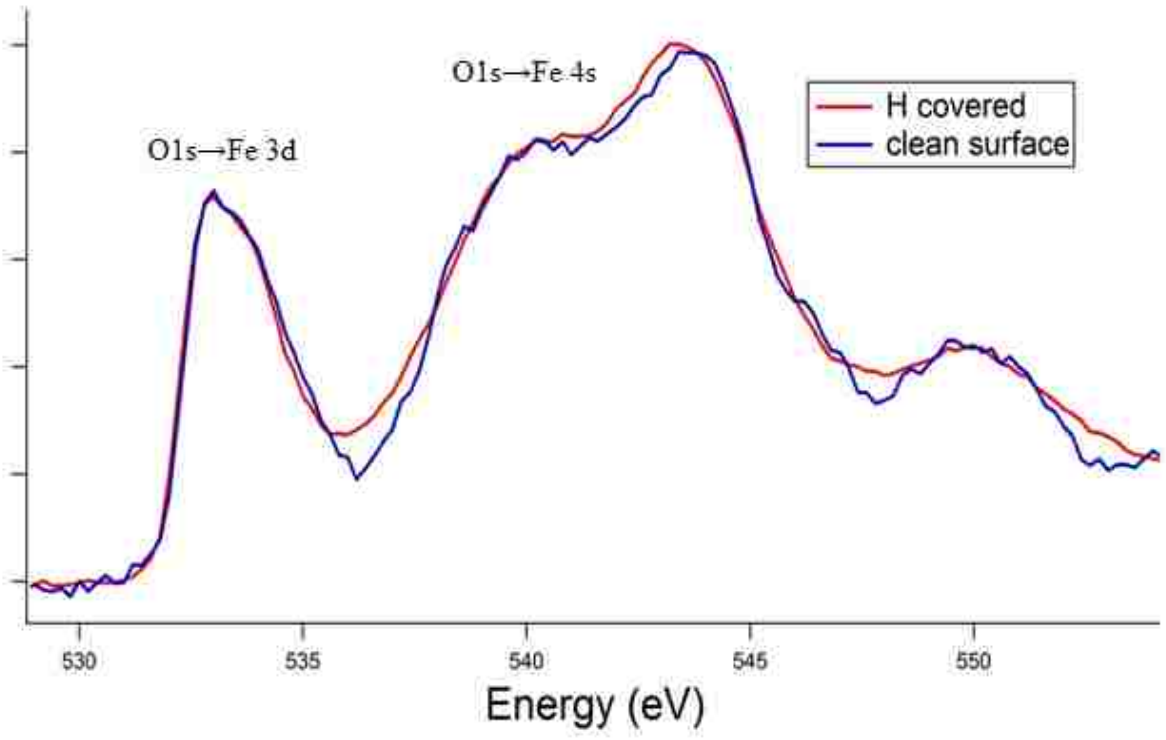


Figure 3.21 O K edge measured by XANES at normal incident angle.

Desorption experiments are also performed with XANES, both on the Fe L and O k edges. The shift and peak shape change on the Fe L edge after hydrogen adsorption are recovered after heating the sample up to about 500K, which means the changes observed are caused by hydrogen. Continued heating of the sample up to 800K does not bring about any more changes to the spectra. Another cycle of hydrogen adsorption is done on this same sample to confirm this change is reproducible and the results are consistent. Due to the lack of an accurate thermal couple, detailed investigations on the desorption process are not available for XANES.

In summary, although Fe $L_3$ edge splitting is observed, the resolution is not good, which makes more detailed investigation difficult. After hydrogen adsorption, the Fe $L_3$ edge is observed to shift towards lower energy, implying a surface reduction due to bonded H. O K edge doesn't show changes upon hydrogen adsorption.

**3.6 Summary**

Combining LEED, HREELS, LEIS, XPS, UPS and XANES techniques, hydrogen adsorption on the $Fe_3O_4$ (001) surface is studied structurally and electronically. Unexpectedly, all the techniques in our study suggested that large amount of hydroxyl species do not exist on hydrogen covered $Fe_3O_4$ surface. HREELS fails to discover OH vibration peaks around the anticipated 450 meV, XPS O 1s do not show a high binding energy peak around 532 eV, and LEIS oxygen peak areas do not significantly change upon hydrogen adsorption, all of which should be observed for OH formation phenomenon. Conversely, there is evidence for H-Fe bonding. LEIS observed a 40% peak area drop on the Fe peak, HREELS experiments found a small peak located at the H-Fe bridge site vibration frequency region, and a peak at 6 eV is observed in UPS which is consistent with H bonded to metal iron surfaces. All these observations suggest that hydrogen preferentially bonds to surface iron instead of oxygen.

Pan has reported that hydrogen bonds to surface Ti instead of O on oxygen deficient TiO2 surfaces.[89] Their LEIS spectrum is very similar to what we observed on our $Fe_3O_4$ surface. As shown in Figure 3.22, after hydrogen adsorption, their Ti peak was weakened dramatically while no change to the O peak was observed. They attribute this phenomenon to the high concentration of surface oxygen vacancies. This is important for our investigation. The existence of oxygen vacancy on the metal oxide surface is very common and will have large effects on the surface properties.

XPS O 1s spectra contain information on the oxygen vacancies of surfaces. Surface oxygen vacancies will create spectra weight at higher binding energies and make peaks asymmetric. This is what we have observed on our XPS O 1s spectrum. The high emission angle (more surface sensitive) spectrum is more asymmetric than the normal emission (more bulk sensitive) spectrum, indicating that the surface may contain oxygen vacancies. But the determination of surface oxygen vacancy concentration is difficult, especially for well-ordered vacancies.

Desorption experiments are done with LEED, XPS and LEIS. LEIS shows a two-step desorption process. After heating to 500K, the Fe peak is recovered while oxygen peaks remain the same, but by continuing to heat the sample to 750K, the oxygen peaks recover as well. LEED patterns are not recovered until 750K and are therefore affected by a two-step process. XPS Fe 2p peak also portrays a two-step desorption process; after heating to 550K, the $Fe^{2+}$ shoulder is clearly reduced and close to the clean surface spectrum. However, after heating to 750K, the Fe 2p peak is completely recovered. The oxygen peak area from LEIS did not reduce during desorption processes, showing that hydrogen desorbed as pure hydrogen. Therefore, the change was made during the adsorption process.

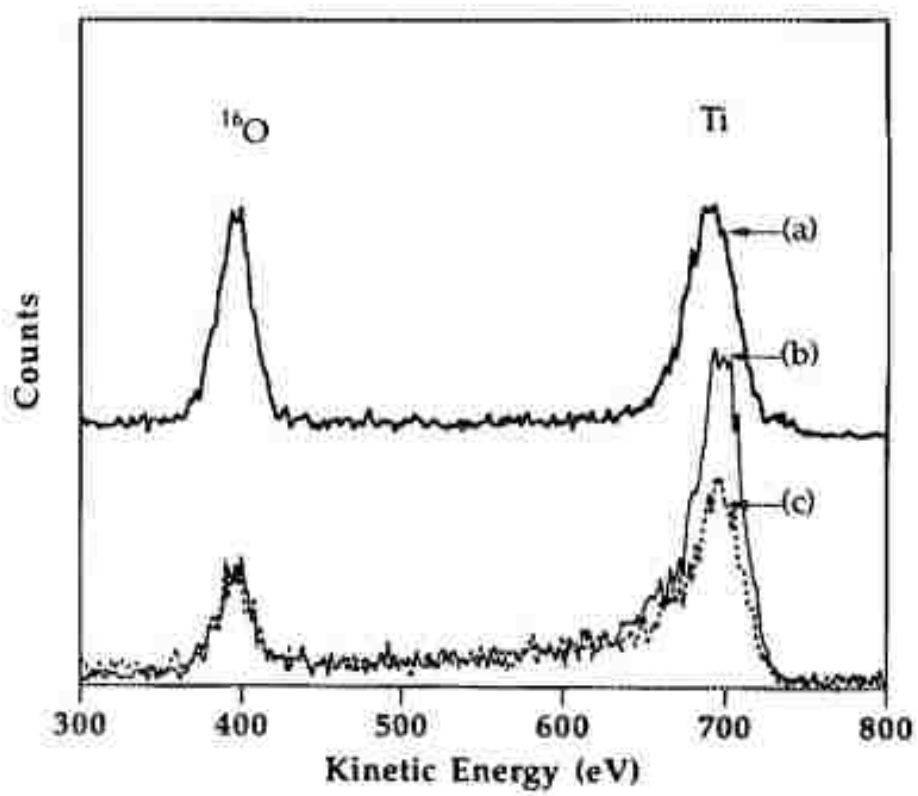


Figure 3.22 LEIS spectra of (a) clean stoichiometric, (b)clean highly defective (sputtered) $TiO_2$ (110) surfaces, and (c)highly defective surface after 50eV hydrogen ion exposure. There is an increase of Ti intensity and a decrease of O intensity for the sputtered surface (b) comparing with (a), and a pronounced reduction of Ti intensity for spectrum (c) after hydrogen exposure.

In summary, hydrogen adsorption on the $Fe_3O_4$ (001) surface is studied with multiple techniques. H-Fe bonding instead of H-O bonding is confirmed with these measurements. XPS experiments indicate that there are still oxygen vacancies on the surface after conventional treatment, and this could be related to the unusual H-Fe bonding. A reasonable hydrogen adsorption is proposed based on the experimental results.

# CHAPTER 4 H ADSORPTION ON OZONE PROCESSED (OP) $Fe_3O_4$ SURFACE

## 4.1 Surface Preparation and LEED Measurements

It has been suggested from previous experiments that conventional processing (CP) cannot effectively remove surface oxygen vacancies and these vacancies may play an important role in hydrogen adsorption. Due to the inability to identify the concentration of surface oxygen vacancies, an alternative approach has been used. Because simple annealing in oxygen is not enough to get rid of oxygen vacancies, a more reactive oxidant is required. Ozone is frequently used as an oxidant in oxide thin film growth because thin films require a better oxidant due to their inherent lack of bulk states to serve as oxygen reservoirs, necessitating that oxygen be provided externally instead.

After regular sputtering, $Fe_3O_4$ (001) was annealed in a 6% ozone oxygen environment to 700K in a different UHV chamber, and then transferred *in-situ* to the analysis chamber. LEED patterns show a $(\sqrt{2} \times \sqrt{2})R45°$ reconstruction but with larger background than the CP surface. This may be caused by some residue molecules physically adsorbed by the surface. The sample was then flashed to 500K for 30 seconds before measuring the LEED pattern again. A sharp $(\sqrt{2} \times \sqrt{2})R45°$ reconstruction with low background is observed.

LEED is shown in Figure 4.1, where the top panel is the conventional processed (CP) sample and the bottom panel is the OP sample. Both have clear fractional spots and the line profiles show that the background is low. This indicates that the OP sample surface is well ordered and has the same symmetry as the CP surface.

To confirm that the OP surface is still terminated with a B layer, LEED IV curves are taken and compared with the CP surface. As shown in Figure 4.2, the peak locations and shapes are almost the same for OP and CP surfaces. The R factors are also calculated to quantify the

difference. The R factors for integral spots (1,0) and (2,0) are 0.21 and 0.15 respectively, and for the fractional spots (1/2, 1/2) and (3/2, 3/2), 0.31 and 0.30. These low R factors confirm that the two surfaces have similar atom locations. In conclusion, LEED experiments suggest that the OP surface has the same symmetry and termination as CP surfaces.

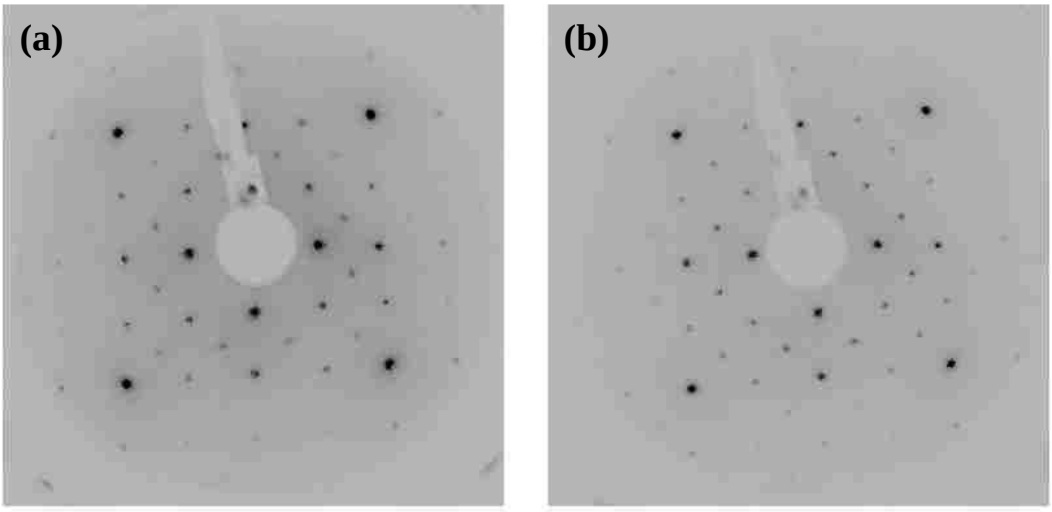


Figure 4.1 LEED pattern of CP(a) and OP(b) $Fe_3O_4$ (001) surface. Both patterns are taken at room temperature and 90 eV beam energy.

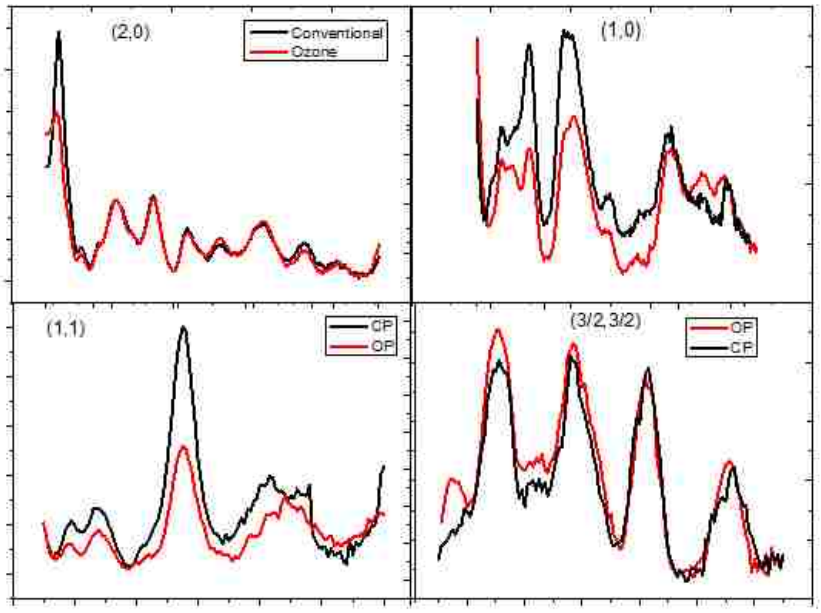


Figure 4.2 LEED IV curve comparison of OP and CP $Fe_3O_4$ (001) surface.

After a clean and ordered OP surface is achieved, hydrogen adsorption is performed using the same procedure as with CP surfaces. As shown in Figure 4.3, the LEED pattern nearly disappears after exposure to hydrogen. Only the strongest integer spots are visible, indicating that the surface is disordered due to hydrogen adsorption. This is different for the CP surface, on which all the integral spots are clearly observed even on a hydrogen-saturated surface.

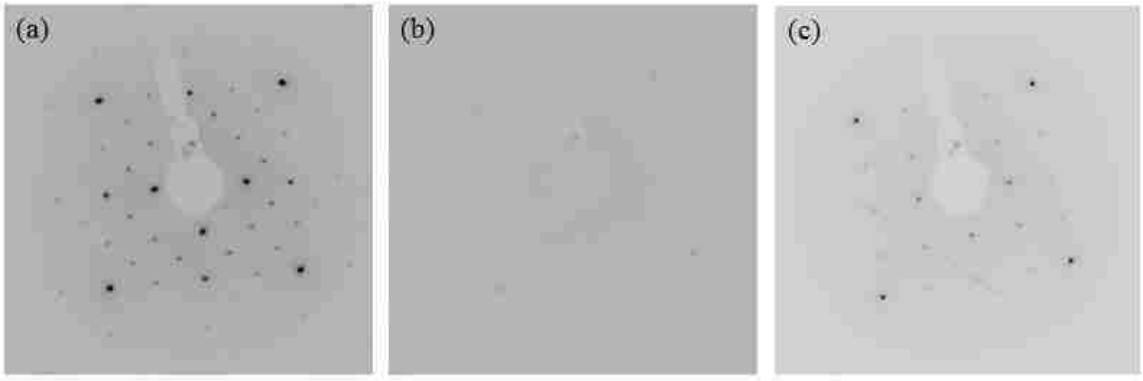


Figure 4.3 LEED pattern (beam energy is 90eV) of hydrogen adsorption on OP $Fe_3O_4$ surface. (a)clean, (b)H saturated, (c)after desorption at 700K.

The hydrogen saturated OP surface is then heated up to desorb surface H. Integer spots are recovered after the sample is heated to nearly 600K, which is higher than needed for the CP surface. This indicates the different hydrogen bondings on these two surfaces. Continued heating of the sample up to an annealing temperature 900K does not clearly change the observed LEED pattern, keeping its (1×1) symmetry. This is different from the CP surface where a sharp $\left(\sqrt{2}\times\sqrt{2}\right)R45°$ LEED pattern is recovered. Therefore, the surface symmetry is changed upon hydrogen adsorption and desorption, while here annealing is not able to recover the surface termination.

In conclusion, ozone processing produced a well ordered $\left(\sqrt{2}\times\sqrt{2}\right)R45°$ symmetry $Fe_3O_4$ B termination surface, which was also observed with conventionally process surfaces. However, after hydrogen adsorption, OP surface is disordered and only the strongest integral

spots are still visible. After desorption, LEED pattern becomes (1×1) and does not recover its original $(\sqrt{2} \times \sqrt{2})R45°$ symmetry. Therefore, although clean CP and OP surfaces have the same symmetry, they perform differently upon hydrogen adsorption.

**4.2 X-ray Photoemission Spectroscopy (XPS)**

In Chapter 3, XPS O 1s spectrum found the existence of surface oxygen vacancies on CP samples. As one of the best techniques for identifying oxygen vacancies, XPS experiments are performed on OP samples as well.

As shown in Figure 4.4, the XPS O 1s peak is much more symmetric after ozone treatment. A similar fitting process performed for the CP surface is used here, where the green component is the ionic oxygen contribution and the red component is the combination of other complex interactions. The peak area of ionic oxygen in the OP surface is more than 93%, compared to only 74% on the CP surface. This indicates that there are effectively no surface oxygen vacancies after ozone treatment and that a truly stoichiometric $Fe_3O_4$ (001) surface if formed.

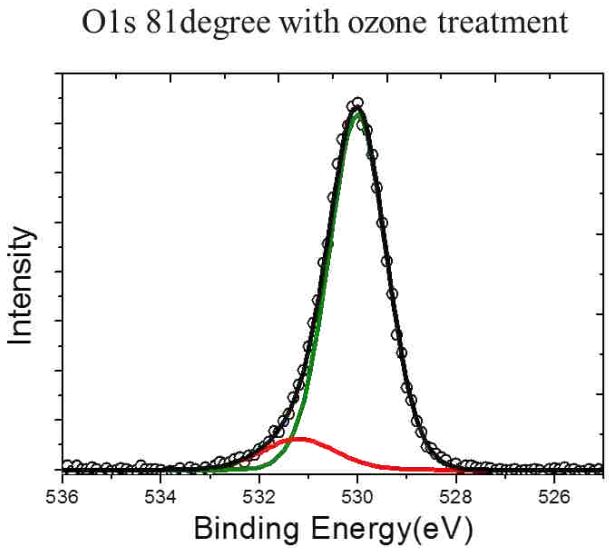


Figure 4.4 O 1s peak on clean OP $Fe_3O_4$ surface, photoelectron emission angle is 81° degree.

Fe 2p peaks are also measured for normal emission angle XPS. As shown in Figure 4.5, the black curve on top is the CP sample and the black curve on bottom is from the OP sample. After ozone treatment, the $Fe^{2+}$ shoulder is clearly weakened, as only a tiny kink can be observed. This indicates that the surface oxygen vacancies are filled with the oxygen atoms provided by ozone gas, and therefore oxidize the surface iron atoms.

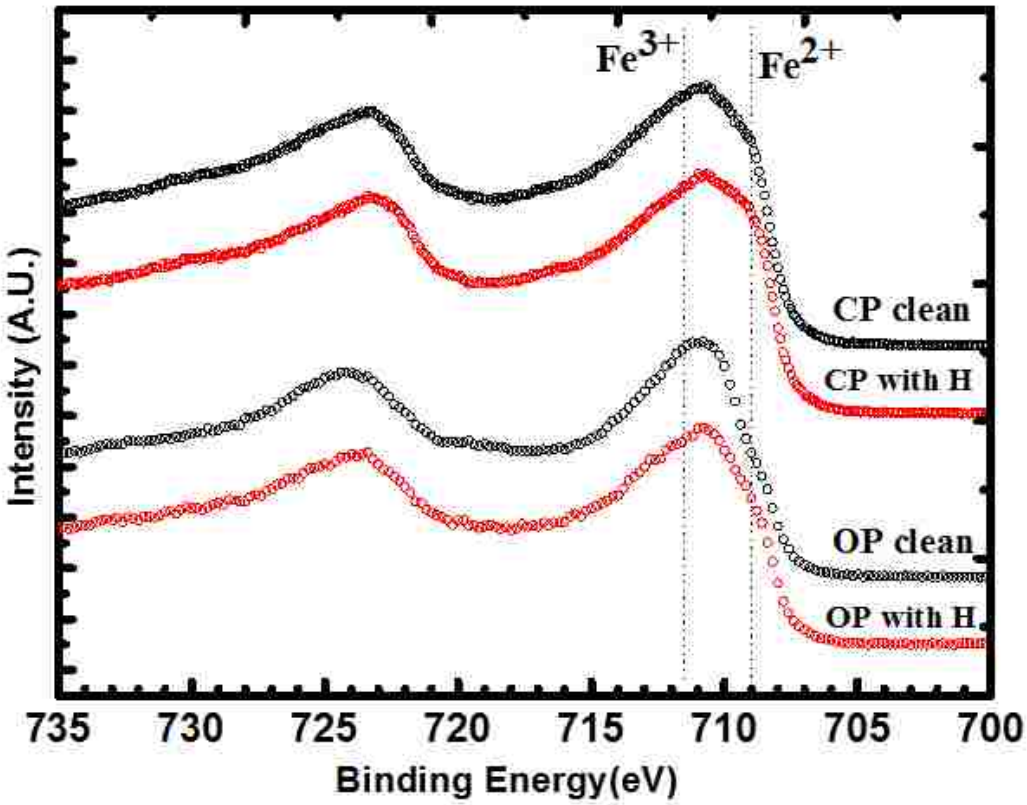


Figure 4.5 XPS Fe 2p spectra taken at normal emission angle. CP and OP are compared upon hydrogen adsorption

At this stage, combining the XPS and LEED experiments, one can conclude that ozone treatment successfully fills all surface oxygen vacancies. Surface symmetry and $Fe_3O_4$ B termination are retained upon ozone treatment, and a true stoichiometric surface is created.

Hydrogen adsorption experiments are measured by XPS as well. As shown in the Fe 2p peak, the $Fe^{2+}$ shoulder is enhanced after hydrogen adsorption. But even after hydrogen

adsorption, the intensity of the $Fe^{2+}$ shoulder is still much lower than that of the clean CP surface. This indicates that the influence by hydrogen on the surface iron valence is much smaller than that from the oxygen vacancies. This suggests that the concentration of oxygen vacancies on CP surface could be large.

As mentioned in Chapter 3, if there were OH species on the surface, a high binding energy peak should appear around 532 eV. It is not until now that the signal of hydroxyl is finally discovered on the hydrogen covered OP surface. As shown in Figure 4.6, a clear shoulder is observed after hydrogen adsorption at the required energy. This proves that atomic hydrogen bonds to surface oxygen on ozone processed $Fe_3O_4$ surfaces. This result is consistent with previous DFT calculations where hydrogen bonds to surface oxygen on stoichiometric $Fe_3O_4$ surfaces.[41]

These experiments helped ensure the uncovered insights into the surface and adsorption properties of this material were accurate. First, they proved our previous experiments on CP surfaces were correct. Although many control experiments are always done, instrumental error could feasibly have induced a failure in discovering hydroxyl on hydrogen covered CP $Fe_3O_4$ surfaces. However, after these experiments, there can be no doubt that hydroxyl did not exist in our first series of measurements. Secondly, it confirmed that the counter intuitive H-Fe bonding is induced by surface oxygen vacancies. From a theoretical point of view, one may imagine that atomic hydrogen would bond to oxygen preferentially over iron. After these findings, it has been proven that on a stoichiometric surface, hydrogen does indeed bond to surface oxygen, agreeing with all calculation results. The difference between CP and OP surfaces is in their oxygen vacancies, which is the origin of H-Fe vs H-O bonding. This then finally closes the gap between our results and theory.

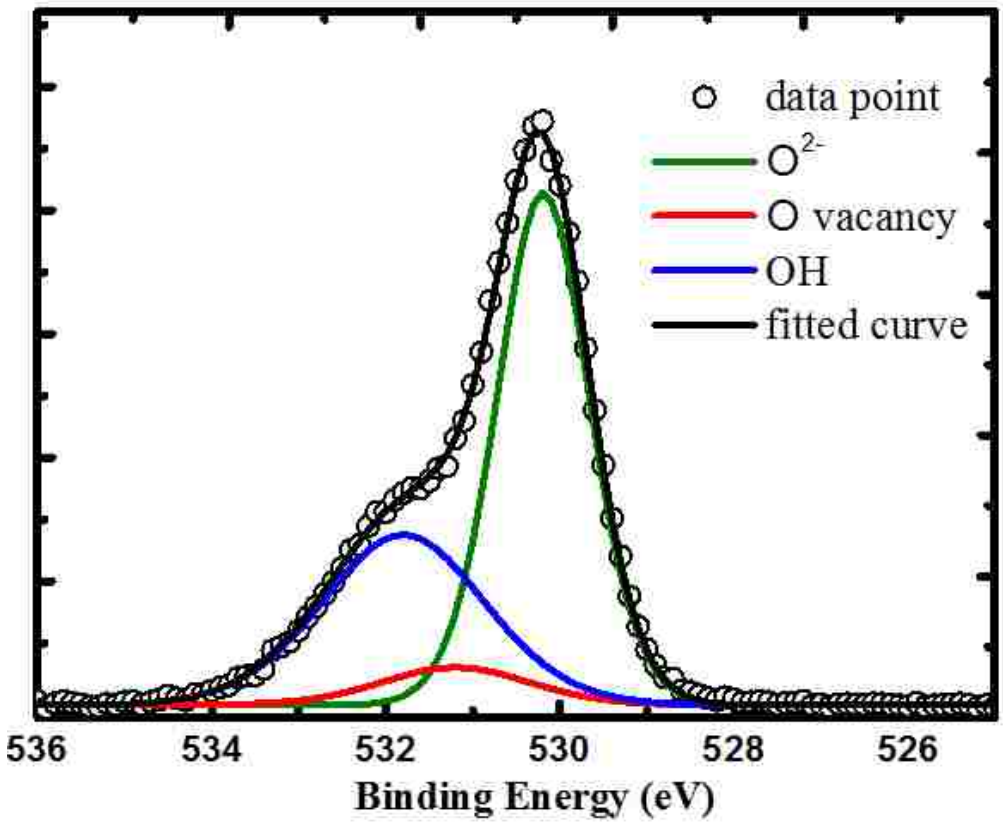


Figure 4.6 O 1s spectra taken at 81 degree emission angle on hydrogen saturated OP $Fe_3O_4$ surface

The XPS O 1s peak after hydrogen adsorption is also fitted with three peaks, due to ionic Fe, shake-off contributions, and OH contributions. The results are listed in Table 4.1 Comparing clean CP and OP surfaces, the peak not only becomes symmetric, but also increases in total area as well. This is reasonable if the surface receives extra oxygen to fill the vacancies. Although these two measurements are taken separately, which could introduce error on the peak area, the sample position and optical parameters are kept the same between measurements. According to experiments on the same sample at different measurement times, the peak error is smaller than 5%. So the truly oxygen 1s peak area on the CP and OP surfaces should be 440±22 and 520±26, respectively. The oxygen peak area change is ~10%-30%, which while not a high precision analysis, still gives us some insight into the oxygen vacancy concentration on our CP surface.

Table 4.1 O1s peak total area and area percentage of different components.

| | $O^{2-}$ | $O_v$ | OH | Total Area(a.u.) |
|---|---|---|---|---|
| CP surface(0°) | 65% | 35% | N/A | 15690 |
| CP surface(81°) | 63% | 37% | N/A | 444 |
| OP surface(81°) | 85% | 15% | N/A | 520 |
| OP with H(81°) | 64% | N/A | 36% | 477 |

After hydrogen adsorption, the peak area reduced from 520 to 477. This is because hydrogen coverage on the surface makes the contribution from surface oxygen smaller. The hydrogen bonded oxygen 1s peak weight is 36%. Recalling that the contribution ratio of first layer to second layer is 1:0.2, the contribution from the second layer oxygen is then 16%. Assuming hydrogen only bonds to surface oxygen, the second layer oxygen atoms remain ionic after hydrogen exposure, and thus 47% of the contribution comes from ionic oxygen. This is very close to the weight of hydrogen bonded oxygen. It indicates that about half of surface oxygen atoms bond to hydrogen. In other words, the saturation coverage of atomic hydrogen on stoichiometric $Fe_3O_4$ surface is 4 H atoms per $\left(\sqrt{2}\times\sqrt{2}\right)R45°$ unit cell. This conclusion agrees with DFT calculation results on stoichiometric modified B termination $Fe_3O_4$.[53]

Desorption experiments are done to measure the change of hydrogen bonded oxygen 1s shoulders with temperature. As shown in Figure 4.7, the hydrogen saturated OP surface is heated in steps. A clear change occurs at ~600K, where the OH shoulder clearly weakens. Further heating does not change the shape of O 1s peak. Therefore, 600K is the desorption temperature of hydrogen on the OP surface, which is higher than the desorption temperature on the CP surface. This is because OH bonding is much stronger than H-Fe bonding, thus requiring more energy to break the bonding and release bonded hydrogen. The peak area is recovered as well after desorption.

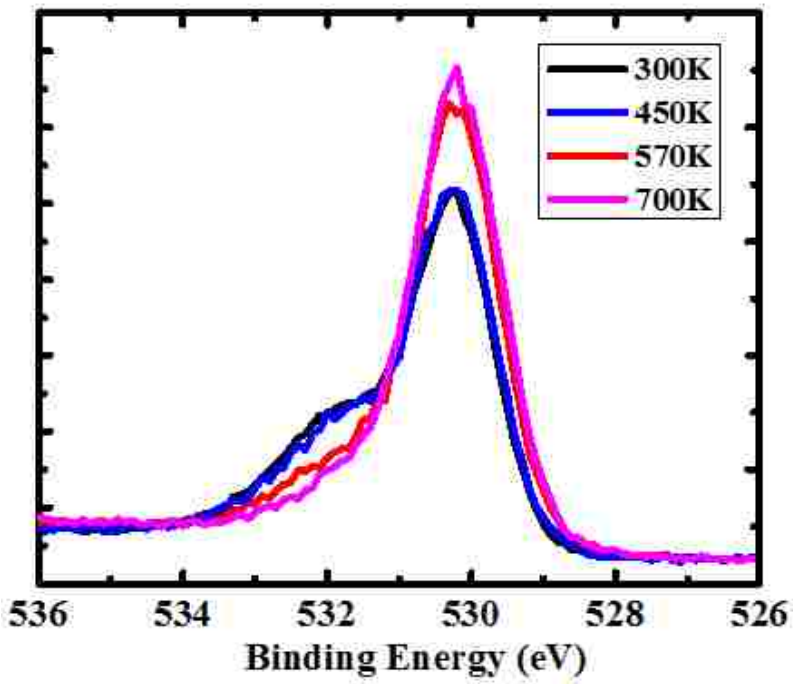


Figure 4.7 O 1s spectra taken at 81 degree emission angle during desorption process. Black curve is hydrogen saturated surface, then $Fe_3O_4$ sample is heated in small steps. The 532 eV shoulder largely suppressed when sample is heated to 570K and get stable at 700K.

In summary, XPS experiments on OP surface have confirmed that ozone treatment effectively removes all surface vacancies and produces a stoichiometric surface. O 1s peak measurements of the hydrogen covered OP surface successfully discovered a peak located at 532 eV which is assigned to the hydrogen bonded surface oxygen. Quantitative analysis suggests that 4H exist in one unit cell at the saturation condition, agreeing with DFT calculation results. Higher desorption temperatures confirmed the existence of OH bonding which is stronger than H-Fe bonding.

**4.3 HREELS**

In Chapter 3, we stated that the strongest evidence of OH bonding is directly observing OH vibrational modes at ~450 meV with HREELS. However, we failed to observe this signature peak on our hydrogen covered CP surfaces, which was later shown to be due to the absence of

OH on that surface. In the previous section, we have successfully observed hydrogen bonded oxygen O 1s shoulders through XPS, which confirmed the formation of OH bonding on OP surfaces. Our next step then is to confirm the existence of OH by HREELS.

The ozone processing equipment is attached to a different system than the HREELS chamber, which makes *in situ* sample transfer impossible. A vacuum suitcase has been designed to transfer samples in vacuum between different systems. The vacuum suitcase consists of one magnetic arm, one ion pump, one ion gauge, one gate valve and one small chamber. The sample holder is designed to be compatible with both sample transfer systems. The ion pump can maintain a $1\times10^{-9}$ Torr vacuum environment, which ensures that the surface remains clean during transfer.

To measure the hydrogen covered OP surfaces with HREELS, the samples were treated with ozone in ozone chamber and exposed to hydrogen for 30 minutes. Surface condition is the checked by LEED and XPS to make sure hydrogen is adsorbed. The transfer from the ozone chamber to HREELS takes 3 hours. After the sample was loaded into the HREELS chamber, its surface was checked again with LEED to ensure no changes happened during the transfer.

The hydrogen covered OP surface is then measured by HREELS. As shown in Figure 4.8, the two main peaks at 50 meV and 80 meV are still at the same location, though the 80 meV peak on the OP surface is much stronger compared to the CP surface. That indicates the OP surface is a much better surface, with less oxygen vacancies.

When the ~450 meV region is scanned, a clear wide peak is observed. This is the desired signal of the OH vibrational mode. The appearance of the OH vibrational mode proves that hydrogen bonds to surface oxygen on the OP surface, which is consistent with our XPS results.

This peak is wider than usual, which may be caused by some intrinsic interactions. After degasing, the OH peaks disappeared while the peaks at 50, 80 meV remain.

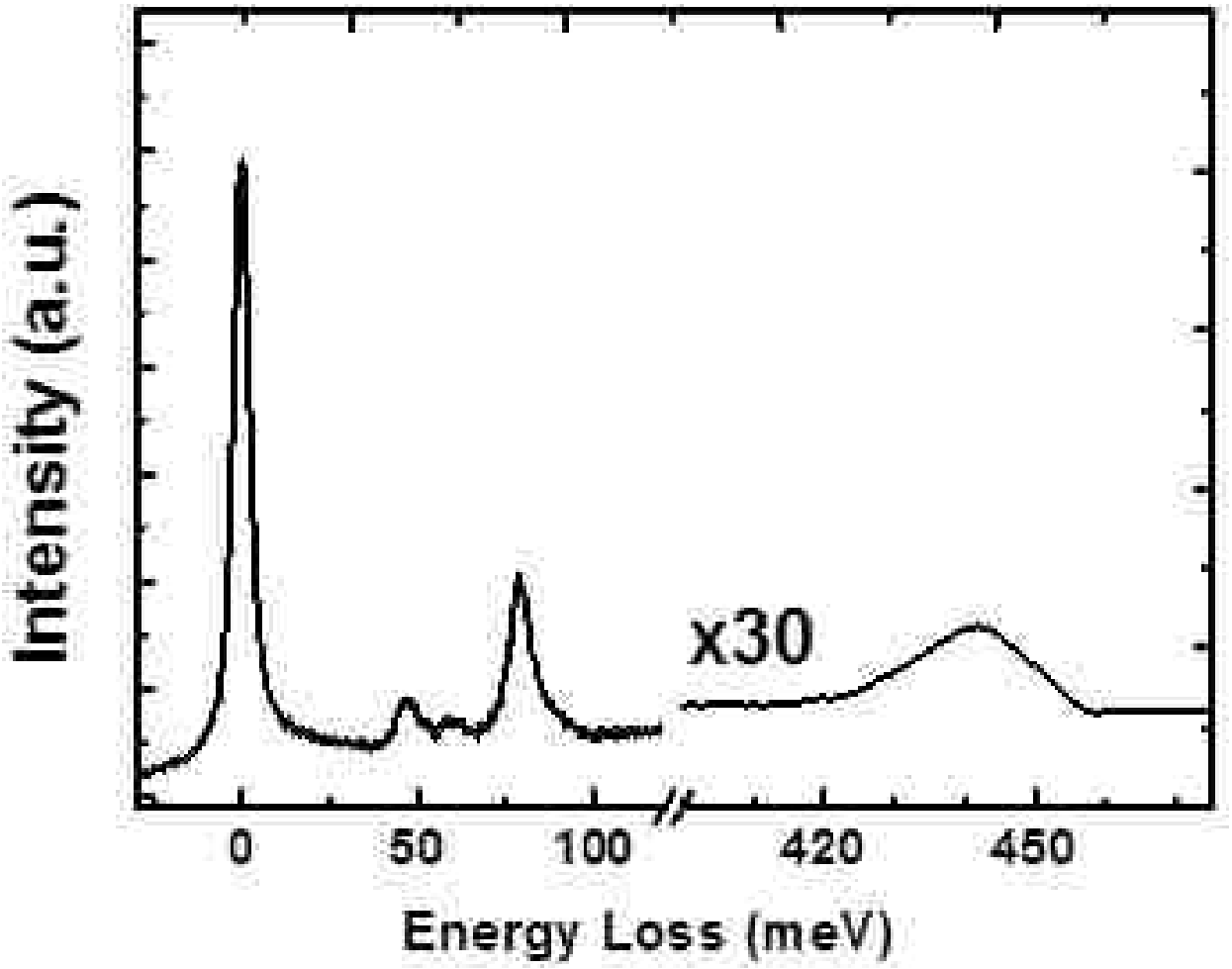


Figure 4.8 HREELS spectra on hydrogen saturated OP $Fe_3O_4$ (001) surface. The range around 450 meV is enlarged 30 times.

In summary, the observation of the OH vibrational mode at 450 meV confirms that hydrogen bonds to surface oxygen on OP surfaces, which is consistent with our XPS results. Combining HREELS and XPS results, we have proved that the hydrogen adsorption mechanism on the OP surface agrees with DFT calculations for hydrogen adsorption on a stoichiometric surface.

## 4.4 Scanning Electron Microscopy (SEM)

Scanning electron microscopy is a good technique if one wants to investigate the surface structure after desorption. After H adsorption and desorption on OP surface, the crystal surface shows some small features even can be observed by eye.

Using optical microscopy, lines perpendicular to each other on the surface are observed. To achieve better view of this surface, better resolution is acquired, that's why SEM experiments are performed.

Since magnetite surface is not reactive, sample can be transferred in air without morphology change. Actually, after exposing a good clean surface to air for less than one hour and putting it back to UHV chamber, clear LEED pattern can still be observed. That indicated this surface does not change much after exposing to air.

As shown in Figure 4.9, in the 300 um × 300 um range, large perpendicular stripes are observed, which means that the surface is destroyed and is no longer a single crystal.

However, this surface still gives a (1×1) LEED pattern, so there must still be ordered features on the surface despite this. In order to see what is in the black and white region, we zooming in the image to the 60 um × 60 um scale, some small white spots are discovered between stripes. Continuing to zoom in to the 15 um x 15 um scale, it is seen that the white "spots" are actually beautiful small crystals. They are octahedral in structure and can have different sizes, including larger crystals that are combinations of two octahedrons. Octahedral structure yields (1×1) symmetry, which explains our continued observation of (1×1) LEED patterns despite the larger defects.

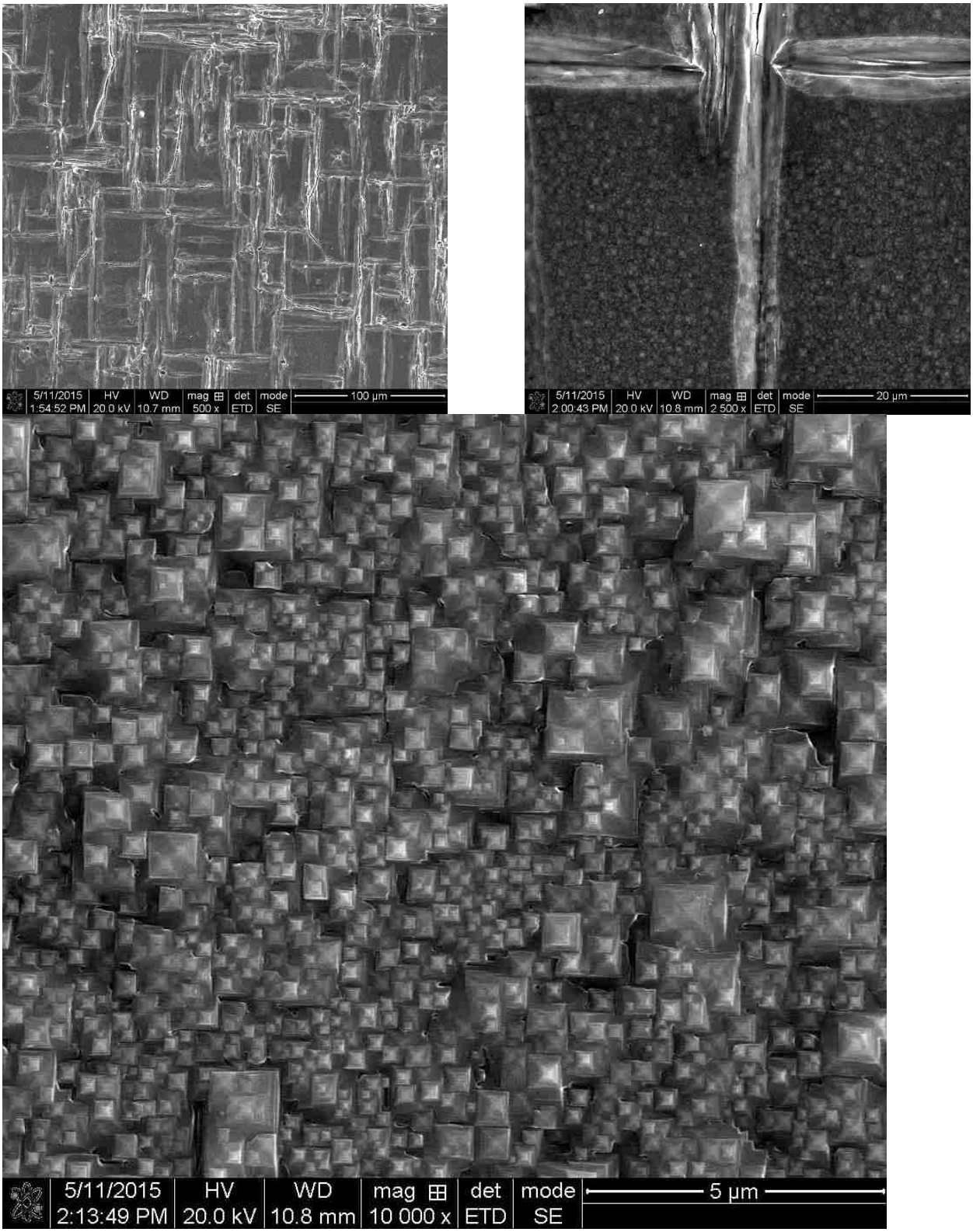


Figure 4.9 SEM image on hydrogen desorbed OP $Fe_3O_4$ surface. (a) 300 um×300 um (b) 60 um×60 um (c) 15 um×15 um

The elementary contribution is measured by Energy Dispersive Spectroscopy (EDS) built in with SEM. As shown in Figure 4.10, the whiter region is about 6% of the whole image, while the darker area is 91%. The elemental concentrations in white and dark regions are shown in Figure 4.11. The Fe peak intensity is much stronger in the dark region than in the white. This is because the oxygen rich area will produce more secondary electrons and make this area brighter in the image. No contamination peaks such as carbon are observed, indicating that the surface is relatively clean even after *ex situ* sample transferring.

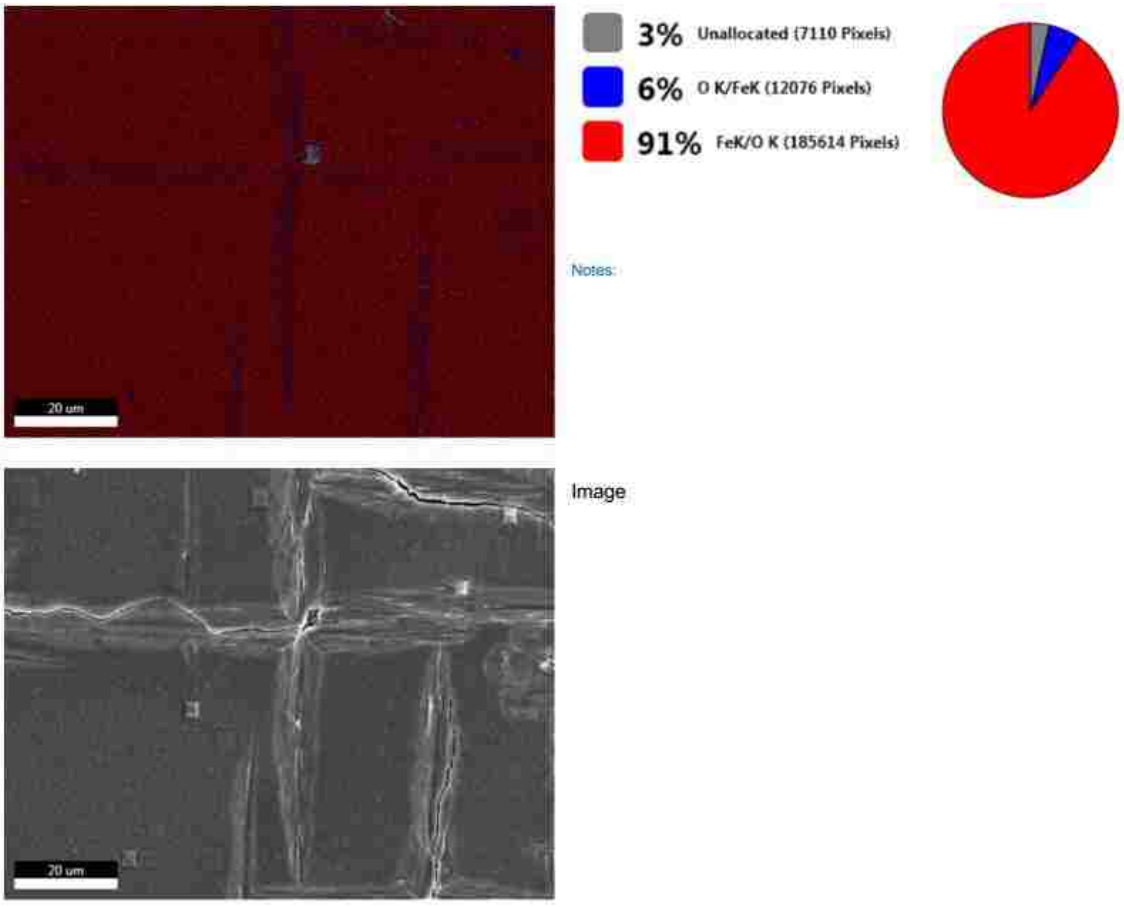


Figure 4.10 elementary distribution image on hydrogen desorbed OP $Fe_3O_4$ surface. Blue region is where oxygen is more concentrated than iron, red region is where iron is more than oxygen

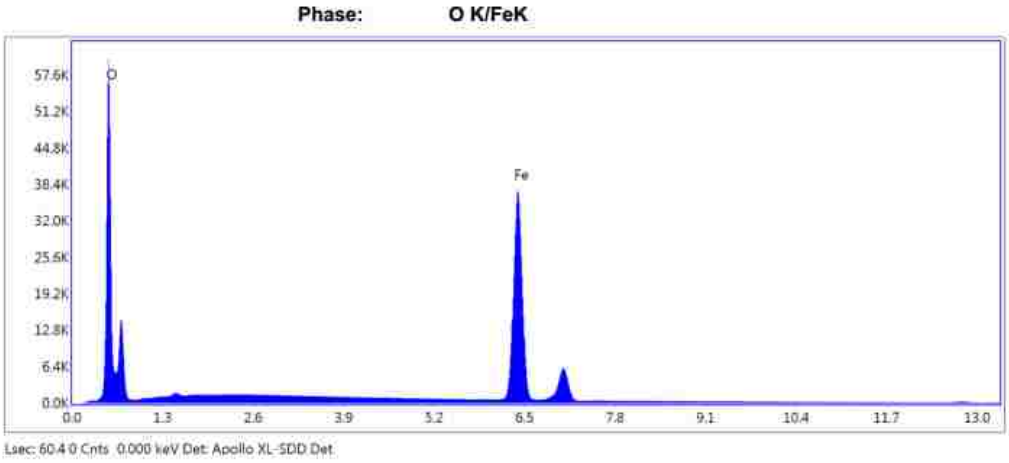


**eZAF Smart Quant Results**

| Element | Weight % | Atomic % | Net Int. | Error % | Kratio | Z | R | A | F |
|---|---|---|---|---|---|---|---|---|---|
| O K | 34.15 | 64.42 | 7426.9 | 5.41 | 0.22 | 1.16 | 0.91 | 0.56 | 1.00 |
| FeK | 65.85 | 35.58 | 9649.4 | 1.75 | 0.62 | 0.90 | 1.04 | 1.01 | 1.03 |

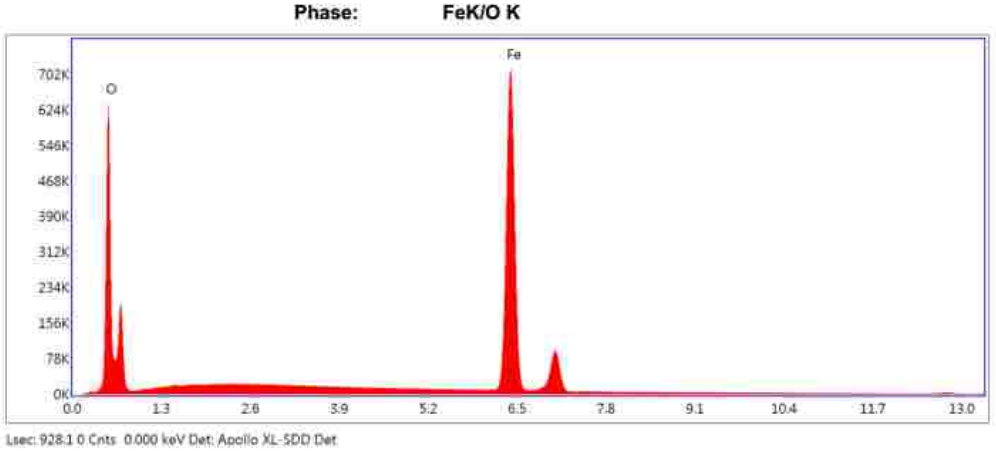


**eZAF Smart Quant Results**

| Element | Weight % | Atomic % | Net Int. | Error % | Kratio | Z | R | A | F |
|---|---|---|---|---|---|---|---|---|---|
| O K | 24.41 | 52.99 | 5264.6 | 5.69 | 0.15 | 1.19 | 0.90 | 0.53 | 1.00 |
| FeK | 75.59 | 47.01 | 11722.4 | 1.60 | 0.73 | 0.93 | 1.03 | 1.01 | 1.03 |

Figure 4.11 Energy dispersion X-ray spectroscopy (EDS) measurement on the blue and red area in Figure 4.10

SEM shows that the OP surface after desorption is completely changed to polycrystalline. This is consistent with perpendicular oxygen rich stripes and many small octahedrons in the dark area. The octahedrons induce the (1×1) LEED pattern after desorption.

**4.5 Summary**

A novel ozone treatment is performed on $Fe_3O_4$ single crystal (001) surfaces in this chapter in an attempt to avoid surface oxygen vacancies.

A stoichiometric $Fe_3O_4$ (001) surface is created by the ozone treatment. Surface quality is checked by LEED, XPS and HREELS. One concern of treating $Fe_3O_4$ with ozone is the possibility of changing the sample into $Fe_2O_3$. $Fe_2O_3$ lattice is hexagonal structure however and would thus have totally different LEED pattern than what was observed. The surface after ozone treatment still obtains a $(\sqrt{2} \times \sqrt{2})R45°$ reconstruction structure, which rules out a termination of $Fe_2O_3$. Although the XPS Fe 2p peak shows oxidation of $Fe^{2+}$ to $Fe^{3+}$, the normal emission spectra still exhibits spectra weight of $Fe^{2+}$, indicating that the inside layers are not oxidized and therefore the sample structure and symmetry are still B termination $Fe_3O_4$. Only the surface is oxidized by the extra oxygen atoms filling the vacancies. Fitting the results of the XPS O 1s spectra confirmed that an OP surface does not have oxygen vacancies, so we can conclude that the OP $Fe_3O_4$ surface is stoichiometric.

Hydrogen adsorption experiments on the OP surface verified previous DFT calculations by Pentcheva. OH bonding is clearly observed by XPS and HREELS, both of which find the signatures of hydroxyl. The higher desorption temperature of hydrogen covered OP surfaces also confirm that hydrogen bonds to oxygen instead of Fe here.

The importance of these ozone treatment experiments are twofold. First, it is the first time a stoichiometric $Fe_3O_4$ surface has been achieved on a $Fe_3O_4$ single crystal. It has been proven

that the CP surface has ordered oxygen vacancies on the surface, showing that that previous studies and results for $Fe_3O_4$ (001) have been based on vacancies and not stoichiometric surfaces. Secondly, hydrogen adsorption on OP surfaces has proven that the H-Fe bonding on CP is due to surface oxygen vacancies.

# CHAPTER 5 DISCUSSION AND CONCLUSION

The hydrogen adsorption mechanisms for $Fe_3O_4$ (001) surfaces are determined and understood in this dissertation. Several unsolved questions have been answered utilizing a variety of experimental surface measurement techniques.

Firstly, the location of hydrogen bonding on a CP $Fe_3O_4$ (100) surface was determined. The existence of large amount OH species on the surface after hydrogen adsorption was ruled out with HREELS, XPS and LEIS. Unexpectedly, the existence of H-Fe bonding is proven by the observance of H-Fe vibrational modes with HREELS, H shadowing effect on Fe with LEIS, and H-Fe bonding electron states with UPS, revealing that the adsorption site of atomic hydrogen is mainly at surface Fe and not O. The adsorption site is found to be at Fe bridge sites according to HREELS and UPS. The H-Fe vibration frequency on the CP $Fe_3O_4$ surfaces match the H-Fe vibration on Fe metal surfaces, as do the UPS spectra shape on H/ $Fe_3O_4$ and H/Fe. The bridge adsorption sites also explain the bright protrusion pairs in STM, as two Fe atoms next to the adsorbed H will bond to H and become bright in the STM images.

Secondly, we determined what induced the H-Fe bonding instead of OH on the CP surface. Inspired by the H-Ti bonding formation on highly oxygen deficient TiO2 surface and asymmetric O 1s peaks in XPS, surface oxygen vacancy was suspected to be the most plausible reason. To confirm whether there are oxygen vacancies on the CP surface, ozone treatment is performed. Combining experimental results from multiple surface techniques, it is shown that the OP surface is a stoichiometric $Fe_3O_4$ (001) B termination, while the CP surface is oxygen deficient. Further hydrogen exposure on an OP surface results in OH bonding, as theoretical calculations predicted. Therefore, surface oxygen vacancies on the CP $Fe_3O_4$ surface produces the unconventional H-Fe bonding over OH; on a stoichiometric surface, H still bonds to oxygen.

Thirdly, we delved into why no OH bonding was observed upon hydrogen adsorption on the CP surface. Even if hydrogen prefers surface Fe because of O vacancies, hydrogen should still be able to bond to surface oxygen. Desorption experiments on an H saturated CP surface revealed a two-step desorption process. During desorption, hydrogen desorbs as molecular hydrogen at 500K first while leaving the surface deconstructed, after which the surface is recovered to a $(\sqrt{2} \times \sqrt{2})R45°$ reconstruction after 750K is reached. After hydrogen desorbs from Fe sites, there may be small amount of OH on the surface, which need higher temperature to desorb. When the temperature is higher enough, H desorb from O sites, thus LEED and LEIS O peak both recovered.

In this work, it has been shown that the CP surface is oxygen deficient, which means that all previous experimental work on $Fe_3O_4$ single crystals have been performed on non-stoichiometric surfaces. Truly stoichiometric surfaces can be produced by ozone treatment. This finding will be important for future research on $Fe_3O_4$.

To identify the exactly adsorption site, angle resolved LEIS can be used with an in plain rotatable sample holder. By analyzing the symmetry of the peak intensity changes along with sample azimuthal angle, the symmetry of the adsorption site can be determined. DFT calculation of the hydrogen adsorption on the CP $Fe_3O_4$ surface has not been undertaken yet. It can provide important details into the progress of water formation and desorption after hydrogen adsorption, as well as the adsorption energies on each site with different oxygen vacancy concentrations.

# REFERENCES


[1] Y. Yamanishi, S. Sakuma, K. Onda, F. Arai, Biomedical microdevices 12 (2010) 745.

[2] M. Liu, O. Obi, J. Lou, Y. Chen, Z. Cai, S. Stoute, M. Espanol, M. Lew, X. Situ, K.S. Ziemer, Advanced Functional Materials 19 (2009) 1826.

[3] Y.-J. Chen, F. Zhang, G.-g. Zhao, X.-y. Fang, H.-B. Jin, P. Gao, C.-L. Zhu, M.-S. Cao, G. Xiao, The Journal of Physical Chemistry C 114 (2010) 9239.

[4] L.F. Chen, C. Ong, C. Neo, V.V. Varadan, V.K. Varadan, Microwave electronics: measurement and materials characterization, John Wiley & Sons, 2004.

[5] Y.S. Kang, S. Risbud, J.F. Rabolt, P. Stroeve, Chemistry of Materials 8 (1996) 2209.

[6] J. Ding, T. Reynolds, W. Miao, P. McCormick, R. Street, Applied physics letters 65 (1994) 3135.

[7] R. Schlögl, Ammonia Synthesis, Wiley Online Library, 2008.

[8] F. Pinna, T. Fantinel, G. Strukul, A. Benedetti, N. Pernicone, Applied Catalysis A: General 149 (1997) 341.

[9] L. Huazhang, H. Zhangneng, L. Xiaonian, L. Yanying, J. Zurong, Journal of Chemical Industry and Engineering (China) 4 (1994) 000.

[10] S. Li, A. Li, S. Krishnamoorthy, E. Iglesia, Catalysis Letters 77 (2001) 197.

[11] S. Li, S. Krishnamoorthy, A. Li, G.D. Meitzner, E. Iglesia, Journal of Catalysis 206 (2002) 202.

[12] B. Wu, L. Tian, H. Xiang, Z. Zhang, Y.-W. Li, Catalysis Letters 102 (2005) 211.

[13] D.S. Newsome, Catalysis Reviews Science and Engineering 21 (1980) 275.

[14] M. Estrella, L. Barrio, G. Zhou, X. Wang, Q. Wang, W. Wen, J.C. Hanson, A.I. Frenkel, J.A. Rodriguez, The Journal of Physical Chemistry C 113 (2009) 14411.

[15] C. Rhodes, B.P. Williams, F. King, G.J. Hutchings, catalysis communications 3 (2002) 381.

[16] J. Connerney, M. Acuna, P. Wasilewski, G. Kletetschka, N. Ness, H. Reme, R. Lin, D. Mitchell, Geophys. Res. Lett 28 (2001) 4015.

[17] D. Tarling, F. Hrouda, Magnetic anisotropy of rocks, Springer Science & Business Media, 1993.

[18] M. Galvez, P. Loutzenhiser, I. Hischier, A. Steinfeld, Energy & Fuels 22 (2008) 3544.

[19] P. Loutzenhiser, M. Gálvez, I. Hischier, A. Stamatiou, A. Frei, A. Steinfeld, Energy & Fuels 23 (2009) 2832.

[20] K. Simeonidis, M. Tziomaki, M. Angelakeris, C. Martinez-Boubeta, L. Balcells, C. Monty, M. Mitrakas, G. Vourlias, N. Andritsos, Development of iron-based nanoparticles for Cr (VI) removal from drinking water, EPJ Web of Conferences. EDP Sciences, 2013, p. 08007.

[21] N. Tsuda, K. Nasu, A. Yanase, K. Siratori, (1991).

[22] D. Schrupp, M. Sing, M. Tsunekawa, H. Fujiwara, S. Kasai, A. Sekiyama, S. Suga, T. Muro, V. Brabers, R. Claessen, EPL (Europhysics Letters) 70 (2005) 789.

[23] E.J. Verwey, P.W. Haayman, F.C. Romeijn, The Journal of Chemical Physics 15 (1947) 181.

[24] F. Walz, Journal of Physics: Condensed Matter 14 (2002) R285.

[25] S. Chikazumi, S. Charap, Co., New York (1978) 168.

[26] P. Weiss, R. Foner, Ann Phys 12 (1929) 297.

[27] L. Bickford Jr, Physical Review 78 (1950) 449.

[28] T. Okamura, Rep. Tohoku Imp. Univ. Ser 1 (1932) 231.

[29] L. Bickford Jr, Reviews of Modern Physics 25 (1953) 75.

[30] F. Walz, V. Brabers, S. Chikazumi, H. Kronmüller, M. Rigo, physica status solidi (b) 110 (1982) 471.

[31] F. Walz, H. Kronmüller, physica status solidi (b) 160 (1990) 661.

[32] F. Walz, H. Kronmüller, physica status solidi (b) 181 (1994) 485.

[33] P.W. Anderson, Physical review 109 (1958) 1492.

[34] N. Tombs, H. Rooksby, Acta Crystallographica 4 (1951) 474.

[35] S. Chambers, S. Joyce, Surface science 420 (1999) 111.

[36] Y. Kim, Y. Gao, S. Chambers, Surface science 371 (1997) 358.

[37] S.A. Chambers, S. Thevuthasan, S.A. Joyce, Surface science 450 (2000) L273.

[38] G.S. Parkinson, N. Mulakaluri, Y. Losovyj, P. Jacobson, R. Pentcheva, U. Diebold, Physical Review B 82 (2010).

[39] J. Rustad, E. Wasserman, A. Felmy, Surface science 432 (1999) L583.

[40] B. Stanka, W. Hebenstreit, U. Diebold, S. Chambers, Surface science 448 (2000) 49.

[41] R. Pentcheva, F. Wendler, H.L. Meyerheim, W. Moritz, N. Jedrecy, M. Scheffler, Physical Review Letters 94 (2005).

[42] R. Pentcheva, W. Moritz, J. Rundgren, S. Frank, D. Schrupp, M. Scheffler, Surface Science 602 (2008) 1299.

[43] P. Nordlander, S. Holloway, J. Nørskov, Surface science 136 (1984).

[44] K. Christmann, Surface Science Reports 9 (1988).

[45] M.S. Daw, M.I. Baskes, Physical Review Letters 50 (1983) 1285.

[46] C. Beachem, Metallurgical transactions 3 (1972) 441.

[47] M. Louthan, G. Caskey, J. Donovan, D. Rawl, Materials Science and Engineering 10 (1972) 357.

[48] L. Schlapbach, A. Züttel, Nature 414 (2001) 353.

[49] A.D.K. Jones, T. Bekkedahl, Nature 386 (1997) 377.

[50] N.L. Rosi, J. Eckert, M. Eddaoudi, D.T. Vodak, J. Kim, M. O'Keeffe, O.M. Yaghi, Science 300 (2003) 1127.

[51] J.L. Rowsell, O.M. Yaghi, Angewandte Chemie International Edition 44 (2005) 4670.

[52] M. Kurahashi, X. Sun, Y. Yamauchi, Physical Review B 81 (2010).

[53] N. Mulakaluri, R. Pentcheva, The Journal of Physical Chemistry C 116 (2012) 16447.

[54] G.S. Parkinson, N. Mulakaluri, Y. Losovyj, P. Jacobson, R. Pentcheva, U. Diebold, Phys Rev B 82 (2010).

[55] I. Langmuir, Journal of the American Chemical Society 40 (1918) 1361.

[56] L.N. Rozanov, Measurement Science and Technology 13 (2002) 1654.

[57] L. Cristina, R. Vidal, J. Ferron, Surface Science 602 (2008) 3454.

[58] A. Müller, F. Hartmann, S. Paul, G. Petzoldt, R. Picker, M. Simson, H.-F. Wirth, O. Zimmer, W. Carli, Nuclear Instruments and Methods in Physics Research Section A: Accelerators, Spectrometers, Detectors and Associated Equipment 582 (2007) 395.

[59] I. Popova, R. Muha, Z. Chen, J. Yates Jr, Journal of Vacuum Science & Technology A 21 (2003) 401.

[60] E. Taglauer, W. Heiland, Applied physics 9 (1976) 261.

[61] A.D. van der Gon, R. Cortenraad, W. Jansen, M. Reijme, H. Brongersma, Nuclear Instruments and Methods in Physics Research Section B: Beam Interactions with Materials and Atoms 161 (2000) 56.

[62] H. Hertz, Annalen der Physik 267 (1887) 983.

[63] P. Innes, Proceedings of the Royal Society of London. Series A, Containing Papers of a Mathematical and Physical Character 79 (1907) 442.

[64] K. Siegbahn, E. der Mateosian, American Journal of Physics 23 (1955) 548.

[65] B. Bhushan, Springer handbook of nanotechnology, Springer Science & Business Media, 2010.

[66] A.P. Grosvenor, B.A. Kobe, M.C. Biesinger, N.S. McIntyre, Surface and Interface Analysis 36 (2004) 1564.

[67] P. Cox, W. Flavell, A. Williams, R. Egdell, Surface Science 152 (1985) 784.

[68] D. Mills, Surface Science 48 (1975) 59.

[69] S.R. Bare, University of Chicago (2005).

[70] P. Zhou, E. Morikawa, Bulletin of the American Physical Society 53 (2008).

[71] C. Davisson, L.H. Germer, Physical review 30 (1927) 705.

[72] G. Mariotto, S. Murphy, I. Shvets, Physical Review B 66 (2002).

[73] M.V. Ganduglia-Pirovano, A. Hofmann, J. Sauer, Surface Science Reports 62 (2007) 219.

[74] I. Langmuir, Journal of the American Chemical Society 34 (1912) 860.

[75] S. Liu, S. Wang, W. Li, J. Guo, Q. Guo, The Journal of Physical Chemistry C 117 (2013) 14070.

[76] A. Baro, W. Erley, Surface Science Letters 112 (1981) L759.

[77] S.A. Chambers, Surface Science Spectra 5 (1998) 219.

[78] J.F. Anderson, Surface Science Spectra 4 (1996) 266.

[79] T. Sham, M. Lazarus, Chemical Physics Letters 68 (1979) 426.

[80] V. Coustet, J. Jupille, Il Nuovo Cimento D 19 (1997) 1657.

[81] B. Du Ahn, J.H. Lim, M.-H. Cho, J.-S. Park, K.-B. Chung, Journal of Physics D: Applied Physics 45 (2012) 415307.

[82] J.C. Fan, J.B. Goodenough, Journal of Applied Physics 48 (1977) 3524.

[83] M. Xue, S. Wang, K. Wu, J. Guo, Q. Guo, Langmuir 27 (2010) 11.

[84] V. Anisimov, I. Elfimov, N. Hamada, K. Terakura, Physical Review B 54 (1996) 4387.

[85] F. Bozso, G. Ertl, M. Grunze, M. Weiss, Applications of Surface Science 1 (1977) 103.

[86] J. Leveneur, G.I. Waterhouse, J. Kennedy, J.B. Metson, D.R. Mitchell, The Journal of Physical Chemistry C 115 (2011) 20978.

[87] S. Krasnikov, A. Vinogradov, K.-H. Hallmeier, R. Höhne, M. Ziese, P. Esquinazi, T. Chassé, R. Szargan, Materials Science and Engineering: B 109 (2004) 207.

[88] T. Regan, H. Ohldag, C. Stamm, F. Nolting, J. Lüning, J. Stöhr, R. White, Physical Review B 64 (2001).

[89] J.M. Pan, B. Maschhoff, U. Diebold, T. Madey, Journal of Vacuum Science & Technology A 10 (1992) 2470.

# APPENDIX: FOURIER TRANSFORM DECONVOLUTION APPLICATION

**Interface**

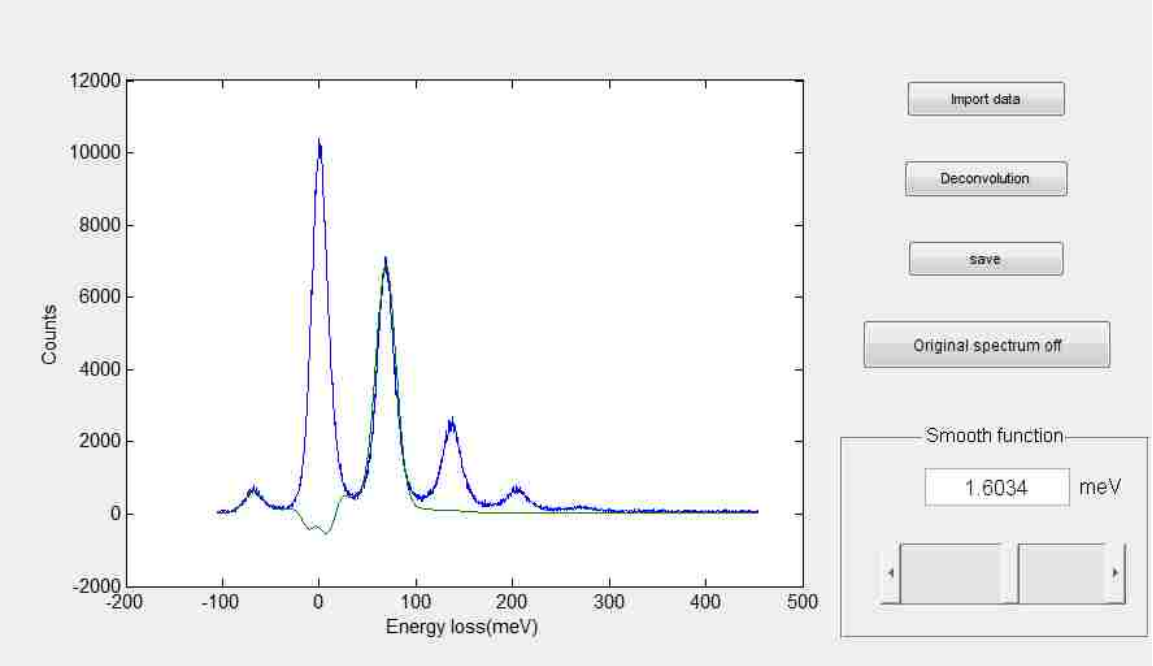


Figure i: Interface of FTD application. Blue spectra is HREELS on ZnO surface, green curve is spectra after FTD, the elastic peak and overtones are removed.

**Source code:**

```
function varargout = FTD(varargin)
gui_Singleton = 1;
gui_State = struct('gui_Name',       mfilename, ...
                   'gui_Singleton',  gui_Singleton, ...
                   'gui_OpeningFcn', @FTD_OpeningFcn, ...
                   'gui_OutputFcn',  @FTD_OutputFcn, ...
                   'gui_LayoutFcn',  [] , ...
                   'gui_Callback',   []);
if nargin && ischar(varargin{1})
    gui_State.gui_Callback = str2func(varargin{1});
end

if nargout
    [varargout{1:nargout}] = gui_mainfcn(gui_State, varargin{:});
else
    gui_mainfcn(gui_State, varargin{:});
end
% End initialization code - DO NOT EDIT


% --- Executes just before FTD is made visible.
```

```
function FTD_OpeningFcn(hObject, eventdata, handles, varargin)
% This function has no output args, see OutputFcn.
% hObject    handle to figure
% eventdata  reserved - to be defined in a future version of MATLAB
% handles    structure with handles and user data (see GUIDATA)
% varargin   command line arguments to FTD (see VARARGIN)

% Choose default command line output for FTD
handles.output = hObject;
handles.s=0;
handles.m1=0;
handles.m2=0;
handles.a1=0;
handles.b1=0;
handles.c1=0;
handles.cts=0;
handles.k=0;

% Update handles structure
guidata(hObject, handles);

% UIWAIT makes FTD wait for user response (see UIRESUME)
% uiwait(handles.figure1);


% --- Outputs from this function are returned to the command line.
function varargout = FTD_OutputFcn(hObject, eventdata, handles)
% varargout  cell array for returning output args (see VARARGOUT);
% hObject    handle to figure
% eventdata  reserved - to be defined in a future version of MATLAB
% handles    structure with handles and user data (see GUIDATA)

% Get default command line output from handles structure
varargout{1} = handles.output;


% --- Executes on button press in pushbutton1.
function pushbutton1_Callback(hObject, eventdata, handles)
% hObject    handle to pushbutton1 (see GCBO)
% eventdata  reserved - to be defined in a future version of MATLAB
% handles    structure with handles and user data (see GUIDATA)
 [filename, pathname] = uigetfile('*.txt;*.dat', 'Pick an data-file');
    if isequal(filename,0) || isequal(pathname,0)
       disp('User pressed cancel')
    else
       disp(['User selected', fullfile(pathname, filename)])

       data1=strcat(pathname,filename);
       [a handles.m1 handles.m2
d]=textread(data1,'%f %f %f %f','headerlines',7)

       %a=load(data1)
       %handles.m1=a(:,2)
       %handles.m2=a(:,3)
       plot(handles.m1,handles.m2,'linewidth',1)
```

```
        %options = fitoptions('gauss3');
        %options.Lower = [0 -Inf 0 0 -Inf 0 0 -Inf 0];
        %f=fittype('gauss3');
        %gfit=fit(handles.m1,handles.m2,f,options)

        %handles.a1=gfit.a1;
       % handles.b1=gfit.b1;
        %handles.c1=gfit.c1;

        xlabel('Energy loss(meV)')
        ylabel('Counts')

        guidata(hObject,handles);

    end

% --- Executes on selection change in popupmenu1.
function popupmenu1_Callback(hObject, eventdata, handles)
% hObject    handle to popupmenu1 (see GCBO)
% eventdata  reserved - to be defined in a future version of MATLAB
% handles    structure with handles and user data (see GUIDATA)

% Hints: contents = get(hObject,'String') returns popupmenu1 contents as cell
array
%        contents{get(hObject,'Value')} returns selected item from popupmenu1


% --- Executes during object creation, after setting all properties.
function popupmenu1_CreateFcn(hObject, eventdata, handles)
% hObject    handle to popupmenu1 (see GCBO)
% eventdata  reserved - to be defined in a future version of MATLAB
% handles    empty - handles not created until after all CreateFcns called

% Hint: popupmenu controls usually have a white background on Windows.
%       See ISPC and COMPUTER.
if ispc && isequal(get(hObject,'BackgroundColor'),
get(0,'defaultUicontrolBackgroundColor'))
    set(hObject,'BackgroundColor','white');
end


% --- Executes on button press in togglebutton1.
function togglebutton1_Callback(hObject, eventdata, handles)
% hObject    handle to togglebutton1 (see GCBO)
% eventdata  reserved - to be defined in a future version of MATLAB
% handles    structure with handles and user data (see GUIDATA)

% Hint: get(hObject,'Value') returns toggle state of togglebutton1



function edit1_Callback(hObject, eventdata, handles)
% hObject    handle to edit1 (see GCBO)
```

```
% eventdata  reserved - to be defined in a future version of MATLAB
% handles    structure with handles and user data (see GUIDATA)

% Hints: get(hObject,'String') returns contents of edit1 as text
%        str2double(get(hObject,'String')) returns contents of edit1 as a
double
s=str2double(get(hObject,'string'));
set(handles.slider2,'value',s)
handles.s=s;
guidata(hObject,handles);

% --- Executes during object creation, after setting all properties.
function edit1_CreateFcn(hObject, eventdata, handles)
% hObject    handle to edit1 (see GCBO)
% eventdata  reserved - to be defined in a future version of MATLAB
% handles    empty - handles not created until after all CreateFcns called

% Hint: edit controls usually have a white background on Windows.
%       See ISPC and COMPUTER.
if ispc && isequal(get(hObject,'BackgroundColor'),
get(0,'defaultUicontrolBackgroundColor'))
    set(hObject,'BackgroundColor','white');
end



% --- Executes on slider movement.
function slider2_Callback(hObject, eventdata, handles)
% hObject    handle to slider2 (see GCBO)
% eventdata  reserved - to be defined in a future version of MATLAB
% handles    structure with handles and user data (see GUIDATA)

% Hints: get(hObject,'Value') returns position of slider
%        get(hObject,'Min') and get(hObject,'Max') to determine range of
slider
s1=get(hObject,'value');
set(handles.edit1,'string',num2str(s1))
handles.s=s1;
handles=dec(handles)
guidata(hObject,handles)




% --- Executes during object creation, after setting all properties.
function slider2_CreateFcn(hObject, eventdata, handles)
% hObject    handle to slider2 (see GCBO)
% eventdata  reserved - to be defined in a future version of MATLAB
% handles    empty - handles not created until after all CreateFcns called

% Hint: slider controls usually have a light gray background.
if isequal(get(hObject,'BackgroundColor'),
get(0,'defaultUicontrolBackgroundColor'))
    set(hObject,'BackgroundColor',[.9 .9 .9]);
end
```

```
function handles=dec(handles)


 %options = fitoptions('gauss3');
       %options.Lower = [0 -Inf 0 0 -Inf 0 0 -Inf 0];
       %f=fittype('gauss3');
       %gfit=fit(handles.m1,handles.m2,f,options)
       datax=handles.m1
       datay=handles.m2
       f=@(b,datax)b(1)*exp(-((datax-b(2))./b(3)).^2);
       [b(1),index]=max(datay)
       b(2)=datax(index)
       n=1
half=max(datay)/2
while datay(n)<half
n=n+1
end
left=datax(n)
n=n+1
while datay(n)>half
n=n+1
end
   right=datax(n)
FWHM=right-left
b(3)=FWHM
b=[b(1) b(2) b(3)]
b=lsqcurvefit(f,b,datax,datay)
gfit.a1=b(1)
gfit.b1=b(2)
gfit.c1=b(3)

       handles.a1=gfit.a1;
       handles.b1=gfit.b1;
       handles.c1=gfit.c1;
mm=handles.a1.*exp(-((handles.m1-handles.b1)./handles.c1).^2);
mms=handles.a1.*exp(-((handles.m1-
handles.b1)./(handles.c1+(handles.s)^(0.5))).^2);
f1=fft(handles.m2);
f2=fft(mm);
f=f1./f2;
fln=log(f);
N=length(handles.m1);
ff=ifft(fln);
cts=cconv(ff,mms,N);
handles.cts=cts;
handles.output=[handles.m1 handles.cts];
disp(handles.output)

if(handles.k==1)
    plot(handles.m1,handles.cts);
else
```

```
    plot(handles.m1,handles.m2,handles.m1,cts)
end

xlabel('Energy loss(meV)')
ylabel('Counts')



% --- Executes on button press in pushbutton2.
function pushbutton2_Callback(hObject, eventdata, handles)
% hObject    handle to pushbutton2 (see GCBO)
% eventdata  reserved - to be defined in a future version of MATLAB
% handles    structure with handles and user data (see GUIDATA)

[filename,pathname] = uigetfile('*.txt','Save to(Please create a new txt
profile for saving)');
if isequal(filename,0) || isequal(pathname,0)
       disp('User pressed cancel')
    else
       disp(['User selected', fullfile(pathname, filename)])

fid = fopen(strcat(pathname,filename), 'wt');
fprintf(fid, '%6.2f %12.8f\n', handles.output');
fclose(fid)
end



% --- Executes on button press in pushbutton3.
function pushbutton3_Callback(hObject, eventdata, handles)
% hObject    handle to pushbutton3 (see GCBO)
% eventdata  reserved - to be defined in a future version of MATLAB
% handles    structure with handles and user data (see GUIDATA)
handles=dec(handles)
guidata(hObject,handles)

% --- Executes on button press in radiobutton1.
function radiobutton1_Callback(hObject, eventdata, handles)
% hObject    handle to radiobutton1 (see GCBO)
% eventdata  reserved - to be defined in a future version of MATLAB
% handles    structure with handles and user data (see GUIDATA)


% Hint: get(hObject,'Value') returns toggle state of radiobutton1


% --- Executes on button press in togglebutton2.
function togglebutton2_Callback(hObject, eventdata, handles)
% hObject    handle to togglebutton2 (see GCBO)
% eventdata  reserved - to be defined in a future version of MATLAB
% handles    structure with handles and user data (see GUIDATA)
handles.k=get(hObject,'value')
handles=dec(handles);
guidata(hObject,handles)
```

# VITA

Fangyang Liu was born in Jiangxi province of China, 1989. After moving to Zhejiang province, he graduates from Huzhou High School in June 2005. Then he enrolled in the Special Class for the Gifted Young (SCGY) of University of Science and Technology of China (USTC) in September the same year. He received his Bachelor degree of physics from USTC in June 2009. As his interest in experimental physics research, he entered the Department of Physics and Astronomy at Louisiana State University (LSU) in August 2009. He is a candidate to receive his PhD degree in May 2016.